Understanding and Modeling Tidewater Outlet Glacier Calving Dynamics - A Numerical Modeling Study

---

Dissertation

zur

Erlangung der naturwissenschaftlichen Doktorwürde

(Dr. sc. nat.)

vorgelegt der

Mathematisch-naturwissenschaftlichen Fakultät

der

Universität Zürich

von

Rémy Mercenier

aus

Belgien

Promotionskommission

Dr. Martin Lüthi (Leitung der Dissertation)

Prof. Dr. Andreas Vieli (Vorsitz)

Prof. Dr. Michael Schaepman

Dr. David Small

Zürich, 2019

Summary

The Greenland Ice Sheet is currently losing mass at a high, increasing rate and is one of the major contributors to sea level rise. Dynamic changes account for approximately 40 % of the recent mass loss from the Greenland Ice Sheet. The origin of these dynamic changes lies at the terminus of tidewater outlet glaciers where large scale retreat, thinning and acceleration of flow have been observed. Understanding the related iceberg calving process, by which ice is lost to the ocean, and its link to climate forcings, is therefore crucial to predict the future of the Greenland Ice Sheet and its contribution to sea level rise.

This thesis focuses on the application and development of numerical models based on the coupling of damage mechanics with ice flow to model iceberg calving and tidewater outlet glacier evolution. First, a numerical model of ice flow is used to analyze the stress and flow regimes in the vicinity of the calving front of idealized tidewater glaciers. The thesis then further presents the development of a transient coupled ice flow/damage evolution model that simulates the evolution of an idealized tidewater glacier. Finally, the developed calving model is used to investigate the effect of oceanic melt on iceberg calving and tidewater glacier evolution.

The relative water depth at the calving front and its geometry are shown to strongly influence the stress and flow regimes of an idealized tidewater glacier. The presence of water has a strong stablizing effect at the calving front. Based on the stress and flow regime analysis, a calving rate parametrization is proposed that only requires two geometrical properties: frontal ice thickness and relative water depth. The calving relation is calibrated using observations from Arctic tidewater outlet glaciers.

The developed transient calving model that couples ice flow and damage evolution produces emergent geometries and calving styles that are typically encountered in marine-terminating glaciers. The processes thus far shown to be relevant for the evolution of tidewater glaciers, e.g., iceberg calving and oceanic melt, are incorporated into the model. This allows for an investigation of the importance of individual processes, their time scales and their coupling. The choice of stress measure for damage evolution is found to be crucial to determine the calving front geometry. The von Mises stress measures produce the most realistic calving front evolutions for idealized tidewater glaciers. Consequently, the von Mises stress is used as stress measure for damage evolution in the sensitivity analysis of the model and forcing parameters.

While oceanic melt is generally assumed to lead to enhanced calving activity, detailed model experiments on the effect of submarine melt on tidewater glacier evolution show a more complex relationship than previously thought. The complex interplay between oceanic melt and iceberg calving strongly impacts the calving front geometry. The results of this modeling effort highlight the necessity to consider iceberg calving and oceanic melt as coupled processes that both alter the calving front geometry, which in turn affects the stress regime and consequently the calving process.

The main finding of this thesis is that the geometrical properties of the terminus control the dynamics of calving and hence the evolution of tidewater glaciers. It will therefore be necessary to further understand the physical processes that influence the calving front geometry in order to reproduce the recent and future dynamic changes of the Greenland Ice Sheet.

Acknowledgements

The successful completion of this PhD would not have been possible without great social and working environments.

While some people are not directly mentioned, my sincere thanks go to all the people that are not listed individually.

First of all, I want to thank the main supervisor of this thesis Martin Lüthi who provided an immense support and was always there when I needed help. This thesis would have been almost impossible without his great supervision and help. I would also like to thank Andreas Vieli for his supervision and providing the resources for the making of this thesis.

Further, I would like to thank all my colleagues from the 3G group of the department of Geography here in Zürich for their warm welcome, help, numerous barbecues, parties, fieldwork activities and sport events. In particular, I want to thank Simon for proofreading this thesis. Additionally, I want to thank Emiliano, Elias, Christoph, Daniel and Julian of the remote sensing group for the many kicker games that allowed me to release some tension during the making of this thesis.

Importantly, I need to mention the colleagues that shared my office and had to endure my presence for a long time: Gwendolyn, James and Alessandro. Thank you for all the discussions and especially the English improvements suggested by James.

Moreover, productive work would not be possible without the help of friends who help you clear your mind from the science. I therefore greatly appreciate their warm welcome and fun experienced in Zürich and in Belgium.

Finally, I need to thank my family and girlfriend Isabelle for their encouragement and support during the making of this thesis.

Structure and Contents

Structure

This dissertation contains three research publications reproduced in Chapters 2, 3 and 4. For each publication, a short summary, the main findings and the author contribution are first provided. Overall, the thesis is divided in 7 different chapters as follows:

Chapter 1 introduces the scientific background and the related research questions of this thesis.

Chapter 2 analyzes the modeled stress and flow regime of idealized glacier geometries, and the introduction of a new calving rate parametrization (Publication 1).

Chapter 3 presents the development of a transient iceberg calving model that couples ice flow and damage mechanics (Publication 2).

Chapter 4 investigates the effect of oceanic melt on tidewater glacier evolution based on the calving model developed in the previous Chapter (Publication 3).

Chapter 5 presents additional experiments performed for this thesis.

Chapter 6 presents the main findings in view of the research questions formulated in Chapter 1.

Chapter 7 provides concluding remarks and an outlook on potential future research applications.

Contents

Abbreviations

CMC	Continuous oceanic Melt Constant with depth
FE	Finite Element
GrIS	Greenland Ice Sheet
GRL	Geophysical Research Letters
IPCC	Intergovernmental Panel on Climate Change
JAMES	Journal of Advances in Modeling Earth Systems
LBB	Ladyzhenskaya–Babuška–Brezzi
LEFM	Linear Elastic Fracture Mechanics
PETSc	Portable Extensible Toolkit for Scientific Computation
PSD	Power Spectrum Density
SLR	Sea Level Rise
SMC	Seasonal oceanic Melt Constant with depth
SML	Seasonal oceanic Melt Linearly dependent on depth
SNES	Scalable Nonlinear Equations Solvers
SNSF	Swiss National Science Foundation
TC	The Cryosphere
UZH	University of Zurich

1 Introduction

This chapter introduces the importance of the iceberg calving process and provides an overview of previous work on this topic. The main research gaps addressed in this thesis are identified and clarified. Three research questions are finally formulated to approach the gaps identified in the literature.

This thesis was developed within the SNSF project: "*Understanding the long-term outlet glacier calving dynamics with a combined high-resolution field, -remote-sensing- and modeling approach*". The objective of this thesis is to understand calving glacier dynamics through a numerical modeling approach. The work performed contributes towards the wider topic of Greenland Ice Sheet dynamic mass loss estimation in the context of climatic change. This thesis has a strong numerical modeling aspect with a main focus on the identification of the key physical processes related to iceberg calving, through the implementation of damage based methods to simulate the evolution of tidewater glaciers.

1.1 Motivation and relevance

The Greenland Ice Sheet (GrIS) is currently losing mass at a high, increasing rate (van den Broeke et al., 2009, Shepherd et al., 2012), and is one of the major contributors to sea level rise (SLR) (IPCC, 2013). Accelerated ice discharge from the ice sheet to the ocean, besides increased surface melt at the margins of the ice sheet due to atmospheric warming, accounts for approximately 40 % of the current mass loss from the GrIS (van den Broeke et al., 2016). This dynamic mass loss is related to large-scale terminus retreat, thinning and acceleration of flow of tidewater outlet glaciers (Rignot et al., 2008), and is expected to further increase in the future (Nick et al., 2013).

Tidewater glaciers have a high potential for sudden rapid change through the calving retreat instability (Fig. 1.1) in the case of a deepening of the glacier bed in the upstream direction (Meier and Post, 1987, Vaughan and Arthern, 2007). The presence of over-deepened fjords, which are typical in Greenland, are likely to trigger such rapid changes. The potential for such dynamic changes of Greenland outlet glaciers raises concerns regarding their contribution to future SLR. Despite the recent observational efforts, there are currently majors limitations in understanding and predicting this dynamic behavior. For example, the spatial

resolution of the current large-scale ice sheet models is too large to spatially resolve most of the narrow and deep outlet glacier channels (Vieli and Nick, 2011).

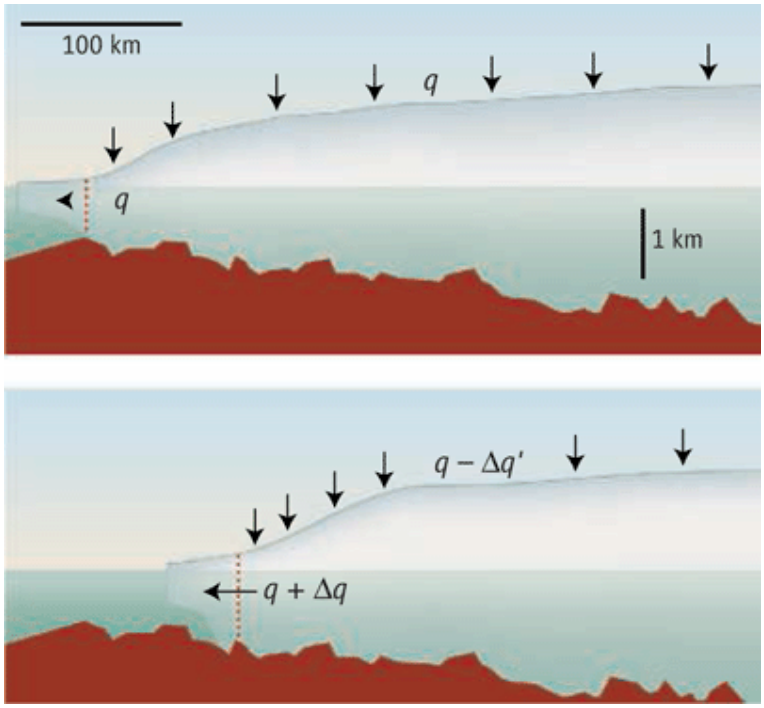

Figure 1.1: The calving retreat instability. In the above panel, the ice sheet is in equilibrium, the influx from snowfall q is in balance with the outflow. In the lower panel, the ice retreats with a glacier bed deepening in upstream direction. This triggers an imbalance between the influx and the outflow. If this imbalance promotes further retreat, the ice sheet margin becomes unstable. Figure extracted from Vaughan and Arthern (2007).

Since the origin of the dynamic changes lies at the terminus of tidewater outlet glaciers, understanding the iceberg calving mechanism, its link to external forcings (atmospheric, oceanic) and suggesting improvements to current models is essential to predict the future of the GrIS and its contribution to SLR (Straneo et al., 2013, Vieli and Nick, 2011). Currently, there is still a lack of dynamic representation of the processes occurring at the calving front, which enables us to reproduce the observed recent fast dynamic changes of the GrIS.

1.2 Calving models

Iceberg calving is the main process of dynamic mass loss from the GrIS at rates in the orders of km^3/yr for the major tidewater outlet glaciers. Calving occurs in different styles described in Figure 1.2. The rate of calving varies seasonally and intra-annually by orders of magnitude. This process plays a crucial role in both dynamic mass loss at the terminus of tidewater outlet glaciers and indirectly on the acceleration of inland ice flow, but its physical understanding remains limited (Straneo et al., 2011).

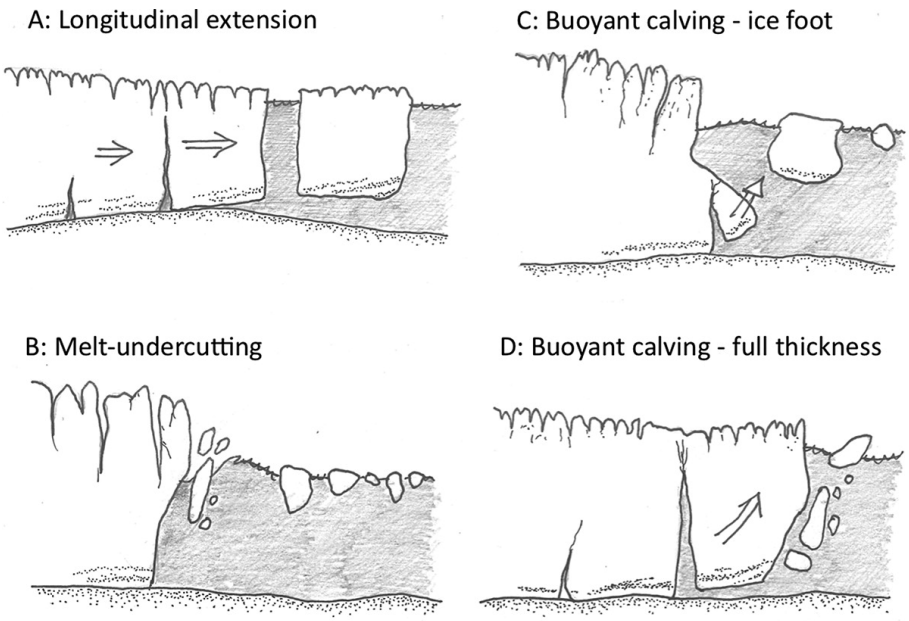

Figure 1.2: Calving styles. a: Rifts occurs due to longitudinal extension and an iceberg detaches from the glacier when basal, and surface crevasses penetrate the full thickness of the glacier. **b**: Melt-undercutting leads to the collapse of the overhanging ice. **c**: A subaqueous ice foot is released below the waterline, due to buoyancy forces. **d**: Due to rapid ice flow into deep water, a hydrostatic disequilibrium is created and a super-buoyant ice tongue rises up which subsequently detaches from the glacier. Figure extracted from Benn and Åström (2018)

Different approaches have been used to represent the calving process. Brown et al. (1982) proposed a simple empirical relationship to determine the calving rate (Fig. 1.3), i.e., the rate at which the terminus retreats through iceberg calving. In this approach, the calving rates are a function of the water depth, i.e., how deep the water is at the terminus of the glacier. This approach is based on observations of only a few tidewater glaciers in Alaska and is not process-based, therefore independent of glacier geometry and dynamics (Vieli et al., 2001).

The flotation or "height above buoyancy" calving criterion, proposed by Van der Veen (1996) and modified by Vieli et al. (2001), determines the position of the terminus by calving away all ice that is close to flotation. In this approach, the calving rate is an emergent quantity resulting from ice flow dynamics, with the bed topography as dominant control on the length variations of tidewater glaciers. A major limitation from these calving criteria is their inability to represent all types of calving front geometries, as they do not allow floating ice tongues to form (Vieli et al., 2001, Benn et al., 2007a).

Benn et al. (2007a,b) introduced a physics-based approach by setting the terminus position at the location where crevasses penetrate below the water level. The crevasse depth is computed using the Nye (1957) theory which relies on the equilibrium between longitudinal tensile strain rate and the creep closure resulting from the overburden pressure of the ice. This dynamic approach for calving allowed for successful reproduction of calving front variations of ocean-terminating glaciers in Greenland and Antarctica (Nick et al., 2010, Otero et al., 2010, Nick et al., 2013, Cook et al., 2014, Otero et al., 2017). Most of these calving mod-

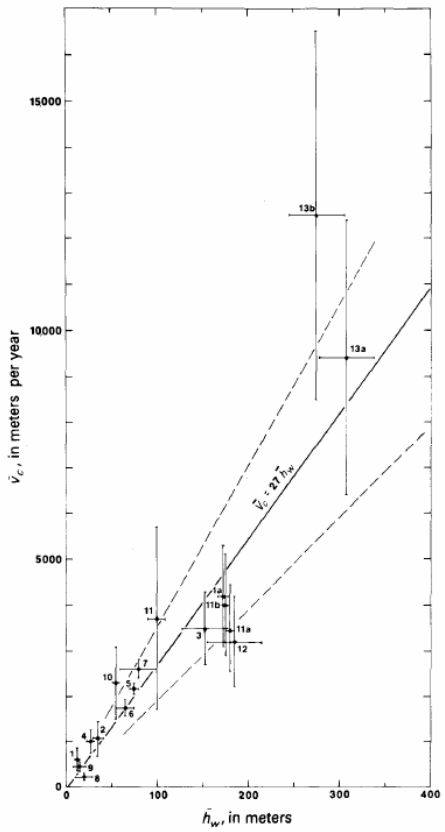

Figure 1.3: Empirical relationship based on the water depth to determine calving rates from Alaskan glaciers, from Brown et al. (1982)

els were however limited to either one-dimensional flowline or two-dimensional map-view representations of the glacier and adopted vertically-integrated stresses, neglecting the effect of bending forces related to melt-undercutting and buoyancy-driven calving, or the effect of lateral stress bridges (Benn et al., 2017, Todd et al., 2018). Further, although the crevasse depth model can be calibrated to observations (Lea et al., 2014), it lacks validation with field observations and is based on a snapshot of the stress balance, neglecting the pre-existence of cracks and their effect on the stress state of the glacier (Krug et al., 2014).

Individual calving events have been simulated using discrete element models, in which ice is represented as a group of blocks, that can slide, linked by springs, which can fail depending on the history of displacement and damage (Faillettaz et al., 2011). Discrete element models allow the simulation of the whole range of calving processes observed in nature (Faillettaz et al., 2011, 2015, Åström et al., 2013, Bassis and Jacobs, 2013, Benn et al., 2017). However, due to their high computational cost, discrete element models are only suited for simulating the evolution of glaciers on timescales of a few hours (Benn et al., 2017).

Recently, more sophisticated approaches overcame some of these limitations. Benn et al. (2017) combined a flow model with a discrete element model (Benn et al., 2017) to predict calving front positions, whereas Todd et al. (2018) developed a three dimensional transient

ice flow-calving model based on a modified crevasse-depth relation, in which calving occurs when basal and surface crevasses penetrate the entire thickness of the glacier. The latter was able to realistically simulate seasonal patterns of advance and retreat of Store Glacier when oceanic and ice mélange forcings were applied. Some major limitations remain in these recent efforts however. For example, in Todd et al. (2018), the calving front face after break-off in this model is assumed to be vertical and buoyant "toes" are automatically removed as soon as they form, which is not consistent with observations of subaqueous ice feet for a series of calving glaciers (Warren et al., 1995, Motyka, 1997, Hunter and Powell, 1998, O'Neel et al., 2007). Subaqueous ice foot release is one of the different calving styles observed in nature (Fig. 1.2).

Another recent approach relies on the application of the level set method in a two-dimensional map-view calving model for which the calving front retreats when the sum of the oceanic melt-undercutting $\dot{M}$ and calving c contributions is determined to be larger than the horizontal velocity vector $\boldsymbol{v}$. This is illustrated by the relation

$$\boldsymbol{v}_{front} = \boldsymbol{v} - \left(c + \dot{M}\right) \boldsymbol{n}, \tag{1.1}$$

where $\boldsymbol{v}_{front}$ is the calving front velocity and $\boldsymbol{n}$ is a unit normal vector that points outward from the ice domain (Morlighem et al., 2016). In this approach, calving occurs when the von Mises tensile stress (cf. Sect. 3.2.2 for definition) reaches a stress threshold. This method is computationally effective, as it uses the shelfy stream approximation to model ice flow (MacAyeal, 1989) and was first applied to model the response of Store Glacier to ocean thermal forcing (Morlighem et al., 2016), and then for the northwest coast of Greenland (Morlighem et al., 2019). Further, Choi et al. (2018) compared four calving laws in the vertically-averaged model to determine calving front positions for several Greenland outlet glaciers. They found that the von Mises tensile stress calving law is best suited to simulate observed ice front positions. This approach, however, remains limited to two dimensions and therefore neglects three dimensional effects.

Iceberg calving is a dynamic process of material failure. When the local stress field near the calving front exceeds the strength threshold of ice, the material begins to weaken and ultimately fails. This drives the formation and propagation of micro-cracks, which can coalesce and lead to the formation of crevasses at the surface and the bottom of the ice. Isotropic damage mechanics have thus been used to describe the micro-crack accumulation that eventually leads to iceberg calving. While other methods focus on individual crevasses in the ice, this method describes the presence of defects within the ice and their effect on the ice rheology (Duddu et al., 2013). Pralong et al. (2003) first proposed a Eulerian damage mechanics description combining Stokes flow and continuum damage mechanics, then were able to successfully predict the break-off of ice lamella from hanging glaciers (Pralong and Funk, 2005). Further glaciological studies used the combination of continuum damage mechanics with ice flow models (Pralong and Funk, 2005, Jouvet et al., 2011, Borstad et al., 2012, Duddu and Waisman, 2012, 2013, Duddu et al., 2013, Krug et al., 2014, 2015, Mobasher et al., 2016, Jiménez et al., 2017). Applying this technique in a Eulerian reference frame facilitates the

description of the physics of ice flow and fracture, however, the implementation of damage advection with flow is affected by artificial diffusion, and the numerical accuracy is mesh dependent (Jiménez et al., 2017). To overcome these issues, the use of a Lagrangian reference frame would be more appropriate to study fracture and damage mechanics (Duddu and Waisman, 2012, Jiménez et al., 2017). Currently however, no Lagrangian calving model based on damage evolution exists.

In this thesis, we focus on extending the use of numerical models based on damage mechanics to model iceberg calving. The first part of this thesis derives a calving rate parametrization based on an analysis of the modeled stress and flow regimes near the calving front. Using a damage evolution law and the stress distributions at the top surface of idealized glaciers, a calving rate parametrization is derived that is based solely on ice thickness and relative water depth. The second part of this thesis focuses on the development of a transient calving model that couples an ice flow model to a damage mechanics model, with a glacier geometry that evolves through time. A coupled Euler-Lagrange formulation is used to perform the evolution of the model geometry, which allows us to bypass the use of a rediscretization scheme and an advection scheme that could introduce numerical diffusion of damage.

1.3 Submarine melt

The process of submarine melt, i.e., the melt of ice at the calving front by oceanic water, is complex and difficult to observe. The available data, however, show high temporal variability, and that warmer subsurface waters, e.g., the West Greenland current, seem to reach into the Greenlandic fjords (Straneo et al., 2011). The mechanisms driving ocean water exchange between fjords and the open ocean are not well understood, but have been linked to large-scale atmospheric circulation (storms), suggesting that the oceanic and atmospheric forcings for calving are intrinsically coupled (Straneo and Heimbach, 2013). Oceanic melt at tidewater outlet glaciers is thought to be concentrated where localized plumes, driven by upwelling and mixing of fjord water with freshwater drainage from beneath the glaciers, are present (Jenkins, 2011, Fried et al., 2015, Rignot et al., 2015, Slater et al., 2018).

The recent rapid retreat of ocean-terminating glaciers of the GrIS has been attributed to atmospheric warming and the increased advection of warm ocean currents into the glacial fjords (Holland et al., 2008, Straneo and Heimbach, 2013, Luckman et al., 2015, Slater et al., 2018). Tidewater glacier retreat may be triggered by sufficiently rapid oceanic melt, leading to a dynamic response including flow acceleration, thinning and long-term instability (Morlighem et al., 2016, Slater et al., 2018).

Subaqueous melt erosion of the glacier terminus by warm water alters the calving front geometry and is generally assumed to result in the formation of an over-steepened calving front, due to undercutting below the waterline, and therefore increased stresses and calving activity (Vieli et al., 2001, Motyka et al., 2013, O'Leary and Christoffersen, 2013, Benn et al., 2017, Todd et al., 2018, How et al., 2019, Fig. 1.2). Conversely, in other studies, melt-

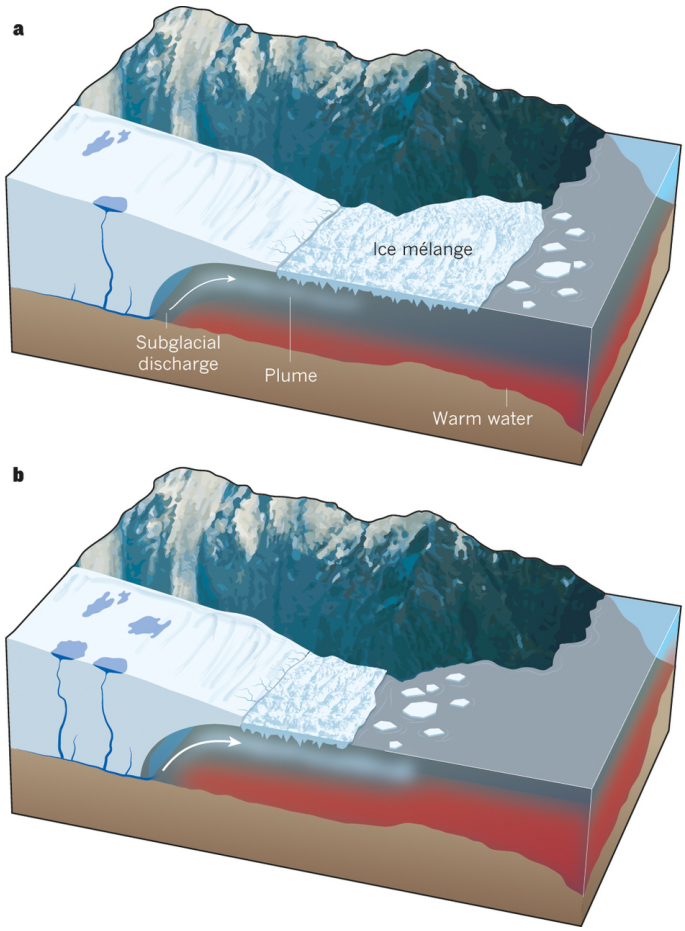

Figure 1.4: Submarine melt. **a**: Before the retreat, the oceanic water is relatively cold, subglacial discharge from the ice sheet is limited and ice mélange is extended. **b**: During the retreat, oceanic water is warmer, subglacial discharge increases and ice mélange is weakened. Figure extracted from Straneo et al. (2013).

undercutting has been shown to have a limited effect on calving rates (Cook et al., 2014, Todd and Christoffersen, 2014, Krug et al., 2015). Ma and Bassis (2019) recently investigated the controversial effect of submarine melting on the stress regime at the calving front and showed that the magnitude and vertical distribution of oceanic melt determines its enhancing or suppressing effect on calving. Their simulations were limited to the onset of one calving event, and did not explore the effect of oceanic melt on the evolution of the tidewater glacier geometry over a longer period of time.

Using the transient calving model developed in the second part of this thesis that couples ice flow and damage for tidewater glacier evolution with a freely evolving calving front geometry, the relationship between submarine melt and the iceberg calving mechanism, and consequently the long-term evolution of the idealized tidewater glaciers, was investigated in the last part of this thesis.

1.4 Research questions

Based on the review of current literature, three research questions were formulated. Each research question represents a research task that led to a publication. The rationale for each research question is first detailed followed by its formulation.

Studies have rarely focused on the effect of geometrical properties, e.g., calving front slope and/or water depth, of the calving front on its stress and flow regime. However, the stress and flow regime near the calving front determine the rate of iceberg calving. This interest in the relationship between geometrical properties and the stress state is motivated by the particular geometry of Eqip Sermia glacier in West Greenland.

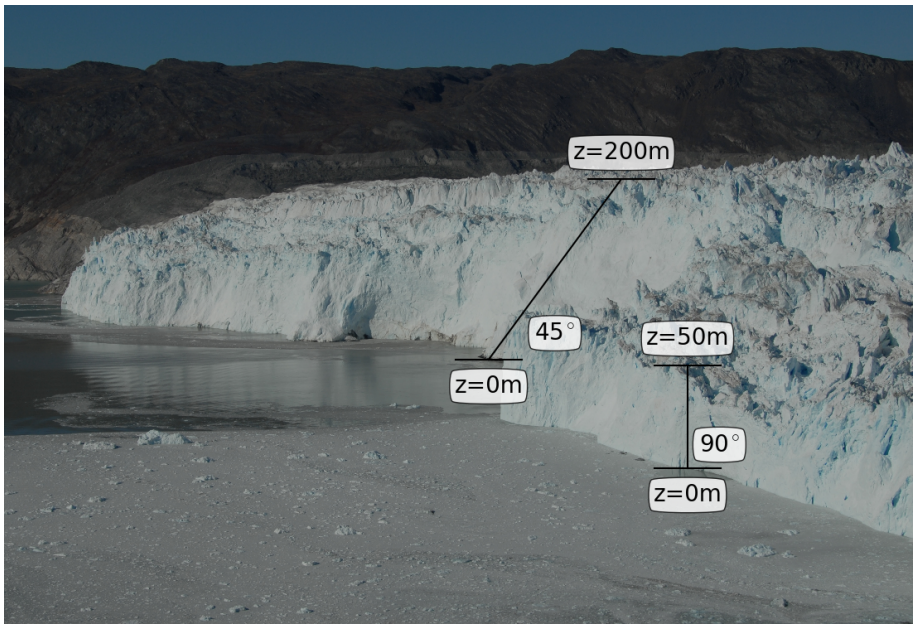

Figure 1.5: Calving front of Eqip Sermia glacier. Side view of the calving front of Eqip Sermia glacier in July 2016. The geometrical properties of the two distinct parts of the calving front are described in the boxes within the picture. Picture from Mercenier et al. (2018)

This medium-sized ocean-terminating glacier is characterized by two distinct calving front lobes with contrasting geometries: the grounded northern lobe exhibits a 200 m high inclined calving face with slope angles exceeding 45°, while the southern lobe features a vertical ice cliff of $\sim$ 50 m freeboard, with a water depth of $\sim$100 m (Lüthi et al., 2016). These substantially different geometries lead to distinct velocity and stress regimes in the proximity of the calving front, which also induce different types of calving. This leads us to the first research question:

1. *How do geometrical properties of the calving front influence the stress and flow regimes of tidewater glaciers?*

As previously mentioned, current models remain limited in their capacity to predict the behavior of tidewater glaciers. Based on an understanding of the stress regime that was gathered while working on the first research question, a new iceberg calving model is developed that couples an ice flow model to a damage mechanics model, which brings about the following research question:

2. *How realistically can a model that couples ice flow and damage mechanics reproduce calving front geometry and tidewater glacier evolution?*

Building on the model developed to answer the previous research question, the link between oceanic melt and the iceberg calving mechanism, which has a consequential impact on tidewater glacier evolution, is investigated in detail. The last research question thus reads:

3. *How does oceanic melt control the evolution of tidewater glaciers?*

These three research questions are addressed one by one in the following three Chapters, each of which represents a publication, and Chapter 6 presents an overall synthesis of the main findings.

2 Calving relation for tidewater glaciers based on detailed stress field analysis

Citation Mercenier, R., Lüthi, M. P., and Vieli, A.: Calving relation for tidewater glaciers based on detailed stress field analysis, The Cryosphere, 12, 721–739, doi: 10.5194/tc-12-721-2018, 2018.

Short summary Ocean-terminating glaciers in Arctic regions have undergone rapid dynamic changes in recent years, which have been related to a dramatic increase in calving rates. Iceberg calving is a dynamic process strongly influenced by the geometry at the terminus of tidewater glaciers.

Using a numerical model that solves the full equations for ice flow, the sensitivity to variations in front thickness and slope, the water depth and the strength of the coupling to the bed which results from sliding processes was investigated. These model experiments were performed on idealized geometries of grounded glacier termini and the results were explicitly expressed as a function of relative water depth.

Based on a detailed analysis of the model results, a novel parametrization of calving rate was derived and calibrated with observations from Arctic tidewater glaciers.

Main findings The Mercenier et al. (2018) study major findings are:

- Relative water depth and calving front slope control the stress and flow regime for an idealized grounded ocean-terminating glacier.
- Spatially uniform variations in basal sliding have a limited effect on the stability of the idealized grounded tidewater glacier.
- A simple new parametrization for calving rates is proposed for grounded tidewater glacier that is solely based on relative water depth and ice thickness and is calibrated with observations.

Contributions of the author The author set up and performed the model sensitivity analyses to water depth, calving front slope and basal sliding. The author implemented the new boundary conditions of the model, e.g., the water pressure at the ice/ocean boundary and

basal sliding. The analysis of the results, design of most figures and writing of the paper was performed by the author with support of all authors.

Data availability Data from this study can be made available from the authors upon request.

Journal *The Cryosphere (TC)*
Impact Factor: **4.524**

Abstract

Ocean terminating glaciers in Arctic regions have undergone rapid dynamic changes in recent years, which have been related to a dramatic increase in calving rates. Iceberg calving is a dynamic process strongly influenced by the geometry at the terminus of tidewater glaciers. We investigate the effect of varying water level, calving front slope and basal sliding on the state of stress and flow regime for an idealized grounded ocean-terminating glacier and scale these results with ice thickness and velocity. Results show that water depth and calving front slope strongly affect the stress state, while the effect of spatially-uniform variations in basal sliding is much smaller. An increased relative water level or a reclining calving front slope strongly decreases the stresses and velocities in the vicinity of the terminus and hence have stabilizing effects on the calving front. We find that surface stress magnitude and distribution for simple geometries are determined solely by the water depth relative to ice thickness. Based on this scaled relationship for the stress peak at the surface, and assuming a critical stress for damage initiation, we propose a simple and new parametrization for calving rates for grounded tidewater glaciers that is calibrated with observations.

2.1 Introduction

Many ocean terminating glaciers in the Arctic are currently undergoing rapid retreat, thinning and strong acceleration in flow. These dynamic mass losses contribute to about half of the Greenland ice sheet's contribution to sea level rise (van den Broeke et al., 2009), and are expected to further increase in the future (Nick et al., 2013). The mechanism of iceberg calving is thereby at the heart of these rapid dynamic changes of ocean terminating glaciers. However, the understanding of the involved processes as well as the capability of predictive flow models to represent calving are limited (Vieli and Nick, 2011, Straneo et al., 2013).

Tidewater glacier evolution is the result of an interplay between mass flux from upstream and the rate and size of calving events (Post et al., 2011). Both processes are strongly influenced by the geometry of the glacier surface, the glacier bed and the bathymetry of the proglacial fjord (Nick et al., 2009) as well as external forcings such as submarine melt due to heat advection by ocean currents (Motyka et al., 2013, Straneo and Heimbach, 2013, Straneo et al., 2013, Howat et al., 2010, Carr et al., 2013b) or changes in ice-mélange (Joughin et al., 2008, Amundson et al., 2010).

Iceberg calving is a dynamic process of material failure that occurs when the local stress field in the vicinity of the calving front exceeds the fracture strength of ice, driving the formation and propagation of cracks and eventually leading to the detachment of a block of ice from the glacier front. The local geometry and water level at the terminus together determine the stress field and thereby the fracture processes and the geometry evolution. Further, buoyancy forces of submerged ice and erosion from subaqueous melt are expected to enhance near-terminus stress intensity and hence calving rates, while a reclining terminus should reduce extensional stresses.

Several empirical and semi-empirical parametrizations of the calving rate have been proposed for different terminus geometries. A simple empirical relationship of linearly increasing calving rate with water depth, based on observations of tidewater glaciers in Alaska, has been established, used and extended for different regions (Brown et al., 1982, Benn et al., 2007b). This approach depends on the local water depth at the terminus only, is not process-based, and therefore independent of glacier geometry and dynamics (Vieli et al., 2001). In contrast, the flotation calving criterion, proposed by Van der Veen (1996) and modified by Vieli et al. (2001), determines the position of the terminus by calving away all ice that is close to flotation. In this approach the calving rate is an emergent quantity resulting from ice flow dynamics. Benn et al. (2007a,b) introduced a physics-based approach by setting the terminus position at the location where crevasses penetrate below the water level. The crevasse depth is computed using the Nye (1957) theory which relies on the equilibrium between longitudinal stretching and overburden stress of the ice. This dynamic approach for calving allowed for successful reproduction of calving front variations of ocean-terminating glaciers in Greenland and Antarctica (Nick et al., 2010, Otero et al., 2010, Nick et al., 2013, Cook et al., 2014, Otero et al., 2017). Although the crevasse depth model can be calibrated to observations (Lea et al., 2014), it lacks validation with field observations and is based on a snapshot of the stress balance, neglecting the pre-existence of cracks and their effect on the stress state of the glacier (Krug et al., 2014). A recent, more sophisticated approach by Benn et al. (2017) predicts calving positions based on the maximum principal stress distribution, and accounts for the effect of water pressure in the submerged parts of the glacier front by combination of a continuum flow model with a discrete element model to simulate calving events.

For near-vertical calving fronts, the main driver for calving is the horizontal deviatoric stress σ'_{xx} in the vicinity of the laterally-confined calving front. Its magnitude can be estimated from the difference of vertically integrated hydrostatic pressure within the ice and of ocean water at the calving front (Cuffey and Paterson, 2010, p. 353). The resulting extensional stress within the ice depends on the ice thickness H and the water depth H_w at the calving front

$$\sigma'_{xx} \simeq \frac{\rho_i g H}{4} \left(1 - \frac{\rho_w}{\rho_i}\omega^2\right) , \tag{2.1}$$

where ρ_i, ρ_w and $\omega = H_w/H$ are the ice density, water density and relative water depth (Tab. 2.1). This equation illustrates the square dependence of the horizontal extensional stress on relative water level at the terminus. However, it should be noted that this vertically integrated stress is not representative of the stress state near the surface of the terminus, and such a 'depth averaged' longitudinal stress may be inaccurate, as bending stresses are neglected.

Using the above longitudinal stress at the front, the maximum height for which a grounded glacier with a dry calving front can sustain a stable vertical front is approximately 110 m when crevasse depth is computed according to the Nye (1957) theory and 221 m when the ice is considered as undamaged and without crevasses (Bassis and Walker, 2012). However, the presence of water along the calving front influences this maximum stable height, as an increase of water depth for a constant ice thickness reduces the stresses and hence tends to

increase the stability of the glacier front. Thus, a thicker glacier must terminate in deeper water in order for its calving front not to exceed a certain stress limit and to remain stable (Bassis and Walker, 2012).

Calving termini can also be over-steepened by melt undercutting which leads to higher stress intensities (Hanson and Hooke, 2000) and may facilitate calving (Benn et al., 2017). Ice flow model results (Hanson and Hooke, 2000) suggest that an increase of water depth leads to a higher rate of oversteepening development at the calving front and thus an increase of calving activity. However, model results seem to indicate that melt undercutting does not significantly affect calving rates (Cook et al., 2014, Krug et al., 2015) while other studies suggest that calving rates are strongly related to melt undercutting for some arctic glaciers (Luckman et al., 2015, Petlicki et al., 2015, Cowton et al., 2016). Conversely, a calving front inclined towards the inland is expected to be more stable than a vertical cliff.

The state of stress near the calving front is determined by ice geometry and water depth, and controls the intensity and location of material degradation processes. Material creep and fracture processes in turn change the geometry of the glacier front. Observations and theoretical considerations indicate a tendency of increasing relative water level with increasing thickness (Bassis and Walker, 2012). This implies that thick glaciers approach flotation at their front, but for shallow water depth, the bounds on stress, and hence cliff geometry, are less well constrained.

The relationship between water depth, stress state, front geometry and related calving type is well illustrated for the example of Eqip Sermia, a medium size ocean terminating outlet glacier on the West Greenland coast. Figure 2.1 shows that this glacier is characterized by two distinct calving front lobes with contrasting geometries: The grounded northern lobe exhibits a 200 m high inclined calving face with slope angles exceeding 45° while the southern lobe features a vertical ice cliff of ~ 50 m freeboard with a water depth of ~ 100 m (Lüthi et al., 2016). These substantially different geometries lead to distinct velocity and stress regimes in the proximity of the calving front which also determine the type of calving. The high, grounded, inclined northern cliff collapses over timescales of weeks, releasing large ice masses of up to $10^6\,\mathrm{m}^3$ and generating 50 m tsunami waves (Lüthi and Vieli, 2016). In contrast, the southern part of the front calves smaller volumes of ice at intervals of several hours.

Motivated partly by the case of contrasting calving front geometries at Eqip Sermia, the aim of this study is to better understand the detailed flow and stress regimes in the vicinity of the calving front of tidewater glaciers, including those that are far from flotation. Using a numerical model that solves the full equations for ice flow, we investigate the sensitivity to variations in front thickness and slope, water depth, and the strength of the coupling to the bed which results from sliding processes. We perform these model experiments on idealized geometries of grounded glacier termini and succeed to explicitly express the results as function of relative water depth.

Based on these model results, we derive a novel parametrization of calving rate that is calibrated with observations from Arctic tidewater glaciers. This parametrization only requires

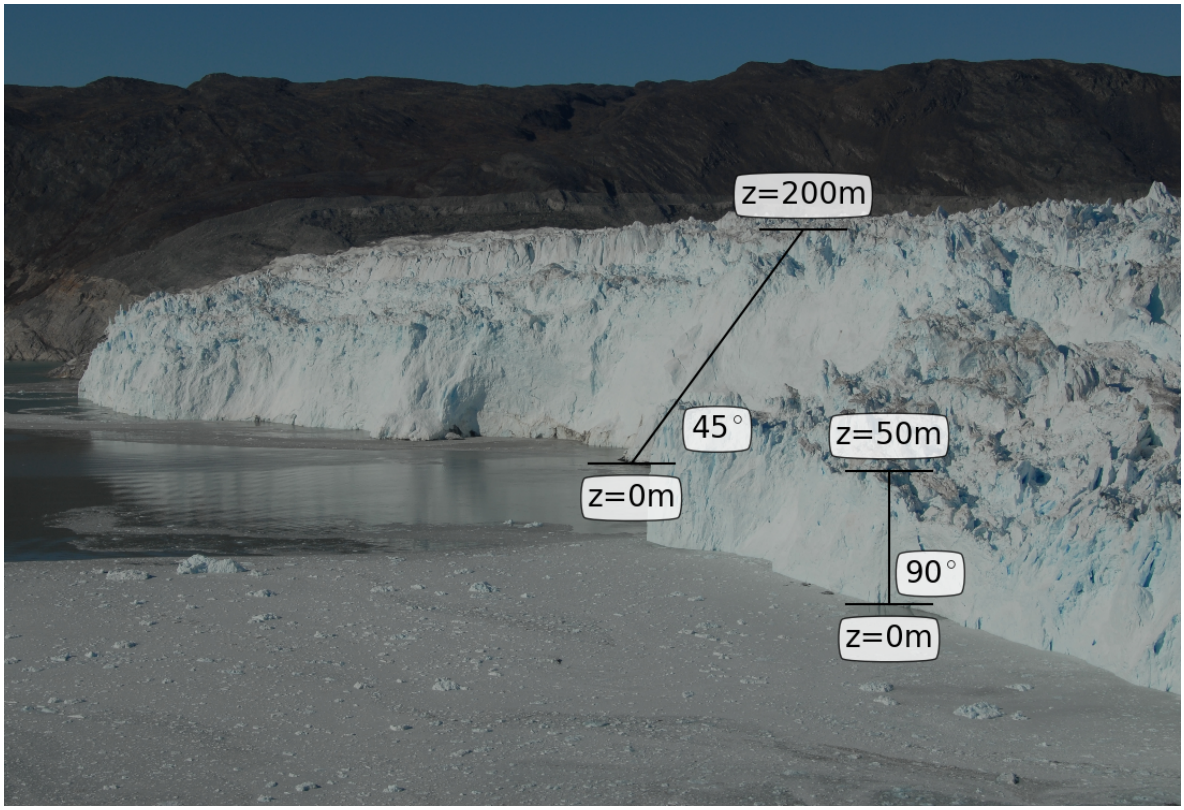

Figure 2.1: Calving front of Eqip Sermia glacier in July 2016. The boxes in the picture describe the geometrical properties of the two distinct parts of the calving front.

the relative water level and is based on a fit to the modeled stress field at the surface and an isotropic damage evolution relation.

2.2 Methods

2.2.1 Ice flow model and rheology

We used the finite-element library libMesh (Kirk et al., 2006) to implement the Stokes equations for continuum momentum and mass conservation

$$\mathrm{div}(\boldsymbol{\sigma}) + \rho_i \boldsymbol{g} = 0\,, \tag{2.2}$$

$$\mathrm{div}(\boldsymbol{u}) = 0\,, \tag{2.3}$$

where $\boldsymbol{\sigma}$ is the Cauchy stress tensor, ρ_i the ice density, $\boldsymbol{g}$ the gravitational force vector and $\boldsymbol{u}$ the velocity vector. As we assume ice to be incompressible and isotropic, the Cauchy stress tensor can be decomposed into an isotropic and a deviatoric part $\boldsymbol{\sigma'}$

$$\boldsymbol{\sigma} = \boldsymbol{\sigma'} + \sigma_m \boldsymbol{I}\,, \tag{2.4}$$

where $\sigma_m = \frac{1}{3}\mathrm{tr}(\boldsymbol{\sigma}) = \frac{1}{3}\sigma_{ii}$ is the isotropic mean stress and $\boldsymbol{I}$ the identity matrix. The ice rheology is described as a viscous power-law fluid (Glen's flow law), linking the deviatoric stress tensor $\boldsymbol{\sigma'}$ to the strain rate tensor $\dot{\boldsymbol{\varepsilon}}$

$$\boldsymbol{\sigma'} = 2\eta\dot{\boldsymbol{\varepsilon}}\,. \tag{2.5}$$

The effective shear viscosity η is defined as

$$\eta = \frac{1}{2}A^{-\frac{1}{n}}(\dot{\varepsilon_e} + \kappa_\varepsilon)^{\frac{1-n}{n}} \tag{2.6}$$

where $\dot{\varepsilon}_e = \left(\frac{1}{2}\dot{\varepsilon}_{ij}\dot{\varepsilon}_{ij}\right)^{\frac{1}{2}}$ is the effective strain rate, A the fluidity parameter, $n = 3$ the power-law exponent and κ_ε is a finite strain rate parameter included to avoid infinite viscosity at low stresses (Greve and Blatter, 2009, p. 56).

The model domain was discretized with second-order 9 node quadrangle elements with Galerkin weighting. Model variables are approximated with a second-order approximation for the velocities u and w and a first-order approximation for the mean stress σ_m. This forms a Ladyzhenskaya–Babuška–Brezzi (LBB) stable condition for the discretization of the Stokes flow. The accuracy of the solution was improved with adaptive mesh refinement near the calving front. The Stokes equations with the nonlinear rheology were solved with the Portable Extensible Toolkit for Scientific Computation (PETSc) nonlinear solver SNES (Scalable Nonlinear Equations Solvers) to a relative accuracy of 10^{-4} (Balay et al., 2017).

2.2.2 Model geometry and scaling

We used a 2-dimensional version of the model to conduct the geometrical tests, as illustrated in Fig. 2.2. The geometry is defined in a Cartesian coordinate system with horizontal axis x and vertical axis z with origin at sea level at the calving front (where $x = 0$). The ice moves from right to left. The idealized glacier geometry used in all model experiments consists of a block of ice resting on a flat bed with a characteristic length $L = 2000\,\mathrm{m}$ and a characteristic ice thickness $H = 200\,\mathrm{m}$. The domain was discretized with 20 elements in the vertical and 200 elements in the horizontal which, after mesh refinement, led to a spatial resolution of $2.5\,\mathrm{m}$ in the terminus area.

All numerical results are scalable with reference values for ice thickness H_{ref} and overburden stress σ_{ref} and are therefore independent of the geometrical extent. This validity of the scaling was tested by running the model for different ice thicknesses which recovered identical flow and stress results. The velocity scale u_{ref} was chosen as the vertical surface velocity caused by uniaxial compression in pure shear of an ice block under its own weight

that is confined in the direction transverse to flow (Cuffey and Paterson, 2010, p. 377)

$$\begin{aligned} H_{\mathrm{ref}} &= H\,, \\ \sigma_{\mathrm{ref}} &= \rho_i g H \sim [0.009\,\mathrm{MPa\,m^{-1}}]\,H\,, \\ u_{\mathrm{ref}} &= \frac{AH\sigma_{\mathrm{ref}}^n}{8(n+1)} \sim [1.7\cdot 10^{-6}\,\mathrm{m^{-3}\,a^{-1}}]\,H^4\,. \end{aligned} \tag{2.7}$$

The coordinates and the water depth at the calving front H_w are scaled by the ice thickness H_{ref}

$$\widehat{x} = \frac{x}{H_{\mathrm{ref}}}, \qquad \widehat{z} = \frac{z}{H_{\mathrm{ref}}}, \qquad \omega = \frac{H_w}{H_{\mathrm{ref}}}\,. \tag{2.8}$$

All stress and velocity components are scaled according to

$$\widehat{\sigma} = \frac{\sigma}{\sigma_{\mathrm{ref}}}, \qquad \widehat{u} = \frac{u}{u_{\mathrm{ref}}}\,. \tag{2.9}$$

2.2.3 Boundary conditions

The upper surface of the glacier was described as a traction-free surface boundary. Basal motion was parametrized with a slipperiness coefficient C which relates the basal velocity u_b with basal shear stress τ_b (Gudmundsson and Raymond, 2008, Ryser et al., 2014a)

$$u_b = C\tau_b\,. \tag{2.10}$$

This boundary condition was implemented as a two-element layer with constant viscosity $\eta_s = h_s/C$ which was added at the bottom of the model domain representing the glacier. At the lower boundary of this "sediment layer", a Dirichlet boundary condition with zero velocity ($u = v = 0$) was imposed. A layer thickness of $h_s = 10\,\mathrm{m}$ was chosen, although tests with varying h_s showed no significant differences. This simple approach allowed to capture the physical processes that are relevant to this study. In the case of vanishing basal motion the two-element layer was left away, and Dirichlet boundary conditions ($u = v = 0$) were imposed directly at the bottom of the model domain representing the glacier.

At the calving front a normal stress boundary condition was imposed below the water level, while the surface above water was kept stress-free. The stress boundary condition thus reads

$$\begin{aligned} \sigma_{nn} &= \min(\rho_w g z, 0) \\ \sigma_{nt_i} &= 0 \qquad (i = 1, 2)\,, \end{aligned} \tag{2.11}$$

where σ_{nn} and σ_{nt_i} are the normal and tangential tractions applied on the calving front (σ_{nn} is negative, i.e., compressive since $z < 0$ below water) and ρ_w is the water density (Tab. 2.1).

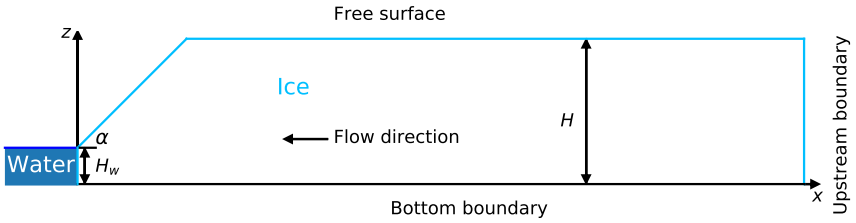

Figure 2.2: Geometry of the idealized grounded glacier. α is the slope angle of the calving front above the vertical cliff.

At the upstream boundary of the glacier domain velocities were fixed to zero. Additional modelling experiments showed that different values for this upstream boundary condition do not affect the results of the analysis.

2.2.4 Sensitivity analysis strategy

The stress state and flow field near the calving front is analyzed in three suites of numerical experiments that investigate the effect of variations in relative water level ω, the slope of the calving front, and basal motion.

The water level sensitivity experiments were performed for relative water levels $\omega = 0, 0.25, 0.5, 0.75, 0.85$ and $\omega_f = \frac{\rho_i}{\rho_w}$, where the last value is the relative water level at flotation. The calving front for this experiment was vertical, and the bottom boundary without sliding (i.e., zero velocity Dirichlet boundary condition). All these experiments were undertaken with both the density of ocean water (ρ_w =1028 kg m^{-3}) and freshwater (ρ_w =1000 kg m^{-3}).

The calving front slope sensitivity experiments were performed on a geometry with the upper part of the calving front reclining at various angles. The lower 25% of the calving front height was set vertical, and the upper part inclined at angles from 90°, 75°, 60° and 45°, until it reached the maximum surface height, see Fig. 2.2 for illustration. This particular geometrical setup was chosen to represent a simplified geometry of Eqip Sermia, which has a 50 m high vertical cliff at the bottom with a 45° inclined slope up to the top at 200 m. For this experiment, the relative water level was set to $\omega = 0$ and the sliding velocity was set to zero.

The bed slipperiness sensitivity experiments were performed on a block geometry with a vertical calving front and a relative water level $\omega = 0.5$. The basal slipperiness coefficient C was varied from 0 to 1000 m MPa^{-1} a^{-1} with 333 m MPa^{-1} a^{-1} increments. A slipperiness of 1000 m MPa^{-1} a^{-1} corresponds to a sliding speed of 300 m a^{-1} for a typical tidewater outlet glacier in Greenland with a driving stress of 0.3 MPa.

Table 2.1: Model parameters, notations, units and values for constant parameters.

Parameter	Notation	Value	Units
Fluidity parameter	A	75	$\mathrm{MPa}^{-3}\,\mathrm{a}^{-1}$
Effective damage rate	$\tilde{B}$	65	$\mathrm{MPa}^{-r}\,\mathrm{a}^{-1}$
Bed slipperiness	C		$\mathrm{m}\,\mathrm{MPa}^{-1}\,\mathrm{a}^{-1}$
Initial damage	D_0	0.2	
Critical damage	D_c	0.7	
Gravitational acceleration	$\boldsymbol{g}$	9.81	$\mathrm{m}\,\mathrm{s}^{-2}$
Sediment layer thickness	h_s	10	m
Ice thickness	H		m
Water level height	H_w		m
Glen exponent	n	3	
Damage law exponent	r	0.43	
Velocity vector	$\boldsymbol{u}$		$\mathrm{m}\,\mathrm{a}^{-1}$
Basal velocity	u_b		$\mathrm{m}\,\mathrm{a}^{-1}$
Calving rate	$\bar{u}_c$		$\mathrm{m}\,\mathrm{d}^{-1}$
Reference velocity	u_{ref}	$\sim [1.7 \cdot 10^{-6}\mathrm{m}^{-3}\,\mathrm{a}^{-1}]\, H^4$	$\mathrm{m}\,\mathrm{a}^{-1}$
Hayhurst parameter 1	α	0.21	
Hayhurst parameter 2	β	0.63	
Hayhurst stress	χ_H		MPa
Strain rate tensor	$\dot{\boldsymbol{\varepsilon}}$		a^{-1}
Effective strain rate	$\dot{\varepsilon_e}$		a^{-1}
Effective viscosity	η		MPa a
Sediment layer viscosity	η_s		MPa a
Finite strain rate parameter	κ_ε	$5.98 \cdot 10^{-6}$	a^{-1}
Ice density	ρ_i	917	$\mathrm{kg}\,\mathrm{m}^{-3}$
Sea water density	ρ_w	1028	$\mathrm{kg}\,\mathrm{m}^{-3}$
Fresh water density	ρ_w	1000	$\mathrm{kg}\,\mathrm{m}^{-3}$
Cauchy stress tensor	$\boldsymbol{\sigma}$		MPa
von Mises stress	σ_e		MPa
Maximum principal stress	σ_1		MPa
Mean stress	σ_m		MPa
Deviatoric stress tensor	$\boldsymbol{\sigma'}$		MPa
Reference stress	σ_{ref}	$\rho_i g H \sim [0.009\,\mathrm{MPa}\,\mathrm{m}^{-1}]\, H$	MPa
Damage threshold stress	σ_{th}	0.17	MPa
Basal shear stress	τ_b		MPa
Relative water level	ω		
Relative water level at flotation	ω_f	0.89	

2.2.5 Stress invariant combinations

Any criterion for fracture propagation or damage evolution should be independent of the choice of coordinate system, and can therefore be expressed as a function of the invariants and eigenvalues of the stress tensor. Hayhurst (1972) proposed a linear combination of three stress invariants to describe the creep rupture of ductile and brittle materials under multi-axial states of stress. The invariants chosen were maximum principal stress σ_1, first stress invariant $I_1 = \sigma_m = \frac{1}{3}\sigma_{ii}$, and the von Mises stress $J_2 = \sigma_e = \left(\frac{3}{2}\sigma'_{ij}\sigma'_{ij}\right)^{\frac{1}{2}}$ to form the stress combination

$$\chi_H = \alpha\sigma_1 + \beta\sigma_e + \gamma\sigma_m \,, \tag{2.12}$$

where the weights α, β and γ fulfill the conditions

$$0 \leq \alpha, \beta, \gamma \leq 1 \,, \tag{2.13a}$$

$$\alpha + \beta + \gamma = 1 \,. \tag{2.13b}$$

The Hayhurst stress χ_H has been used as a criterion for the initiation and evolution of damage in several glaciological studies (Pralong et al., 2003, Pralong and Funk, 2005, Duddu and Waisman, 2012, 2013, Duddu et al., 2013, Mobasher et al., 2016).

To investigate the full spectrum of possible stress states that lead to the initiation of damage, we investigated linear combinations of five stress invariants: $\sigma_1, \sigma_e, \sigma_m$, and additionally the third invariant of the stress tensor $I_3 = \det(\boldsymbol{\sigma})$ and third invariant of the deviatoric stress tensor $J_3 = \det(\boldsymbol{\sigma'})$. This extended linear combination reads

$$\chi = \alpha\sigma_1 + \beta\sigma_e + \gamma\sigma_m + \phi I_3 + \mu J_3 \tag{2.14}$$

with weights $\alpha, \beta, \gamma, \phi$ and μ that fulfill the conditions

$$0 \leq \alpha, \beta, \gamma, \phi, \mu \leq 1 \,, \tag{2.15a}$$

$$\alpha + \beta + \gamma + \phi + \mu = 1 \,. \tag{2.15b}$$

We performed a sensitivity analysis based on the five stress invariants of Eq. (2.14), calculated using the stress distributions, by systematically varying the weights with 0.1 increments (Eq. 2.15)

2.3 Results

2.3.1 Sensitivity analyses

All sensitivity experiment results shown in Figs. 2.3, 2.5 and 2.6 exhibit similar velocity and stress patterns. The effects of varying water level, basal slipperiness and calving front slope on the stress field are displayed as Hayhurst stress with parameters chosen according to

Pralong and Funk (2005) (Tab. 2.1). In general, the modeled velocities and stresses increase towards the calving front, with a local stress maximum at the surface that is located less than one ice thickness upstream of the calving front. This zone of high stress extends diagonally down towards the calving front where it has a second local maximum closely above the water level. For experiments with a relatively low water level, the absolute maxima in stress are found at the bottom of the calving face.

Water level height

The depth of the water at the calving front significantly impacts the stress regime and consequently the ice flow pattern and magnitude near the terminus. The effect of different water depths on the stress field is displayed as Hayhurst stress in Fig. 2.3a,c.

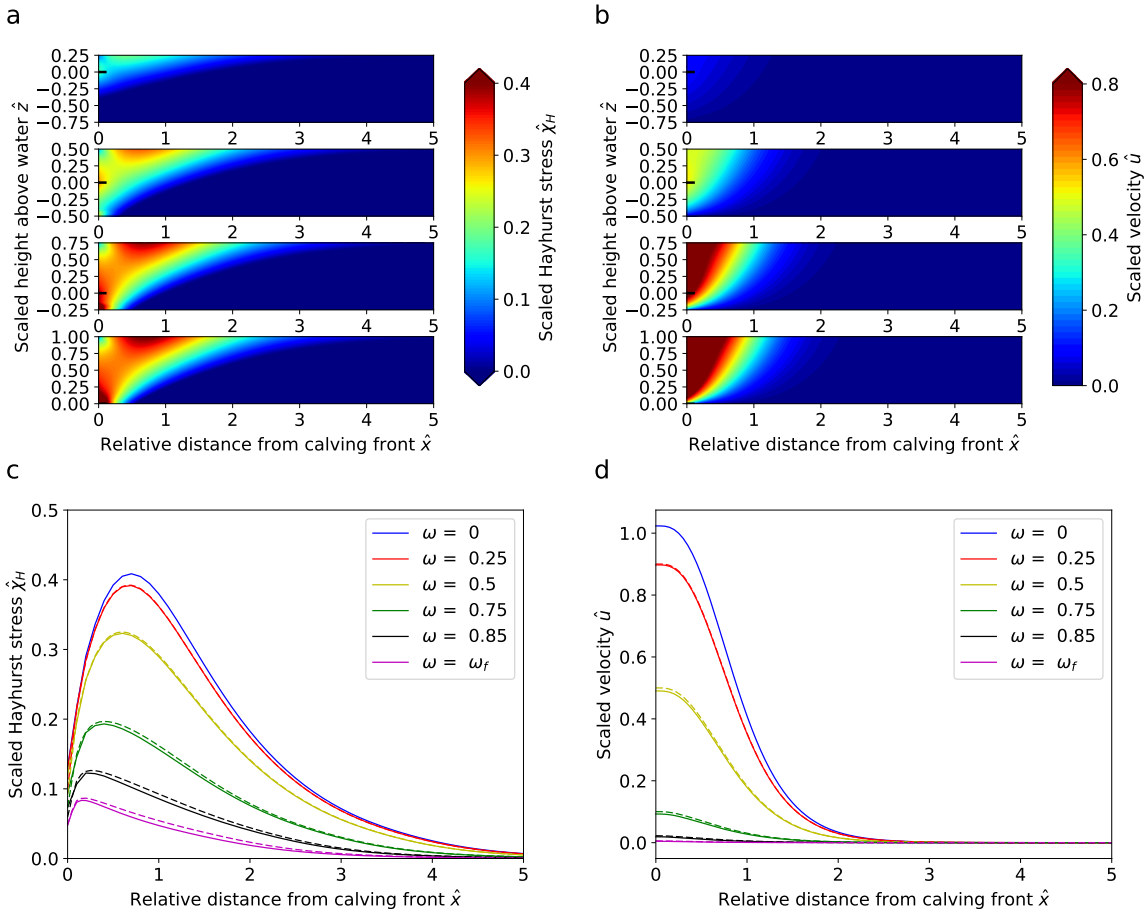

Figure 2.3: Sensitivity experiment results for varying water depth. (a) Scaled Hayhurst stress distribution. (b) Scaled horizontal velocity distributions. (c) Scaled Hayhurst stress along the surface. (d) Scaled horizontal velocity magnitude along the surface. In panels a and b, the subplots show increasing water depth from the bottom to the top (water level at $\widehat{z} = 0$). Solid and dashed lines in Panels c and d correspond to experiments with sea and fresh water densities, respectively.

For a reduction in the relative water level from $\omega = \omega_f$ to $\omega = 0$, the maximum Hayhurst stress at the surface increases from 0.08 to $0.42\,\sigma_{\mathrm{ref}}$ and the location of the stress peak at

the surface moves from 0.1 to 0.5 H upstream of the front, whereas the Hayhurst stress at the vertical calving front increases from 0.15 to $0.81\,\sigma_{\mathrm{ref}}$. Interestingly, the local maxima at the front are always located near the water level. Further, the position of the global stress maximum at low water levels (below 0.25) is found at the bottom of the calving front instead of the surface (Tab. 2.2).

Table 2.2: Maximum scaled Hayhurst stress and velocity for water depth experiments. The s and f letters indicate if the scaled Hayhurst stress maxima are found at the surface or at the bottom of the calving front, respectively.

ω	$\max(\widehat{\chi}_H)$	$\max(\widehat{u})$
0	0.808(f)	1.098
0.25	0.513(f)	0.967
0.50	0.323(s)	0.526
0.75	0.193(s)	0.097
0.85	0.123(s)	0.019
ω_f	0.083(s)	0.005

Figures 2.3b, 2.3d and 2.4 illustrate how velocities close to the calving front increase by more than one order of magnitude when the water level is decreased from near flotation ($\omega = 0.85$) to shallow water ($\omega = 0.25$). Note that for all water depths the velocities are only affected up to approximately 2.5 ice thicknesses upstream from the front.

Extrusion flow, a velocity pattern for which maximum horizontal velocity occurs below the surface (Waddington, 2010), is clearly visible in Fig. 2.4 in the vicinity of the calving front for the low water level cases. This pattern of extrusion flow near the terminus was also observed by Hanson and Hooke (2000) and Leysinger–Vieli and Gudmundsson (2004).

In summary, increasing relative water depth leads to decreased flow velocities and lower stresses and moves the peak of the Hayhurst stress at the surface closer to the front.

Calving front slope

Table 2.3: Maximum Hayhurst stress and velocity for calving front slope experiments.

Slope	$\max(\widehat{\chi}_H)$	$\max(\widehat{u})$
90	0.808	1.098
75	0.752	0.722
60	0.669	0.465
45	0.571	0.269

Results from the sensitivity experiment on calving front slope displayed in Fig. 2.5 show large variations in stresses and flow speeds. Maximum Hayhurst stresses are found at the bottom of the calving front for all cases ranging from 0.57 to $0.81\,\sigma_{\mathrm{ref}}$ for slope angles between

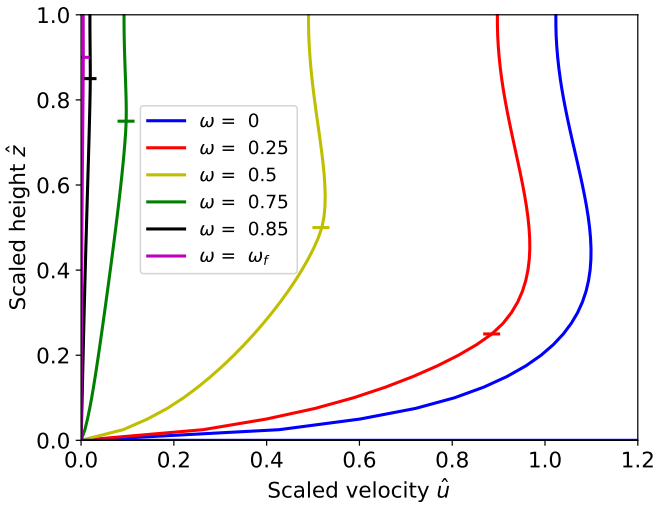

Figure 2.4: Scaled velocities along the vertical face of the calving front (solid lines) for different relative water levels. Horizontal line markers show the relative water level for each curve.

45° and 90° (Tab. 2.3). A second, local maximum occurs at the surface behind the end of the slope, but the magnitude strongly decreases with decreasing slope. The maximum velocity for a 45° slope is ~ 4 times smaller than for a vertical calving front (Fig. 2.5d). Thus, as the calving front gets steeper, the stresses as well as the velocities increase. Again, the peak in Hayhurst stress at the surface moves further upstream as the calving front becomes more gentle, and a further local stress maximum occurs along the sloped surface. Moreover, the velocities along the surface do not peak towards the front corner as in the vertical front case, but rather towards the bottom of the sloped surface, which is another sign of extrusion flow.

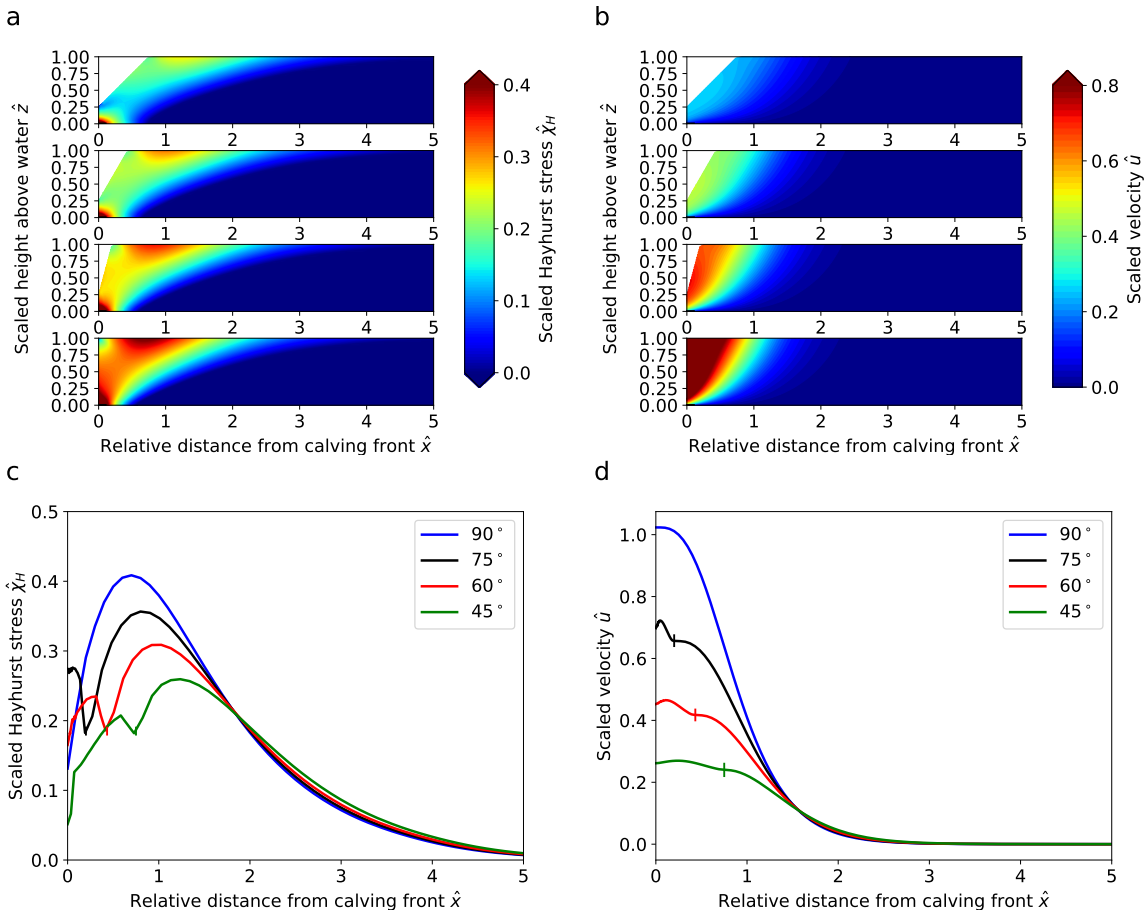

Figure 2.5: Sensitivity experiment results for varying calving front slope. Panels a, b, c and d are arranged the same as in Fig. 2.3. In panels a and b, the subplots show decreasing calving front slopes from the bottom to the top. In panel c, the local minimum of stress close to the calving front is located where the front reaches its maximal height. In panel d, vertical lines on the curves for inclined fronts mark the distance at which the maximal surface height is reached.

Bed slipperiness

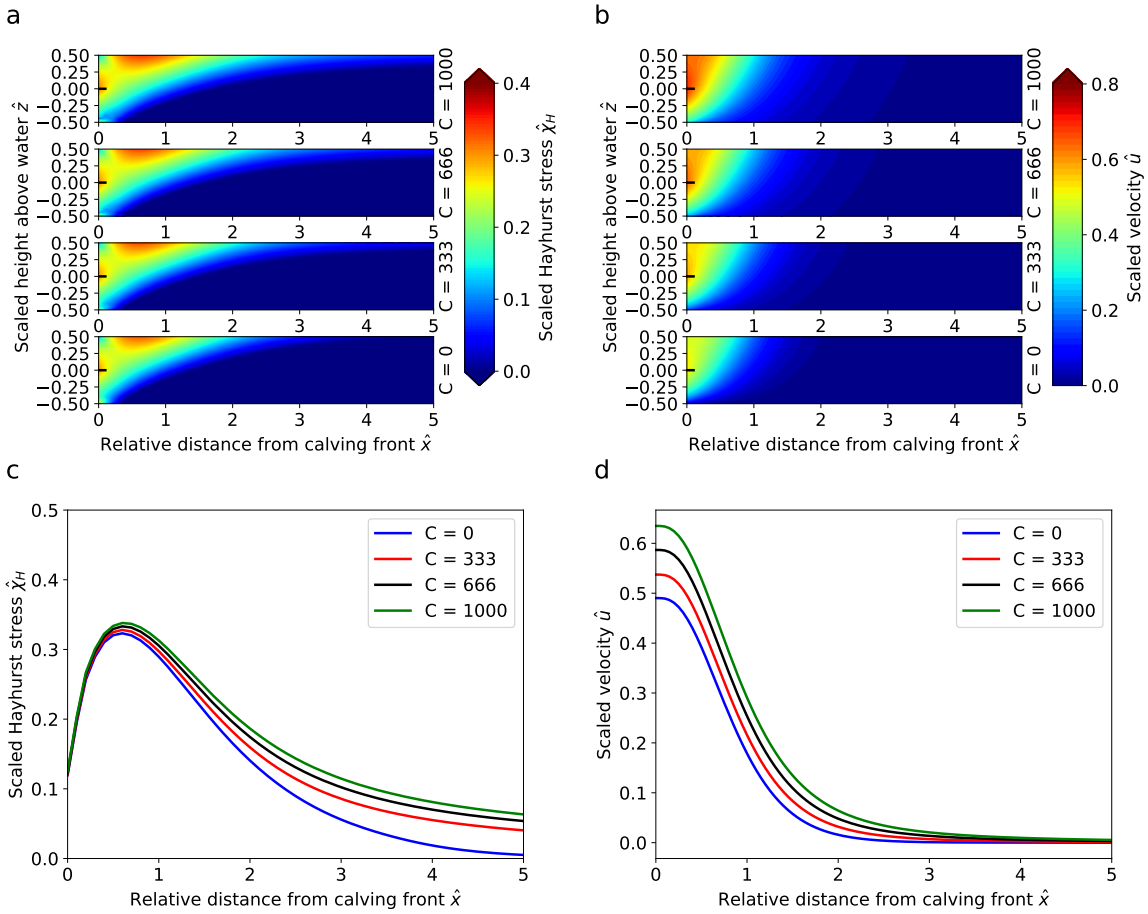

Figure 2.6: Sensitivity experiment results for varying bed slipperiness C. Panels a, b, c and d are arranged the same as in Fig. 2.3. In panels a and b, the subplots show increasing bed slipperiness from the bottom to the top. Units for bed slipperiness C are m MPa a^{-1}

The flow and stress regimes of the idealized glacier are less sensitive to an increase of bed slipperiness coefficient. Figure 2.6 shows that increased bed slipperiness leads to a slight increase in flow velocity, and the affected zone at the surface extends from 3 ice thicknesses in horizontal distance from the front to 5 ice thicknesses. Increasing the bed slipperiness coefficient produces very little effect near the front but causes a substantial increase of the stresses further upstream. The differences in the magnitudes of the Hayhurst stress maximum at the surface are, however, relatively small compared to the variations from other sensitivity experiments. The locations of the stress maxima remain the same for all bed slipperiness sensitivity experiments. Moreover, the spatial distributions of Hayhurst stress and velocity remain qualitatively very similar throughout the domain for the different bed slipperiness coefficients, and differences are mostly apparent at the surface.

Table 2.4: Maximum Hayhurst stress and velocity for bed slipperiness coefficient experiments.

C	$\max(\widehat{\chi}_H)$	$\max(\widehat{u})$
0	0.323	0.526
333	0.328	0.579
666	0.333	0.634
1000	0.337	0.688

Bed and surface slope

In the modeling presented so far we used a glacier geometry with horizontal surface and bed. Consequently the driving stress and hence velocities and stresses far upstream from the calving front are close to zero. In reality, glaciers have a sloping surface. Therefore, we repeated some of the above experiments on a simple glacier geometry with a sloped bed and surface, a fixed cliff height and no sliding. Bed and surface slopes were chosen as -5° and 5°, respectively.

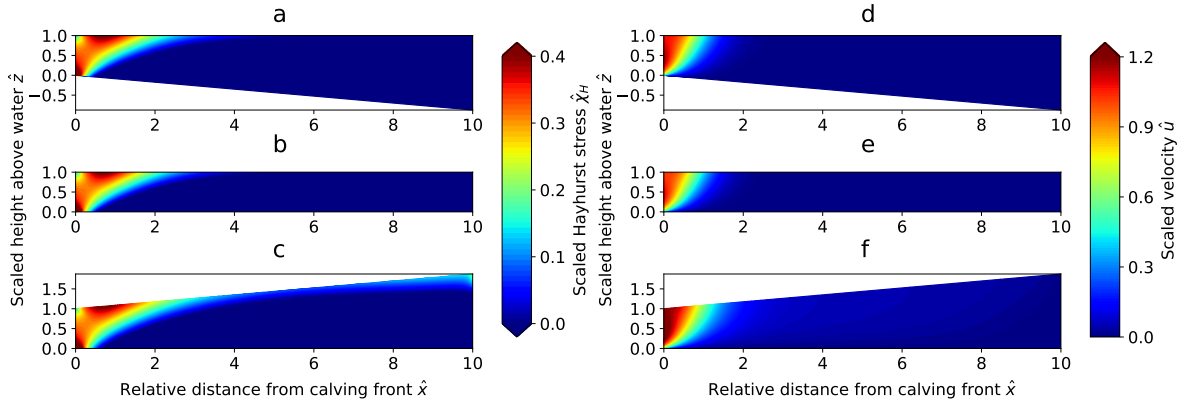

Figure 2.7: Sensitivity experiments result for an inclined surface (bottom), reverse bed (top) and the simple rectangular geometry (middle). The left and right panels show the scaled Hayhurst stress and velocity distributions, respectively.

Figure 2.7 illustrates the results: A reclining slope at the surface (i.e., surface height increasing towards the inland) with a flat bed leads to higher stresses and velocities upstream of the calving front as compared to the flat surface. However, the stress maximum and its location in the vicinity of the calving front remains almost identical (Fig. 2.7b,c). Similar results are obtained for a reverse bed slope with a flat surface (Fig. 2.7a,b).

To summarize, the stress and velocity fields in the vicinity of the calving front are only slightly altered for sloping bed and surface. It is, however, noteworthy that the reclining surface slope induces higher stresses near the surface, which could potentially induce crevassing, and thus advect pre-damaged ice to the calving front.

2.3.2 Stress invariant combinations

The Hayhurst stress, typically used as the driving force for damage evolution (Pralong et al., 2003, Pralong and Funk, 2005, Duddu and Waisman, 2012, 2013, Duddu et al., 2013, Mobasher et al., 2016), is not the only possible combination of objective stress measures. Here we attempt a systematic analysis of the possible stress invariant combinations (Eq. 2.14) and the corresponding locations of the stress maxima along the glacier surface.

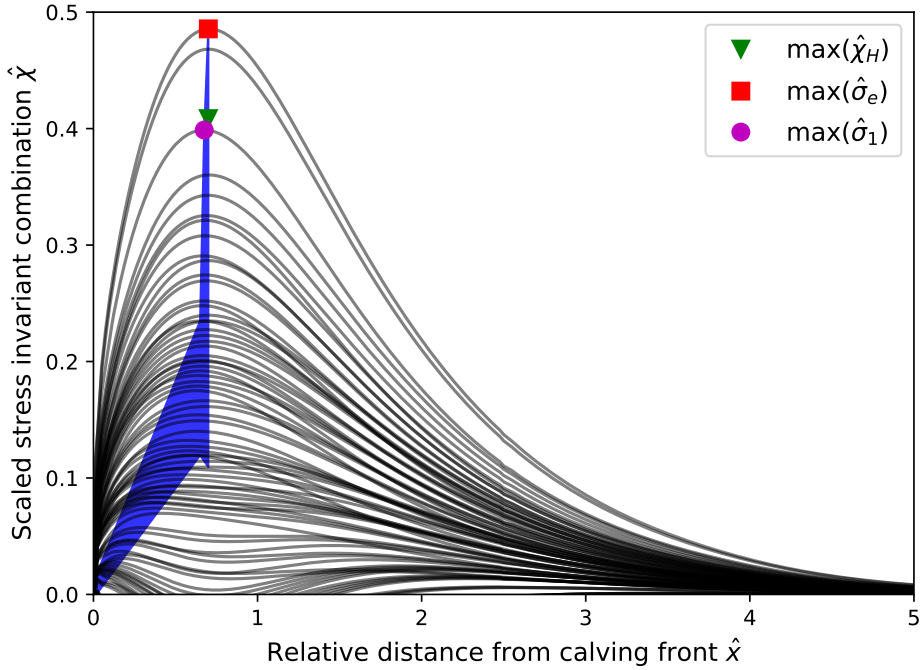

Figure 2.8: Combinations of five stress tensor invariants at the surface of an idealized glacier with a vertical calving front without water pressure and zero basal motion. Each black line represents a linear combination of five stress invariants. The blue envelope contains the maxima of all stress invariant combinations. The green triangle, red square and purple circle represent the maximum of the scaled Hayhurst stress $\widehat{\chi}_H$, von Mises stress $\widehat{\sigma}_e$, and maximum principal stress $\widehat{\sigma}_1$, respectively.

We illustrate this analysis at the example of the block geometry without any water pressure ($\omega = 0$) in Fig. 2.8 where all possible linear combinations of five stress invariants along the surface are displayed. While the stress combinations show a wide variety of curves, the maximum achievable stress states are dominated by the von Mises stress σ_e and the maximum principal stress σ_1, which both contribute to the Hayhurst stress. Hence, these two stress invariants are likely the driving factors for material failure in the vicinity of the calving front. An important aspect illustrated in Fig. 2.8 is the horizontal position of the stress maximum which is limited to $x_{max} \simeq 0.7\, H_{\mathrm{ref}}$. This analysis thus suggests that a zone with maximum crevasse opening cannot be located in greater distance from the calving front than x_{max} for an idealized glacier without pre-damaged ice.

The magnitudes and positions of the maximum stress invariant combinations for different relative water levels ω are shown in Fig. 2.9 (blue area corresponds to Fig. 2.8). The maximum stress for dry conditions ($\omega = 0$) is located $\sim 0.7\, H_{\mathrm{ref}}$ from the calving front with a maximum von Mises stress of $\sim 0.45\, \sigma_{\mathrm{ref}}$, whereas a water level close to flotation ($\omega = 0.85$) leads to a stress maximum of $\sim 0.15\, \sigma_{\mathrm{ref}}$ at $\sim 0.25 H_{\mathrm{ref}}$ from the calving front. Figure 2.9 clearly illustrates that water pressure at the calving front exerts a stabilizing effect on the calving front by both lowering the stresses and decreasing the distance from the calving front at which the stress maximum is located, as argued earlier by Bassis and Walker (2012).

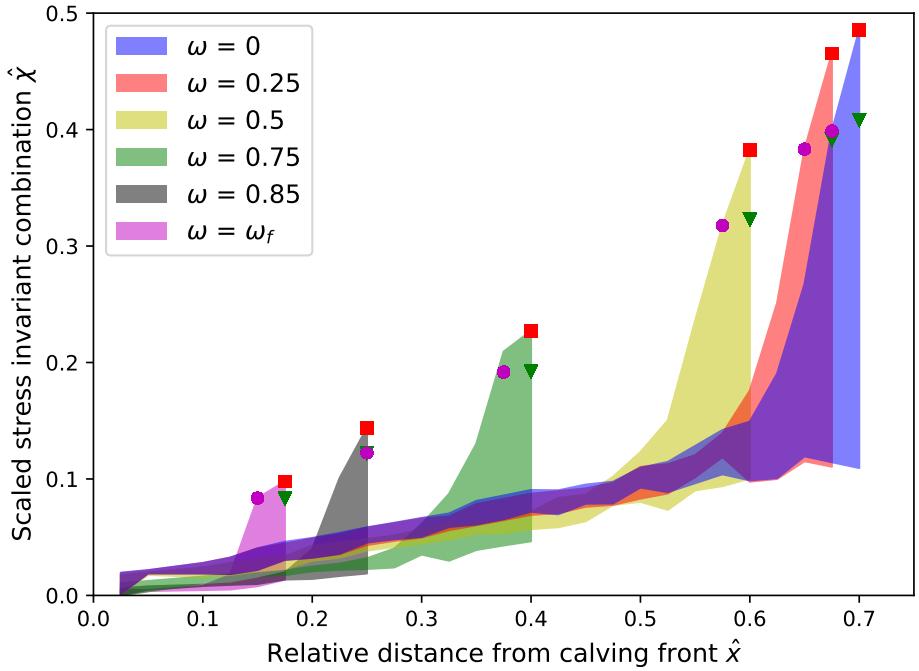

Figure 2.9: Envelopes of stress invariant combinations at the surface of the idealized glacier with zero basal motion for varying relative water level ω. The green triangle, red square and purple circle represent the maximum of the scaled Hayhurst stress, von Mises stress and maximum principal stress, respectively, for each water depth.

The Hayhurst, maximum principal and von Mises stress distributions are shown in Figs. 2.3a, 2.A.1a and 2.A.1b, respectively.

2.4 Stress parametrization and calving relation

The similarity of stress distribution curves along the glacier surface for varying relative water levels (Fig. 2.3c) allows for an explicit parametrization of the stresses. With some simple assumptions on a damage evolution law, a calving rate parametrization can be derived that is expressed as a function of total ice thickness and relative water level. Specifically, we as-

sume that surface crevasses open under the extensional stress σ_1. The Hayhurst stress would be a similarly suited stress measure for the extensional stress state under small compressive load at the glacier surface. The above stress state analysis showed that the three stress intensity measures σ_1, σ_e and χ_H along the glacier surface are very similar, as demonstrated in Fig. 2.9.

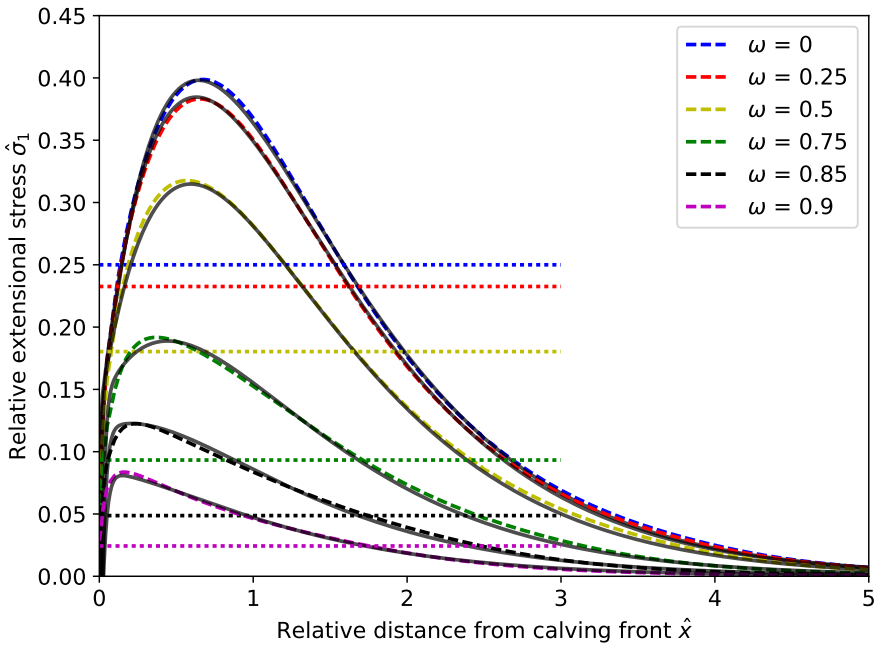

Figure 2.10: Modeled (dashed lines) and corresponding parametrized (solid lines) maximum extensive stresses $\widehat{\sigma}_1$ at the surface for different water depths. The dotted lines show the horizontal deviatoric stresses at the calving front for all water depths based on Eq. (2.1)

2.4.1 Stress parametrization

The distribution along the glacier surface of scaled maximum principal stress $\widehat{\sigma}_{1s}$ is shown for different relative water levels in Fig. 2.10 (this is approximately the tensile stress along the surface, whereas Fig. 2.3c shows Hayhurst stress). The similarity in shape of these stress curves allows for an approximate representation using a function that depends on the relative water level ω alone

$$\widehat{\sigma}_{1s}(\widehat{x}) = a(\omega)\,\widehat{\widehat{x}}\,\exp(-\widehat{\widehat{x}})\,, \tag{2.16}$$

where $\widehat{\widehat{x}}$ is a stretched and shifted version of the scaled (by ice thickness) horizontal coordinate $\widehat{x}$. This stretching function is somewhat cumbersome and is given in Appendix 2.A.1. The extensional stress reaches the maximum at $\widehat{\widehat{x}} = 1$ (setting the derivative of Eq. 2.16 to 0)

with magnitude $\widehat{\sigma}_{1,m} = a(\omega)\exp(-1)$, and can be approximated by

$$\begin{aligned}\widehat{\sigma}_{1,m}(\omega) &= 0.4 - 0.45\,(\omega - 0.065)^2 \\ &\simeq 0.4\left(1 - \frac{\rho_w}{\rho_i}\,(\omega - 0.065)^2\right)\,, \qquad (2.17a)\\ a(\omega) &= 1.087 - 1.223\,(\omega - 0.065)^2\,. \qquad (2.17b)\end{aligned}$$

It is interesting to note that the maximum extensional stress at the surface has a similar form as the mean deviatoric stress in Equation (2.1) but is $\sim 60\%$ higher. The scaled horizontal position of the stress maximum can be approximated by

$$\widehat{x}_m = 0.67\left(1 - \omega^{2.8}\right)\,. \qquad (2.18)$$

2.4.2 Analytical calving relation

Using the parametrizations of magnitude and position of the maximum extensional stress at the surface (Eqs. 2.17a and 2.18), the calving rate can be estimated under simple assumptions on crevasse formation.

One major assumption is that a large crevasse forms at the location of the maximum tensile surface stress where the ice is weakened until failure. Such crevassing seems realistic as both observations and model results show the formation of huge crevasses. When failure of the surface ice is complete, we assume that all ice in front of the crevasse is removed and a new calving front forms at the location of the crevasse. Here, we do not consider explicitly which processes are responsible for downward propagation of the crevasse. Several processes could be considered, such as bottom crevassing, hydro-fracturing by ponding water in surface crevasses, rapid elastic crevasse propagation (Krug et al., 2014), ice break-off in multiple steps (e.g., a surface slump, followed by subaqueous buoyant calving), or continued material fatigue due to tidal forcing. The proposed calving relation relies on the major assumption that processes responsible for ice break-off act on faster time scales than the formation of the surface crevasse, and therefore that the calving process is uniquely determined by the time to failure at the surface stress maximum. Thus, the average calving rate $\bar{u}_c$ can be calculated as the distance of the stress maximum divided by the time to failure T_f. In dimensional coordinates this is

$$\bar{u}_c = \frac{\widehat{x}_m H_{\mathrm{ref}}}{T_f}\,. \qquad (2.19)$$

Assuming further that crevasse formation can be described by isotropic damage formation with damage variable D, the stress in the damaged material is $\tilde{\sigma} = (1-D)^{-1}\sigma$ (Pralong et al., 2003, Pralong, 2006). The isotropic damage evolution relationship employed here is

$$\frac{dD}{dt} = B\frac{(\sigma_0 - \sigma_{th})^r}{(1-D)^{k+r}}\,, \qquad (2.20)$$

where B is the rate factor for damage evolution, r and k are constants, σ_0 is the stress in the work zone and σ_{th} a stress threshold for damage creation. Integrating this relation over time, the time-to-failure, i.e., the time required for damage to evolve from an initial value D_0 to a critical value D_c, reads

$$T_f = \frac{(1-D_0)^{k+r+1} - (1-D_c)^{k+r+1}}{(k+r+1)B(\sigma_0 - \sigma_{th})^r} \,. \tag{2.21}$$

We further assume that the stress in the work zone is the maximum tensile stress $\sigma_0 = \sigma_{1,m}$. Inserting the parametrizations for maximum tensile stress and stress maximum position (Eqs. 2.17b and 2.18) in the above relation yields

$$\bar{u}_c = \frac{\widehat{x}_m H}{T_f} = \left[\frac{0.67\,(k+1+r)\,B}{(1-D_0)^{k+r+1} - (1-D_c)^{k+r+1}}\right] \left(1-\omega^{2.8}\right) \left(\sigma_{1,m} - \sigma_{th}\right)^r H \,.$$

The term in square brackets is constant, and after renaming it the effective damage rate $\tilde{B}$, the expression reads

$$\bar{u}_c = \tilde{B} \left(1-\omega^{2.8}\right) \left(\left(0.4 - 0.45\,(\omega - 0.065)^2\right) \rho_i g H - \sigma_{th}\right)^r H \tag{2.22}$$

with parameter values $\tilde{B} = 65\,\mathrm{MPa}^{-r}\,\mathrm{a}^{-1}$ and $\sigma_{th} = 0.17\,\mathrm{MPa}$ which were determined from a calibration with data discussed below in Section 2.5.3. The parameter value $r = 0.43$ is chosen according to Pralong and Funk (2005).

2.5 Discussion

2.5.1 Sensitivity analyses

The stress intensity and therefore ice deformation rates are decreasing as the relative water level increases due to the pressure exerted by the water at the calving front. This feature is already captured by the depth integrated extensional stress at the front (Eq. 2.1), and in more detail in the parametrized maximum extensional stress (Eq. 2.17a), illustrated in Fig. 2.10. In both cases the square dependence of the horizontal stress on relative water level controls fracture or damaging processes, the magnitude and rate of which depend linearly on the stress intensity.

In addition, the detailed modeling shows that the stress peak at the glacier surface moves upstream when lowering the relative water level (Figs. 2.3 and 2.10), implying that crevasses are likely to open in greater distance from the calving front and leading to detachment of larger masses during calving.

A higher relative water level results in a more stable calving front (as emphasized by Bassis and Walker, 2012) which seems to be in contrast with the often-used relations which predict that calving rates increase with water depth (Brown et al., 1982, Meier and Post, 1987, Hanson and Hooke, 2000). In nature, however, glaciers terminating in deeper waters are

also thicker and calve at higher rates as they experience higher absolute (unscaled) stresses. Furthermore, submarine frontal melting is likely to lead to higher calving rates by oversteepening of the front (O'Leary and Christoffersen, 2013), although the melt undercutting effect on calving rates seems to be limited (Cook et al., 2014, Krug et al., 2015).

Using fresh water instead of sea water at the calving front yields slightly higher stresses and velocities (Fig. 2.3c,d). This difference can be explained by the reduced back pressure applied by fresh water on the calving front, which results from a lower water density.

The model results demonstrate that reclining calving fronts lead to lower velocities and stresses and thereby implicitly confirm that inclined calving fronts should reach larger stable heights than vertical cliffs, as observed for example at Eqip Sermia (200 m high at 45°). This sensitivity analysis on front slope may, together with observational data on non-vertical calving fronts, provide constraints on parameters of ice resistance to failure. Further, the presence of extrusion flow along the reclining calving face of an idealized glacier was demonstrated. Such a velocity pattern has been observed and measured on an inclined slope at the northern front of Eqip Sermia (Lüthi et al., 2016) but is rarely discussed in modeling studies (Hanson and Hooke, 2000, Leysinger–Vieli and Gudmundsson, 2004).

Basal sliding leads to increased stresses at the surface throughout the computational domain. Thus, basal sliding may cause an onset of ice damaging and crevasse opening at a greater distance from the calving front (Fig. 2.6c). The velocity patterns in Fig. 2.6b show that the influence of bed slipperiness is only apparent in the proximity of the calving front, even for high sliding coefficients. Moreover, stress distributions are almost identical for all bed slipperiness experiments, which implies that basal sliding has a negligible effect on the stability of the calving front. Basal sliding adds a constant velocity at the bottom of the domain rather than affecting the velocity gradients. This result does not include any spatial variation in bed slipperiness, which would likely be caused by including a water pressure dependent sliding relation. Effective pressure (the difference between ice normal stress at the bottom and water pressure) typically decreases towards the calving front for real glaciers with a sloping surface, and may cause additional sliding towards the front, an effect that was not considered in this modeling effort.

For a sloping glacier surface, the location and magnitude of the stress maximum in the vicinity of the calving front remain almost identical, as shown in Fig. 2.7. Similar results are obtained for a reverse bed slope with a flat surface, with a smaller influence on stresses and velocities than for the reclining surface. However, the effect on stresses and velocities upstream of the calving front is not visible for the reverse bed slope with a flat surface. This indicates that, for a glacier with a reclining surface slope, ice can potentially start damaging and forming crevasses at the surface far upstream from the calving front.

2.5.2 Calving relation

The proposed calving rate parametrization (Eq. 2.22) is simple and only requires two geometrical quantities: frontal ice thickness H and water depth H_w. The assumptions about

the failure process are lumped into three parameters $\tilde{B}$, σ_{th} and r, which can be determined by data calibration (Section 5.3). The parametrization exhibits many similarities with established calving relations but is formulated in terms of two quantities that are calculated by any ice flow model. It therefore is a drop-in replacement for other calving relations used in glacier models of different complexities.

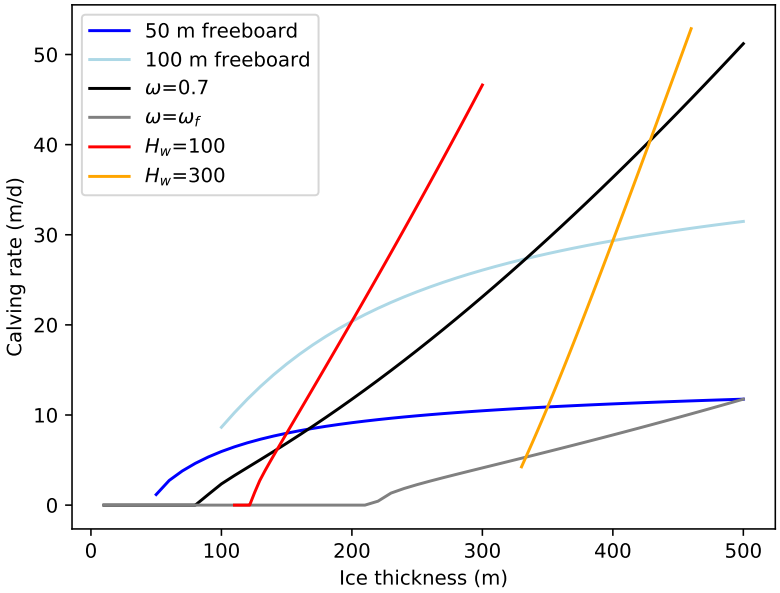

Figure 2.11: Calving rates predicted by the parametrization in relation to ice thickness. Calving rates increase with increasing total ice thickness for a given water depth $H_w = \omega H$ (red and orange lines), relative water level ω (black and gray lines) or freeboard $H - H_w$ (blue lines). Note that the gray line refers to a front at flotation.

The calving rate parametrization (Eq. 2.22) has some interesting properties which are illustrated in Figs. 2.11 and 2.12. Holding constant the relative water depth, the absolute water depth or the ice thickness results in different calving laws:

- For constant relative water level ω the calving rate grows roughly like $\bar{u}_c \propto H^{1+r}$ (black and gray lines in Fig. 2.11);
- For constant absolute water depth $H_w = \omega H$ a fit shows that roughly $\bar{u}_c \propto H^{1.25}$ (red and orange lines in Fig. 2.11);
- For constant ice thickness, the calving rate decreases with increasing relative water level (Fig. 2.12) roughly as

$$\bar{u}_c \propto \left(1 - \omega^{2.8}\right)\left(1 - 1.3\,\omega^2\right)^r \simeq \left(1 - \omega^{2.8}\right)\left(1 - \left(\frac{\rho_w}{\rho_i}\omega\right)^2\right)^r .$$

The predicted calving rate for a given water depth depends on the thickness of the glacier which is the result of the mass fluxes in the terminus area. Thus, calving rates depend on

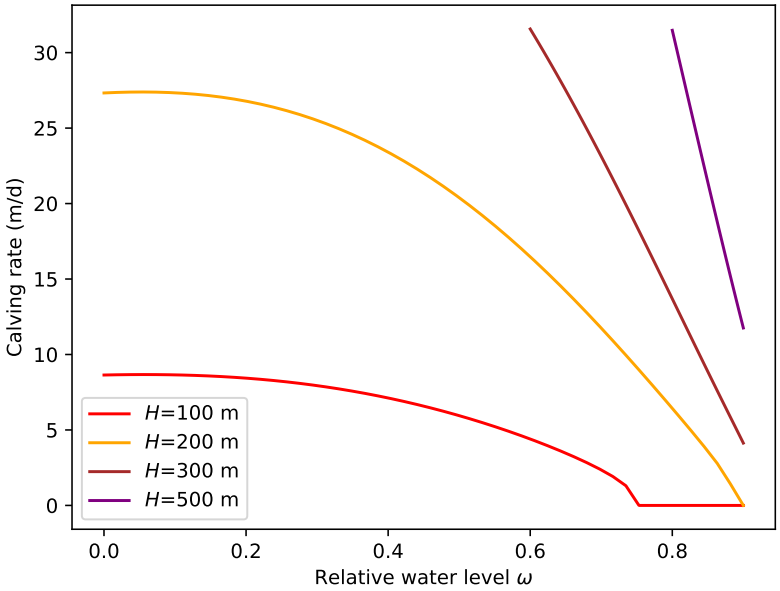

Figure 2.12: Calving rates predicted by the parametrization as a function of relative water level. Calving rate decreases under increase of the relative water level ω for constant total ice thickness H.

the surface evolution and hence the upstream dynamics of the glacier. The semi-empirical calving rate parametrization is therefore, in the sense of inclusion of upstream dynamics, similar to the position based calving models (Benn et al., 2007a, Nick et al., 2010, Todd and Christoffersen, 2014, Benn et al., 2017). The formulation as a calving rate also makes this parametrization relatively easy to use in larger-scale fixed grid models.

2.5.3 Calibration of the parametrization

The calving rate parametrization (Eq. 2.22) contains three empirical parameters $\sigma_{\mathrm{th}} = 0.17\,\mathrm{MPa}$, $\tilde{B} = 65\,\mathrm{MPa}^{-r}\mathrm{a}^{-1}$ that were obtained by calibration with data, and $r = 0.43$ which is taken from Pralong and Funk (2005). Calving rates thus obtained are not very sensitive to the exact choice of parameter values, which are within the range of previous studies (Duddu and Waisman, 2012, Lliboutry, 2002, Vaughan, 1993).

To calibrate these parameter choices, data on calving rate, ice thickness and water depth for a wide variety of tidewater glaciers in the Arctic were collected. The dataset covers the full range of water levels (relative and absolute), velocities and ice thicknesses that are found in Arctic tidewater glaciers. Unfortunately, many studies report only width-averaged data on calving front geometry and calving rate which are not suitable for our proposed relation which relies on local stresses on a flowline. Only a limited set of point data on calving front geometries are available from the published literature from which total ice cliff thickness, water depth and calving rate can be obtained. For the calibration, we used the values shown in Tab. 2.5 from diverse data sources.

Table 2.5: Values of calving front height, water depth and calving rate for different glaciers.

Abbr	Glacier	H_s (m)	H_w (m)	u_c ($\mathrm{m\,d^{-1}}$)	Source
Bow	Bowdoin 2015	25	220	1.5	Sugiyama et al. (2015), pers. comm. G. Jouvet
Col	Columbia 1983	53	213	6.7	Pfeffer (2007) Fig. 4
Col	Columbia 1988	29	243	10.6	Pfeffer (2007) Fig. 4
Col	Columbia 1994	61	280	15.4	Pfeffer (2007) Fig. 4
Col	Columbia 1998	103	253	29.7	Pfeffer (2007) Fig. 4
Col	Columbia 2000	122	260	24.8	Pfeffer (2007) Fig. 4
Eqi	Eqip Sermia 2015	50	80	8.2	Lüthi et al. (2016), Rignot et al. (2015)
Hel	Helheim 2015	80	615	25.0	Murray et al. (2015), Voytenko et al. (2015) Fig. 2
Hum	Humboldt N 2015	25	250	1.2	Carr et al. (2015)
Hum	Humboldt S 2015	30	125	0.2	Carr et al. (2015)
JI	Jakobshavn Isbræ 2008	100	800	35.6	Lüthi et al. (2009)
Kng	Kangilgata 1962/63	40	350	4.5	Carbonnell and Bauer (1968)
Lil	Lille 1962/63	25	230	1.5	Carbonnell and Bauer (1968)
Moe	Moench 2006	50	0	0.1	Pralong (2006)
RI	Rink Isbræ1962/63	70	560	13.0	Carbonnell and Bauer (1968)
Sto	Store 1962/63	65	500	17.3	Carbonnell and Bauer (1968)
Sto	Store 2015	60	500	16.0	Rignot et al. (2015), Ryan et al. (2015)
Yak	Yakutat 2015	30	325	0.4	Trüssel et al. (2015)

Contours of calving rates calculated with Eq. (2.22) are shown in Fig. 2.13 together with the maximum theoretical calving front height predicted by Bassis and Walker (2012). Figure 2.14 plots the same calving rate data against results from the parametrization. While a sizable spread of the data is visible, especially for low calving rates, the general agreement shows that the parametrization is well suited to estimate calving rates for this set of tidewater glaciers in the Arctic.

Note that the derivation of the parametrization is independent of the specific geometry or location of a tidewater glacier and thus the calibration is expected to be 'global' and valid for any tidewater glacier.

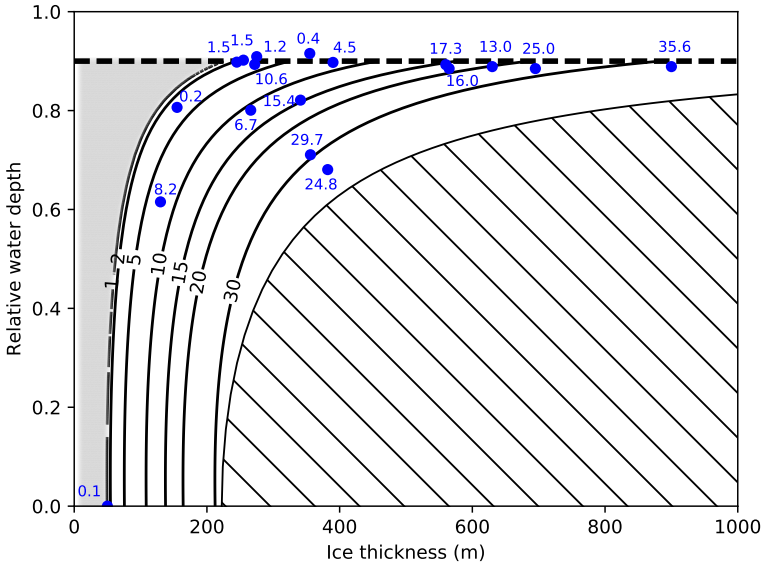

Figure 2.13: Calving rates ($\mathrm{m\,d^{-1}}$) predicted by the parametrization are shown as contours dependent on H and ω. The hatched region indicates the states excluded by the maximum calving front criterion (Bassis and Walker, 2012). The gray area indicates states where the stress threshold σ_{th} precludes calving. Blue dots with numbers indicate calving rates determined from measurements, shown in Table 2.5.

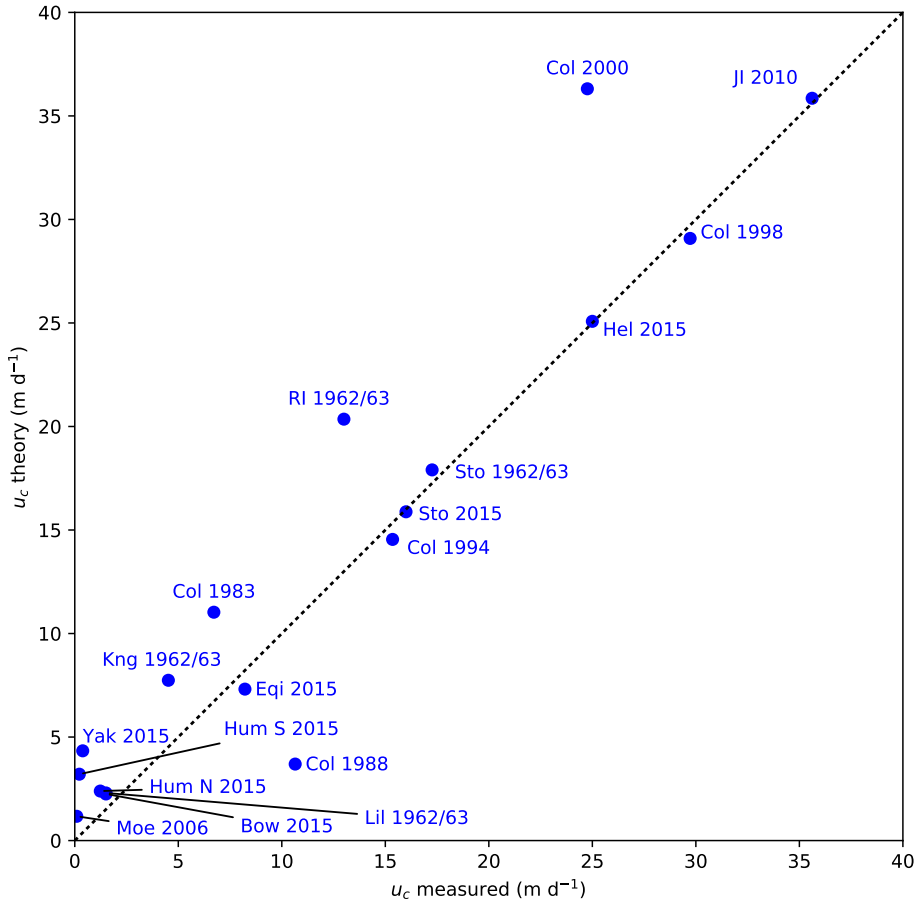

Figure 2.14: Comparison of measured calving rates with predictions from the calving parametrization. The glacier names are abbreviated according to Table 2.5.

2.6 Conclusions

This study improves our knowledge of the influence of geometry and water depth on the stress and flow regimes in the vicinity of the calving front, and proposes a novel calving rate parametrization.

The magnitude of the stresses and flow speeds near a grounded vertical calving front are mainly dependent on water depth, and increase with decreasing water depth. Thus, the presence of water at the calving front has a strong stabilizing effect. Importantly, the extensional stress at the surface can be parametrized as a function of relative water level only. Further, we find that grounded tidewater glaciers with reclining calving faces have the potential to reach larger maximum stable heights than those with vertical calving fronts. Spatially uniform variations in basal sliding likely have a weaker effect than water depth and calving front slope on the stability, as the magnitude and location of the stress maximum show a small sensitivity to variations in bed slipperiness.

A simple calving rate parametrization was derived that was calibrated with calving rate data of a set of tidewater glaciers in the Arctic. This approach can be used to compute calving rates for grounded tidewater glaciers with relatively simple geometries, if front thickness and water depth are known. The application of this parametrization in flow models of different complexity should be straightforward.

The present study lays the foundation for future, more detailed studies of the calving process on more realistic geometries. Detailed analyses including time evolution, further processes such as frontal melt and water-filled crevasses, and data validation will be necessary for the implementation of improved calving parametrizations.

Acknowledgements

The authors wish to thank Jaime Otero and Jeremy Bassis for their reviews and Douglas Benn, Joe Todd and Olivier Gagliardini for their comments that helped considerably to improve this manuscript. This work was funded by the Swiss National Science Foundation Grant 200021_156098.

2.A Appendix

2.A.1 Stress parametrization

The distribution of longitudinal tensile stress at the surface $\widehat{\sigma}_{1s}$ can be fitted using stretched and scaled coordinates $\widehat{\widehat{x}}$ depending on the relative water level ω

$$\widehat{\widehat{x}} = 1.37\,\widehat{x} + 0.09 + \frac{0.031}{(1.07 - w)^2} \tag{2.23}$$

The stress fit includes a taper towards the calving front which was chosen as an exponential. The full approximation to the stress curve is given by

$$\widehat{\sigma}_1(\widehat{x}) = a(w)\,\left(\widehat{\widehat{x}}\exp(-\widehat{\widehat{x}}) - \exp\left(\frac{-20\,\widehat{x}}{0.7 - \widehat{x}_m}\right)\right)\,. \tag{2.24}$$

The functions $a(w)$ and $\widehat{x}$ are given in Eqs. (2.17b) and (2.18).

2.A.2 Stress distributions for varying water depth

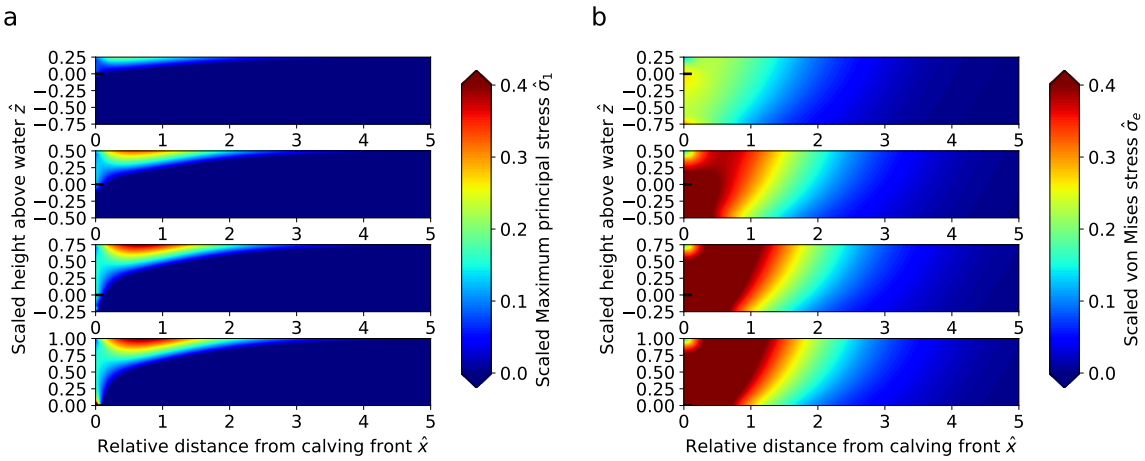

Figure 2.A.1: Stress distributions for varying water depths. (a) Scaled maximum principal stress distribution. (b) Scaled von Mises stress distribution. The subplots show increasing water depth from the bottom to the top (water level at $\widehat{z} = 0$).

3 A transient coupled ice flow-damage model to simulate iceberg calving from tidewater

Citation Mercenier, R., Lüthi, M. P., and Vieli, A.: A transient coupled ice flow-damage model to simulate iceberg calving from tidewater outlet glaciers, Journal of Advances in Modeling Earth Systems, in press, 2019a.

Short summary This study presents the development of a transient multi-physics finite-element model to simulate iceberg break-off and geometry evolution of a marine-terminating glacier. The model solves the coupled equations of ice flow, damage mechanics, oceanic melt and geometry evolution on the same Lagrangian computational grid. A modeling sensitivity analysis shows that the choice of stress measure used for damage evolution strongly influences the resulting calving front geometries. Our analysis suggests that the von Mises stress measures produce the most realistic calving front geometry evolutions for tidewater glaciers.

Main findings The Mercenier et al. (2019a) study's major findings are:

- A coupled transient ice flow model with damage and geometry evolution is developed to simulate ice break-off at the calving front.
- Calving front geometries in two dimensions are emergent results of the model.
- The choice of stress measure used for damage evolution strongly influences the evolution of the calving front geometry.
- For tidewater glaciers, the von Mises stress measures produce the most realistic geometries.

Contributions of the author The author continued the development of the pre-existing coupled ice flow/damage model. The author implemented the specific boundary conditions of the model, e.g., the buoyancy condition and submarine melting. The author wrote the

manuscript with the help of the co-authors, designed all graphics and was in charge of the paper publication.

Data availability Data from this study can be obtained from `https://doi.org/10.5281/zenodo.1492244`.

Journal *Journal of Advances in Modeling Earth Systems (JAMES)*
Impact Factor: **3.97**

Abstract

Iceberg calving, the detachment of an ice block at the glacier front, is the main process responsible for the dynamic mass loss from the ice sheets to the ocean. Understanding this process is essential to accurately predict ice sheet response to the future climate. We present a transient multi-physics finite-element model to simulate iceberg break-off and geometry evolution of a marine-terminating glacier. The model solves the coupled equations of ice flow, damage mechanics, oceanic melt and geometry evolution on the same Lagrangian computational grid. A modeling sensitivity analysis shows that the choice of stress measure used for damage evolution strongly influences the resulting calving front geometries. Our analysis suggests that the von Mises stress measures produce the most realistic calving front geometry evolutions for tidewater glaciers. Submarine frontal melt is shown to have a strong impact on the calving front geometry. The presented multi-physics model includes all processes thus far shown to be relevant for the evolution of tidewater glaciers, and can be readily adapted for 3D and arbitrary bedrock geometries.

3.1 Introduction

Iceberg calving, i.e. the mechanical loss of ice from glaciers and ice shelves, is one of the main contributors to sea level rise from tidewater glaciers together with surface melt (van den Broeke et al., 2016), and is expected to further increase in the future (Nick et al., 2013). Consequently, it is crucial to understand the calving process to accurately predict the ice sheets response to future climates (Benn et al., 2007b).

Iceberg calving is a dynamic process of material failure. When the local stress field near the calving front reaches the strength threshold of ice, the material begins to weaken and ultimately fails. This drives the formation and propagation of micro-cracks that can coalesce and lead to the formation of crevasses at the surface and the bottom of the ice. Intense crevassing eventually leads to the detachment of blocks of ice from the glacier front, termed iceberg calving. The break-off of chunks of ice can occur above and below the water line, and, if basal and surface crevasses intersect, blocks of the entire thickness of the glacier can detach.

The local geometry of the terminus controls the stress field and therefore the fracture and failure process (Hanson and Hooke, 2000, Mercenier et al., 2018). Further processes can contribute to iceberg calving. When calving losses above the water line exceed those below, hydrostatic forces lead to a buoyancy-induced upward rotation of the ice below water, which subsequently detaches from the calving front. On the other hand, subaqueous melt erosion of the glacier terminus results in the formation of overhanging ice above the water line and therefore increased stresses and calving activity (Motyka et al., 2013, O'Leary and Christoffersen, 2013, Benn et al., 2017).

The majority of modeling studies on iceberg calving have used the zero stress crevasse-depth model (Benn et al., 2007a,b) which sets the terminus position at the location where

crevasses penetrate below the water level. In this approach, the depth of a crevasse is determined based on the difference between the overburden ice pressure and the tensile stress. This dynamic approach for calving allowed for successful reproduction of calving front variations of ocean-terminating glaciers in Greenland and Antarctica (Nick et al., 2010, Otero et al., 2010, Nick et al., 2013, Cook et al., 2014, Otero et al., 2017, Todd et al., 2018). Although the crevasse-depth model can be calibrated to observations (Lea et al., 2014), the validation of the related processes with field observations is limited and is based on a snapshot of the stress balance, neglecting the pre-existence of cracks and their effect on the stress state of the glacier (Krug et al., 2014, Mercenier et al., 2018). The earlier studies applying this model were limited to one or two dimensions and did not permit the model domain to evolve through time.

The application of fracture mechanics for crevasse penetration was introduced to represent the rapid propagation of pre-existing fractures at very short time-scales (Smith, 1976). In Linear Elastic Fracture Mechanics (LEFM) models, crevasses penetrate downward as long as a stress intensity factor exceeds the fracture toughness of ice (Smith, 1976, Rist et al., 1999). The LEFM approach can be expanded for two-dimensional plan-view crevasse modeling and permits the combination of different modes of crevassing (Van der Veen, 1999, Colgan et al., 2016). Due to the boundary-condition dependence of the stress intensity factor, it is important to note that calving models using LEFM approaches (Van der Veen, 1998a,b, Krug et al., 2014), may be appropriate for floating ice tongues, but not for grounded glaciers (Jiménez and Duddu, 2018).

Recent more sophisticated approaches overcame some of the limitations of the zero stress and LEFM models. Benn et al. (2017) combined a flow model with a discrete element model to predict the calving front position, whereas Todd et al. (2018) developed a three dimensional ice flow- a stress threshold (Morlighem et al., 2016, cf. Sect. 3.2.2 for definition). This approach was used to model Store Gletscher's response to ocean thermal forcing. Further, Choi et al. (2018) compared four calving laws to determine calving front positions for several Greenland outlet glaciers. They found that the von Mises tensile stress calving law is best suited to simulate observed ice front positions.

As an alternative, a continuum description of micro-crack accumulation is provided by isotropic damage mechanics. While other methods focus on individual crevasses in the ice, this method describes the presence of defects within the ice and their effect on the ice rheology (Duddu et al., 2013). Pralong et al. (2003) first proposed a Eulerian damage mechanics description combining Stokes flow and continuum damage mechanics, and were able to successfully predict lamella break-off from hanging glaciers (Pralong and Funk, 2005). Further glaciological studies used the combination of continuum damage mechanics with ice flow models (Pralong and Funk, 2005, Jouvet et al., 2011, Borstad et al., 2012, Duddu and Waisman, 2012, 2013, Duddu et al., 2013, Krug et al., 2014, 2015, Mobasher et al., 2016, Jiménez et al., 2017, Mercenier et al., 2018). Applying this technique in a Eulerian reference frame facilitates the description of the physics of ice flow and fracture. However, the implementation of damage advection with flow is affected by artificial diffusion, and the numerical accuracy is mesh dependent (Jiménez et al., 2017). To overcome these issues, the use of a

Lagrangian reference frame would be more appropriate to study fracture and damage mechanics (Duddu and Waisman, 2012, Jiménez et al., 2017).

In this paper, we develop a transient multi-physics finite-element model that simulates ice break-off and oceanic melt at the calving front and tracks the evolving geometry. The proposed calving model is based on the coupling of continuum damage mechanics with ice flow equations, and with a computational domain that evolves through time. A coupled Euler-Lagrange formulation is used to perform the model evolution without the need for rediscretization. Elements for which the damage variable or the accumulated melt exceeds a threshold value are removed from the mesh, which allows us to effectively model ice break-off at the calving front. We provide a complete description of the model and its implementation. We then investigate the sensitivity of the model to the choice of stress measure and to variations in model parameters such as damage rate, critical damage, ice thickness, and oceanic melt rate. These model experiments are performed for an initially idealized glacier geometry that evolves with ice flow, oceanic melt, and calving.

3.2 Methods

We used the finite-element library libMesh (Kirk et al., 2006) to implement a transient coupled ice flow-damage model. The model is formulated as a moving-mesh algorithm outlined in the flow chart of Figure 3.1.

The computational domain (the glacier) is discretized with a finite-element mesh. The continuum Stokes flow equations with strain-rate dependent viscosity in a Eulerian reference frame are solved on this mesh at each time step. The resulting velocity field, defined on the mesh nodes, is used to calculate the evolution of a scalar damage variable, and for advection of the mesh nodes. An elimination algorithm deletes mesh elements that are considered destroyed and/or detached, representing glacier calving and oceanic melt.

In all presented model experiments, an idealized glacier geometry was used that initially consisted of a rectangular block of ice resting on a flat bed with an initial ice thickness $H = 200\,\mathrm{m}$ and length $L = 10\,H$. The model domain was defined in a Cartesian coordinate system with horizontal axis x and vertical axis z with origin at sea level. The idealized glacier was partially submerged in oceanic water with a relative water level $\omega = \frac{H_w}{H}$ = 0.75 (H_w is the water height) for all experiments.

The mesh size dependence of the model was tested and showed limited differences in total volume losses for the different mesh sizes (Fig. 3.A.1). It is also important to note that for the various mesh sizes, the modeled geometries displayed similar frontal shapes (Fig. 3.A.2). In order to reduce the computational time, the initial mesh was chosen with 20 elements in the vertical and 200 elements in the horizontal for the sensitivity analyses. The time step dependence of the model was tested and also showed limited differences in total volume losses (Fig. 3.A.3). All model runs were performed for 2000 time steps of $\Delta t = 0.001$ year corresponding to two years of geometry evolution.

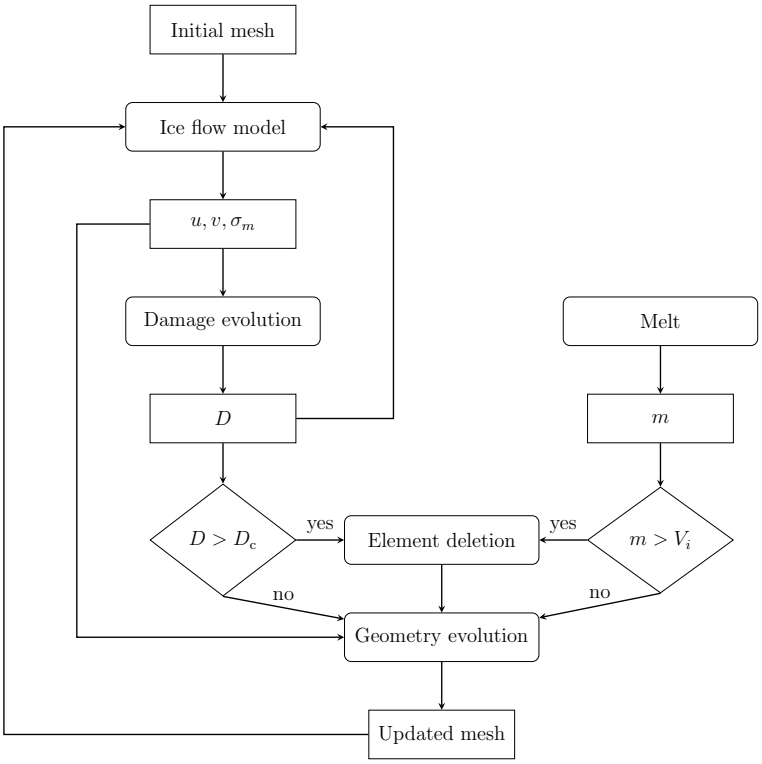

Figure 3.1: Flowchart description of the model steps. Sharp rectangular boxes represent the input and output quantities of the model process-steps. The rounded rectangular boxes show the model processes. The diamond-shaped boxes represent the decision whether elements above a threshold should be deleted. Note that element deletion can occur through an excess of damage without an excess of submarine melt, and conversely through an excess of submarine melt without an excess of damage. The link between the damage variable D output box and ice flow model box represents the viscosity feedback of damage. The variables u, v, σ_m, D_c, m and V_i are the horizontal velocity, vertical velocity, hydrostatic stress, critical damage, accumulated melt rate and initial element volume, respectively

.

First, we describe the ice flow model equations and its boundary conditions. Then we present the continuum damage mechanics model and its coupling to the ice flow model. Finally, we explain the geometry evolution and the calving and melting algorithms.

Table 3.1: Model parameters, notations, units and values for constant parameters.

Parameter	Notation	Value	Units
Fluidity parameter	A	75	$\mathrm{MPa}^{-3}\,\mathrm{a}^{-1}$
Damage rate	B		$\mathrm{MPa}^{-r}\mathrm{a}^{-1}$
Damage	D		
Critical damage	D_c		
Gravitational acceleration	$\boldsymbol{g}$	9.81	$\mathrm{m\,s}^{-2}$
Ice thickness	H		m
Water level height	H_w		m
Melt rate	M		$\mathrm{m\,a}^{-1}$
Glen exponent	n	3	
Damage law exponent	r	0.43	
Velocity vector	$\boldsymbol{u}$		$\mathrm{m\,a}^{-1}$
Healing parameter	h	0	
Hayhurst parameter 1	α	0.21	
Hayhurst parameter 2	β	0.63	
Strain rate tensor	$\dot{\boldsymbol{\varepsilon}}$		a^{-1}
Effective strain rate	$\dot{\varepsilon_e}$		a^{-1}
Melt rate	M		$\mathrm{m\,a}^{-1}$
Effective viscosity	η		MPa a
Finite strain rate parameter	κ_ε	$5.98 \cdot 10^{-6}$	a^{-1}
Ice density	ρ_i	917	$\mathrm{kg\,m}^{-3}$
Sea water density	ρ_w	1028	$\mathrm{kg\,m}^{-3}$
Cauchy stress tensor	$\boldsymbol{\sigma}$		MPa
Maximum principal stress	σ_1		MPa
Effective principal stress	$\sigma_{1,w}$		MPa
Von Mises stress	σ_e		MPa
Von Mises tensile stress	σ_t		MPa
Hayhurst stress	σ_H		MPa
Mean stress	σ_m		MPa
Deviatoric stress tensor	$\boldsymbol{\sigma'}$		MPa
Damage threshold stress	σ_th	0.11	MPa
Stress measure	χ		MPa
Relative water level	ω		

3.2.1 Ice flow model

Ice flow and rheology

Ice flow was computed at each time step on the model domain in an Eulerian reference frame. To model ice flow, we implemented the Stokes equations for incompressible fluid

flow with continuum conservation of momentum and mass

$$\mathrm{div}(\boldsymbol{\sigma}) + \rho_i \boldsymbol{g} = 0\,, \tag{3.1}$$

$$\mathrm{div}(\boldsymbol{u}) = 0\,, \tag{3.2}$$

where $\boldsymbol{\sigma}$ is the Cauchy stress tensor, ρ_i the ice density, $\mathbf{g}$ the gravitational force vector and $\mathbf{u}$ the velocity vector (Tab. 3.1). For isotropic and incompressible ice the Cauchy stress tensor can be decomposed into an isotropic and a deviatoric part $\boldsymbol{\sigma'}$

$$\boldsymbol{\sigma} = \boldsymbol{\sigma'} + \sigma_m \mathbf{I}\,, \tag{3.3}$$

where $\sigma_m = \frac{1}{3}\mathrm{tr}(\boldsymbol{\sigma}) = \frac{1}{3}\sigma_{ii}$ is the mean stress and $\mathbf{I}$ the identity matrix. The undamaged ice rheology is described as a viscous power-law fluid (Glen's flow law), linking the deviatoric stress tensor $\boldsymbol{\sigma'}$ to the strain rate tensor $\dot{\boldsymbol{\varepsilon}}$

$$\boldsymbol{\sigma'} = 2\eta\dot{\boldsymbol{\varepsilon}}\,. \tag{3.4}$$

The effective shear viscosity η is defined as

$$\eta = \frac{1}{2} A^{-\frac{1}{n}} (\dot{\varepsilon_e} + \kappa_\varepsilon)^{\frac{1-n}{n}}\,, \tag{3.5}$$

where $\dot{\varepsilon}_e = \left(\frac{1}{2}\dot{\varepsilon}_{ij}\dot{\varepsilon}_{ij}\right)^{\frac{1}{2}}$ is the effective strain rate, A the fluidity parameter, $n = 3$ the power-law exponent and κ_ε is a regularization parameter that imposes a linear rheology at small strain rates to avoid infinite viscosity at low stresses (Greve and Blatter, 2009).

The model domain was discretized with second-order square, isoparametric nine-node quadrilateral elements with Galerkin weighting. The model variables were approximated with a second-order approximation for the velocities u and v and a first-order approximation for the mean stress σ_m (forming a LBB-stable set).

For each time step, the Stokes equations for ice flow with nonlinear rheology were assembled within libMesh and solved with the PETSc nonlinear solver SNES (Balay et al., 2017) to a relative accuracy of 10^{-4}.

Boundary conditions

In the Eulerian ice flow model, the upper surface of the glacier was described as a traction free boundary. The upstream boundary was treated as a zero velocity Dirichlet boundary condition, independent of the inflow of ice prescribed for the geometry evolution (Sec. 3.2.4), and without effect on the stress field at the terminus.

At the ice/ocean interface, a normal stress boundary condition was imposed below the water level ($z < 0$), while the surface above water was kept traction-free. The stress bound-

ary condition thus reads

$$\begin{aligned} \sigma_{nn} &= \min(\rho_w g z, 0)\,, \\ \sigma_{nt_i} &= 0 \quad (i = 1, 2)\,, \end{aligned} \tag{3.6}$$

where σ_{nn} and σ_{nt_i} are the normal and tangential tractions applied on the calving front and ρ_w is water density (Tab. 3.1). The traction σ_{nn} is compressive (i.e. $\sigma_{nn} < 0$) since $z < 0$ below water.

On the lower boundary of the domain, the type of boundary condition depends on the normal stress $\sigma_{nn} = \boldsymbol{n} \cdot (\boldsymbol{\sigma} \cdot \boldsymbol{n})$. For parts of the boundary where the normal stress exceeds the water pressure ($\sigma_{nn} < \rho_w g z$), a zero velocity Dirichlet boundary condition was imposed. Additional experiments with a zero velocity Dirichlet boundary condition normal to the bed and a prescribed velocity along the bed showed a negligible effect of non-zero velocity boundary conditions on the stress state. On the remaining parts of the bottom boundary the normal stress boundary condition (Eq. 3.6) was imposed, which means that water pressure is applied. The latter condition assumes that there are no cohesive forces restraining the ice movement away from the bed (Durand et al., 2009).

3.2.2 Continuum damage mechanics model

Damage Evolution

Continuum damage mechanics is based on the introduction of a damage variable D. In this study we assume isotropic damage using a scalar variable that represents degradation of mechanical properties at the mesoscale, which averages the accumulation of defects present in the material at the microscale (Lemaitre, 1992). Following the hypothesis of strain equivalence, an effective stress is introduced

$$\tilde{\boldsymbol{\sigma}} = \frac{\boldsymbol{\sigma}}{(1 - D)}\,, \tag{3.7}$$

where D is a state variable that takes the value $D = 0$ in undamaged ice and $D = 1$ when full damage is reached. Damage evolution depends on a stress measure χ and begins once a stress threshold σ_{th} (σ_{th} = 0.11 MPa, Tab. 3.2) is crossed

$$\frac{\partial D}{\partial t} = \max\left(B\left(\frac{\chi}{1 - D} - \sigma_{\mathrm{th}}\right)^r, 0\right) - h\,. \tag{3.8}$$

Damage evolution is parametrized with the damage rate B, the stress measure χ chosen for damage evolution (Sect. 3.2.2), and the power $r = 0.43$ chosen according to Pralong and Funk (2005). A healing term h is easily added, but not considered in this study (i.e. $h = 0$).

Damage evolution on all mesh nodes was calculated by evaluating the stress measure χ based on the solution of the ice flow model at each time step (Fig. 3.1). In our model imple-

mentation damage is a state variable on the nodes of the moving mesh, therefore bypassing the use of an advection scheme that could introduce numerical diffusion of damage.

Stress measure

The stress measure χ for damage evolution should be independent of the choice of coordinate system, and can therefore be expressed as a function of the invariants and eigenvalues of the stress tensor. Our model permits the use of arbitrary linear combinations, and results from a selection shown in the following. Here we list the commonly used stress criteria in glaciological studies (see Tab. 3.2 for a summary of the stress measures and their notations):

- The Hayhurst criterion σ_H is the most widely used stress criterion in glaciological studies for damage evolution (Pralong et al., 2003, Pralong and Funk, 2005, Duddu and Waisman, 2012, 2013, Duddu et al., 2013, Mobasher et al., 2016, Jiménez et al., 2017, Mercenier et al., 2018). This criterion (Hayhurst, 1972) uses a linear combination of the maximum principal stress σ_1, the first stress invariant $I_1 = \sigma_m = \frac{1}{3}\sigma_{ii}$, and the von Mises stress $J_2 = \sigma_e = \sqrt{\frac{3}{2}\sigma'_{ij}\sigma'_{ij}} = \sqrt{3}A^{-\frac{1}{n}}\dot{\varepsilon}_e^{\frac{1}{n}}$ as stress measure χ

$$\begin{aligned} &\sigma_H = \alpha\sigma_1 + \beta\sigma_e + \gamma\sigma_m \,, \\ &0 \leq \alpha, \beta, \gamma \leq 1 \,. \end{aligned} \tag{3.9}$$

  The Hayhurst stress is generally used as a criterion for ductile and brittle materials that allows for damage under uniaxial compression (Pralong and Funk, 2005, Krug et al., 2014).
- The maximum principal stress σ_1 has been used as a stress measure χ in combination with LEFM to simulate calving (Krug et al., 2014). As a stress criterion, the maximum principal stress only represents the purely-tensile contribution, and is therefore useful to locate the position of surface crevasses (Benn et al., 2017, Mercenier et al., 2018). However, without supplementary forcing such as water pressure in cracks, the stresses are compressive close to the bed due to the increasing overburden ice pressure (Krug et al., 2014, Ma et al., 2017) and are likely unable to induce behaviors such as basal crevassing. Combining the maximum principal stress distribution with the effect of water pressure in the submerged parts of the glacier front is suggested to lead to the formation of basal crevasses (Benn et al., 2017). This stress combination, namely the effective principal stress $\sigma_{1,w} = \sigma_1 + P_w$, is also considered in our stress measure analysis ($P_w = \max(-\rho_w g z, 0)$ is the water pressure with $z < 0$ below water).
- The most widely used stress criterion in solid mechanics and structural analysis is the von Mises criterion $J_2 = \sigma_e$ which is a natural quantity to investigate yielding of ductile materials. In glaciology, this criterion has been used to simulate crevasses and fractures on ice shelves (Vaughan, 1993, Albrecht and Levermann, 2014).
- Since calving occurs mainly through stretching (Benn et al., 2007b), the von Mises tensile stress σ_t is additionally considered as a stress measure for damage evolution

(Morlighem et al., 2016). The von Mises tensile stress only takes into account the tensile parts of the von Mises stress and neglects compression. To formulate the von Mises tensile stress, an effective tensile strain rate $\tilde{\dot{\varepsilon}}_e$ is defined

$$\tilde{\dot{\varepsilon}}_e^2 = \frac{1}{2}\left(\max\left(0, \dot{\varepsilon}_1\right)^2 + \max\left(0, \dot{\varepsilon}_2\right)^2\right) \tag{3.10}$$

where $\dot{\varepsilon}_i$ are the eigenvalues of the strain rate tensor. The von Mises tensile stress is then written as

$$\sigma_t = \sqrt{3} A^{-\frac{1}{n}} \tilde{\dot{\varepsilon}}_e^{\frac{1}{n}} . \tag{3.11}$$

Table 3.2: Stress measures and their notations.

Stress measure	Notation
Hayhurst	σ_H
Maximum principal	σ_1
Effective principal	$\sigma_{1,w}$
Von Mises	σ_e
Von Mises tensile	σ_t

Viscosity feedback of damage

The accumulation of micro-defects weakens the ice through damage, which leads to increased deformation rates (Pralong et al., 2003, Pralong and Funk, 2005, Krug et al., 2014). Thus, a damage dependence in the material rheology is introduced, using the equivalence principle of Equation (3.7) for isotropic damage, to describe the rheology of damaged ice (Pralong and Funk, 2005). Practically, the effective shear viscosity was adjusted such that

$$\eta = \frac{1}{2}\left(1 - D\right) A^{-\frac{1}{n}} \left(\dot{\varepsilon}_e + \kappa_\varepsilon\right)^{\frac{1-n}{n}} . \tag{3.12}$$

This equation effectively replaces Equation (3.5) in the ice flow model. The stress and flow regimes for undamaged ice ($D = 0$) remain unaffected while damaged ice is softened, which leads to increased ice deformation rates. Introducing damage thus leads to a positive feedback on the stress and velocity fields. This feedback is represented in the model flowchart (Fig. 3.1) by a direct link between the damage output D box and the ice flow model box.

3.2.3 Submarine melting

Melting of the ice in the submerged parts of the calving front, due to buoyancy-induced heat advection of oceanic water (Howat et al., 2010, Motyka et al., 2013, Straneo and Heimbach, 2013, Straneo et al., 2013, Carr et al., 2013a) is suggested to produce an overhanging ice face below the water line leading to increased calving activity (O'Leary and Christoffersen, 2013, Krug et al., 2015, Benn et al., 2017).

Submarine melting was implemented using a per element state variable m at the boundary between ice and ocean water. In every such element the melt from each side i with length L_i exposed to the oceanic water was accumulated following

$$\frac{\Delta m}{\Delta t} = \sum_i M(x, z, t) L_i \,, \tag{3.13}$$

where $M(x, z, t)$ was the submarine melt rate imposed, which is an arbitrary function of space and time. If the total accumulated volumetric melt m exceeded the initial element volume V_i, the element was removed from the mesh. The excess melt of this element was then evenly distributed among its neighbors. The choice of this implementation method for submarine melt is discussed in Section 3.4.3.

3.2.4 Geometry evolution and calving

At each time step, the velocities $\mathbf{u}$ calculated by the ice flow model were used to update the model geometry. Additionally, a constant horizontal velocity u_{in} was prescribed that corresponds to the upstream inflow of ice into the computational domain, and also served as a uniform basal motion. In the presented results, the ice moves from right to left towards negative x coordinates.

The mesh was modified with the following consecutive steps:

1. Elements in which the damage variable exceeded a threshold D_c were removed from the mesh, as were elements no longer connected to the main mesh (Fig. 3.2). Details are given below.
2. Elements under the water line for which $m > V_i$ were removed from the mesh (Sect. 3.2.3).
3. All mesh nodes were moved by the modeled velocity field $\mathbf{u}\Delta t$.
4. All mesh nodes were additionally displaced by $u_{in}\Delta t$ with $u_{in} < 0$.
5. If the upstream end of the mesh had moved by more than one element length from its original position, a vertical column of elements was added at the upstream end of the domain. The damage variable on these elements was initialized to $D = 0$.
6. The new mesh boundary was scanned and appropriate boundary conditions for the flow model were set.

Iceberg calving was simulated by introducing a critical damage above which the ice was considered too weak. All elements which met the condition $D > D_\mathrm{c}$ were removed from the mesh. This element deletion method is a heuristic approach that allows us to simulate the evolution of the frontal boundary in a simple and efficient way. After this step, groups of elements might exist that are no longer connected to the main mesh, as illustrated in Figure 3.2. A simple search algorithm iteratively traversed the mesh and tagged elements that are connected to either the bed or to a tagged element. The search stopped when no more elements were tagged, and untagged elements were removed from the mesh. The volume of the elements removed due to this algorithm for each time step were considered as

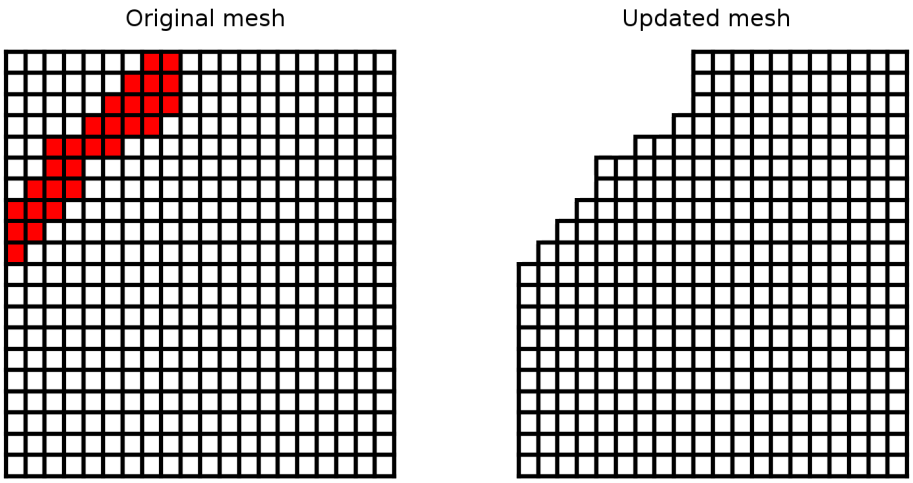

Figure 3.2: Schematic explanation of the calving implementation. Left: In the original mesh the red and white colors represent the elements for which $D > D_c$ and $D < D_c$, respectively. Right: the updated geometry after the elements with $D > D_c$ were removed from the mesh. Note that elements disconnected from the main part of the mesh on the left side of the damaged area were also removed from the mesh.

the volume loss. The calved and melted element volumes were stored for further processing. Note that accumulation/ablation fluxes at the upper surface of the glacier are not accounted for in the geometry evolution.

3.3 Results

In this section, we present the results of the different model sensitivity analyses and the initial adjustment of the calving front. The model formulation allows us to investigate the effect of different stress measures, as well as variations of damage rate B, critical damage D_c, the initial ice thickness and submarine melt.

As a reference experiment, a model run with the von Mises stress σ_e as stress measure, damage rate $B = 5\,\mathrm{MPa}^{-r}\mathrm{a}^{-1}$, critical damage $D_c = 0.5$, initial ice thickness $H = 200\,\mathrm{m}$ and a relative water depth $\omega = 0.75$ was chosen.

Note that for the analysis of the sensitivity experiments our interest is to obtain calving front geometries that are representative of tidewater glacier geometries observed in nature. Calibration of the model parameters with observations would then likely allow us to reproduce the advance and retreat of the calving front positions.

For all experiments presented the initially rectangular calving front adjusts within half a year to a quasi-stable shape. Depending on the model parameters, mainly u_{in}, the front then keeps slightly advancing or retreating at a relatively constant rate (see Movies S1, S2, S3, S4 and S5 in the supporting information). Various influx velocities u_{in} were chosen for the different experiments to compensate for frontal volume loss,therefore constraining the

domain lengths for illustration purposes. It is important to note that the influx velocities do not influence the shape or mass loss evolution of the modeled idealized glaciers.

3.3.1 Choice of stress measure

To investigate the influence of different stress measures on glacier geometry, the coupled model was run for 1000 time steps (1 year) starting from the same geometry the reference parameters (Tab. 3.3). Figure 3.3 and Movie S1 show the geometries for five different stress measures. For the experiments using the von Mises stress σ_e and von Mises tensile stress σ_t an influx velocity of $u_{in} = 2500\,\mathrm{m\,a^{-1}}$ was chosen, whereas $u_{in} = 0\,\mathrm{m\,a^{-1}}$ was used for the other stress measures. For the Hayhurst stress, the linear combination parameters (α, β, γ from Eq. (3.9)) were chosen according to Pralong and Funk (2005).

Table 3.3: Constant model parameters for the stress measure sensitivity experiment.

Parameter	Notation	Value and units
Relative water level	ω	0.75
critical damage	D_c	0.5
Damage rate	B	5 $\mathrm{MPa^{-r}a^{-1}}$
Melt rate	M	0 $\mathrm{m\,a^{-1}}$

The results show distinct model geometry adjustments for the different stress measures (Fig. 3.3 and Movie S1). Using the von Mises σ_e and von Mises tensile σ_t stress, similar calving front geometry evolutions and final shapes were obtained. For these stress measures the damage variable first evolves before a big crevasse forms that penetrates the whole thickness of the glacier at the calving front. The model geometry further evolves and forms an ice foot that regularly breaks off below water. This pattern is particularly pronounced for the von Mises tensile stress where the formation and breaking of the ice foot follows a repeating cycle. Although they have the same influx velocity and damage rate, these two stress measures produce different rates of calving, resulting in a small retreat for the von Mises stress geometry and an advance with the von Mises tensile stress geometry.

For the Hayhurst σ_H and maximum principal stress σ_1 distributions (Fig. 3.3), the damage is only concentrated at the surface and does not penetrate through the whole thickness of the glacier during the model experiment. Elements are only removed at the surface, and most of the ice below the water line remains intact. In reality, however, the damaged ice would likely remain at the surface as it cannot leave the glacier unless it breaks off at the calving front. Further, the influx velocities u_{in} were set to 0 to constrain the length of the domain and limit computation time, as the glacier front continuously advances without breaking off throughout the simulations.

For the Hayhurst stress (Fig. 3.3), in contrast to using the maximum principal stress, the rapidly forming floating tongue is detached further away from the bed and more ice is removed at the top surface. Further, if we take the water pressure in the submerged parts of the

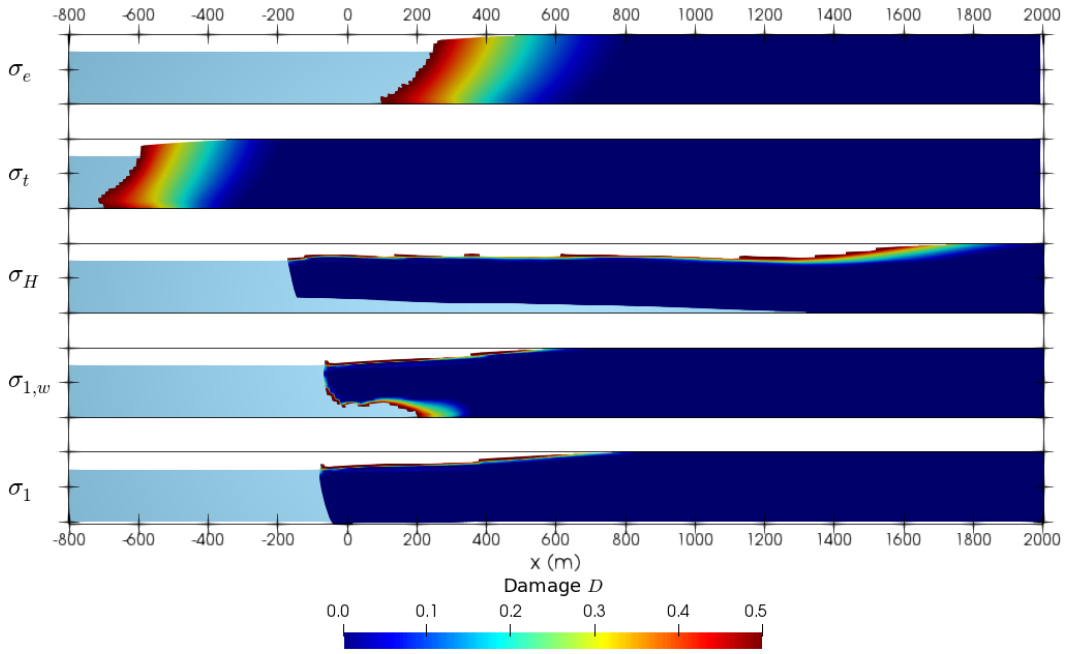

Figure 3.3: Model geometry and damage distribution after one year for different stress measures, labeled on the left. The dark lines show the bed and maximum thickness for each geometry. Light blue indicates ocean.

calving front into account using the effective principal stress measure $\sigma_{1,w}$, the elements at the front and below the floating tongue are progressively removed from the mesh during the simulations. However, damage does not penetrate through the whole thickness upstream of the glacier tongue.

In this study, we aim at providing a model with realistic tidewater glacier behavior such as regular calving and realistic terminus geometries. For the purpose of illustrating the model capabilities, we therefore restrict ourselves to the von Mises stress measure σ_e. Only future analysis of the sparse field data with this model will allow us to identify the most suitable stress measures together with model parameters.

3.3.2 Influence of critical damage

Figure 3.4 and Movie S2 illustrate the quasi-stable geometries obtained from the coupled model after 1000 time steps (1 year) with a critical damage $D_c \simeq 1$ (with $u_{in} = 2000\,\mathrm{m\,a^{-1}}$) and $D_c = 0.5$ (with $u_{in} = 2500\,\mathrm{m\,a^{-1}}$). The model parameters for these experiments are shown in Table 3.4.

Table 3.4: Constant model parameters for the critical damage sensitivity experiment.

Parameter	Notation	Value and units
Relative water level	ω	0.75
Influx velocity	u_{in}	2500 $\mathrm{m\,a^{-1}}$
Damage rate	B	5 $\mathrm{MPa^{-r}a^{-1}}$
Melt rate	M	0 $\mathrm{m\,a^{-1}}$
Stress measure	σ_e	

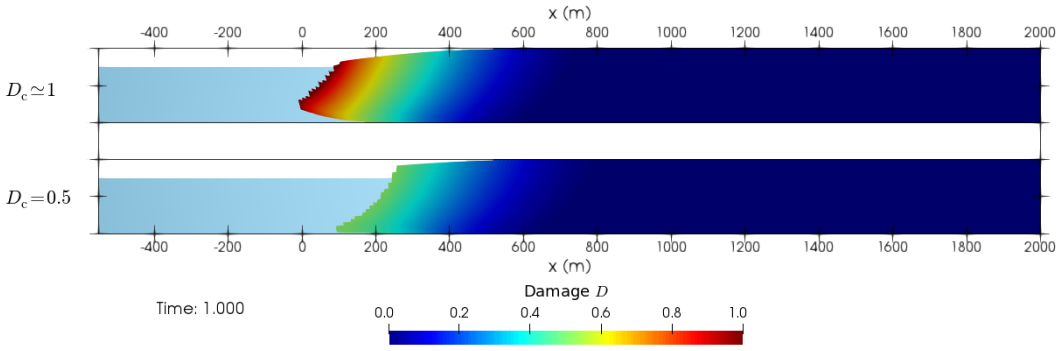

Figure 3.4: Model geometry and damage distribution after one year for different critical damages D_c, labeled on the left. The dark lines show the bed and maximum thickness for each geometry. Light blue indicates ocean. Note the use of a rescaled color bar in this Figure to show the full range of critical damage values tested.

Increasing the critical damage leads to a slower mass loss due to ice break-off at the calving front (Fig. 3.4, 3.A.4 and Movie S2). Further, the resulting geometries differ slightly, with a more pronounced buoyancy driven rise for the fully damaged geometry ($D_c \simeq 1$) and an ice foot closer to the bed for the lower critical damage ($D_c = 0.5$).

3.3.3 Influence of damage rate

Figure 3.5 and Movie S3 show the geometries obtained from the coupled model after 1000 time steps (1 year) with different damage rates B. Table 3.6 shows the model parameters that were chosen for all experiments.

Table 3.5: Constant model parameters for the damage rate sensitivity experiment.

Parameter	Notation	Value and units
Relative water level	ω	0.75
Influx velocity	u_{in}	2000 $\mathrm{m\,a^{-1}}$
Critical damage	D_c	0.5
Melt rate	M	0 $\mathrm{m\,a^{-1}}$
Stress measure	σ_e	

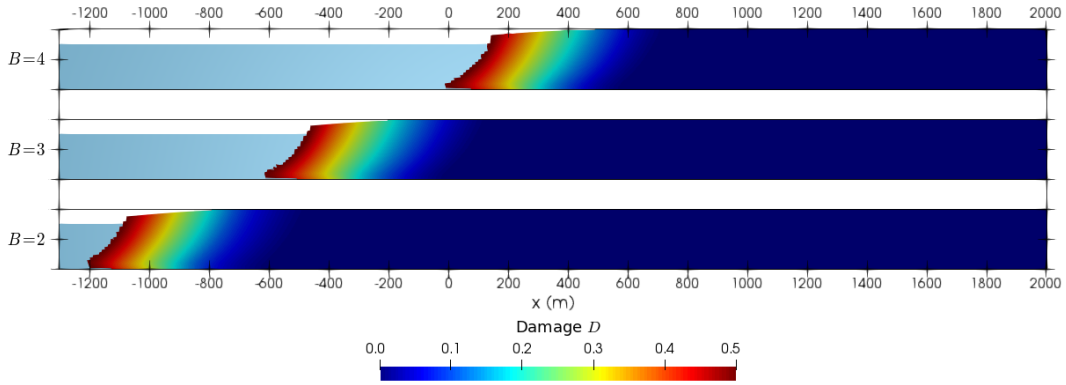

Figure 3.5: Model geometry and damage distribution after one year for different damage rates B ($\mathrm{MPa}^{-r}\mathrm{a}^{-1}$), labeled on the left. The dark lines show the bed and maximum thickness for each geometry. Light blue indicates ocean.

Varying the damage rate appears to change the position of the calving front, as a result of different calving rates, rather than the geometrical properties of the calving front (Figs. 3.5, 3.A.5 and Movie S3). The model experiments follow the same geometrical evolution of the calving front, with a certain time lag due to the different damage rates. All geometries develop the distinctive inclined calving front with an ice foot developing below the water level. Thus, increasing the damage rate leads to a long-term higher rate of mass loss due to enhanced ice break-off at the calving front but the effect on the calving front geometry is limited.

3.3.4 Influence of ice thickness

The stability of the glacier front strongly depends on the ice thickness and water depth (Brown et al., 1982, Bassis and Walker, 2012, Mercenier et al., 2018). Therefore, we performed sensitivity tests on the ice thickness of the initial mesh. The element size was kept identical for the different experiments, with initial square element dimensions of $10\,\mathrm{m} \cdot 10\,\mathrm{m}$. For the ice thicknesses of $H = 250\,\mathrm{m}$, $H = 200\,\mathrm{m}$ and $H = 150\,\mathrm{m}$, the influx velocities were set to 5000 ma^{-1}, 2500 ma^{-1} and 1000 ma^{-1}, respectively. The initial length L of the geometries was set to $L = 10\,H$. Table 3.6 shows the model parameters selected for the ice thickness sensitivity experiments.

Table 3.6: Constant model parameters for the ice thickness sensitivity experiment.

Parameter	notation	Value and units
Relative water level	ω	0.75
Damage rate	B	5 MPa^{-r} a^{-1}
Critical damage	D_c	0.5
Melt rate	M	0 $\mathrm{m\,a}^{-1}$
Stress measure	σ_e	

In a similar way as for the damage rate sensitivity analysis, increasing the initial ice thickness leads to a higher rate of mass loss due to ice break off at the calving front, with a limited effect on the calving front geometry (Fig. 3.6 and Movie S4). Though it appears in Figure 3.6 and Movie S4 that the thicker geometry loses mass at a lower rate, note that the constant horizontal velocities imposed strongly differ. The thicker glacier actually starts to lose mass earlier than the thinner glaciers and continues to lose mass at a higher rate (Fig. 3.A.6). Similar geometries are developed for all ice thicknesses, with a certain delay due to the different rates of mass loss.

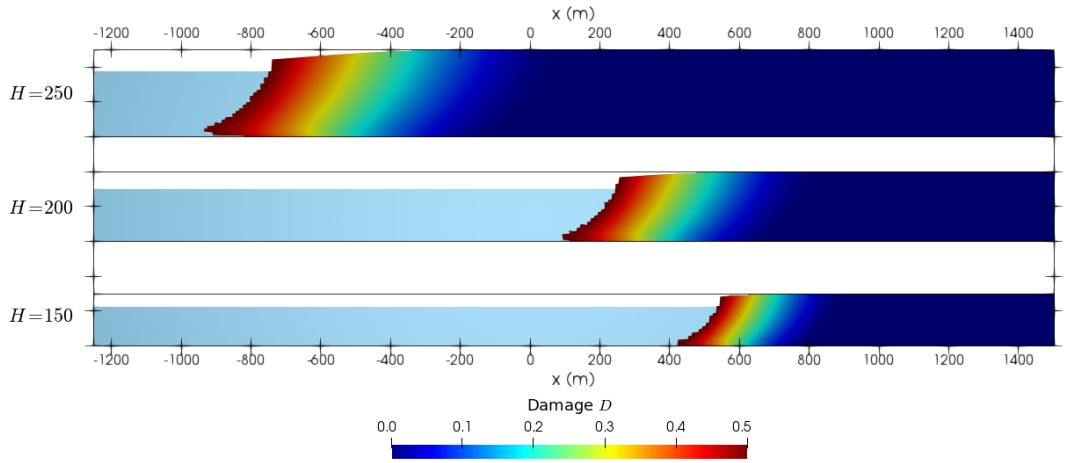

Figure 3.6: Model geometry and damage distribution after one year for different initial ice thicknesses H (m), labeled on the left. The dark lines show the bed and maximum thickness for each geometry. Light blue indicates ocean. The geometries have been cut-off at $x = 1500\,\mathrm{m}$. For $H = 200\,\mathrm{m}$ and H=250 m, the domains extend to 2000 and 2500 m, respectively. Note that for the ice thicknesses of $H = 250\,\mathrm{m}$, $H = 200\,\mathrm{m}$ and $H = 150\,\mathrm{m}$, the influx velocities were set to 5000 ma^{-1}, 2500 ma^{-1} and 1000 ma^{-1}, respectively.

For the purpose of this model description study, the thicknesses were limited to a maximum of 250 m in our modeling effort. The relative water depth ω was kept constant for the ice thickness experiments. However, further experiments using various relative water depths showed similar geometry evolutions as for the different ice thicknesses (Fig. 3.A.7), with a higher rate of frontal mass loss for smaller values of ω.

3.3.5 Influence of submarine frontal melt

Figure 3.7 and Movie S5 show the geometries obtained from the coupled model after 1000 time steps (1 year) for different melt scenarios. The reference parameters for all experiments are displayed in Table 3.7. A constant melt rate M, independent of time and depth, is prescribed below the water line where melt is accumulated in the frontal elements following Equation (3.2.3). More realistic melt parametrizations could easily be prescribed.

Table 3.7: Constant model parameters for the submarine melt experiment.

Parameter	Notation	Value and units
Relative water level	ω	0.75
Critical damage	D_c	0.5
Damage rate	B	2 $\mathrm{MPa}^{-r}\mathrm{a}^{-1}$
Stress measure	σ_e	
Influx velocity	u_{in}	1000 $\mathrm{m\,a}^{-1}$

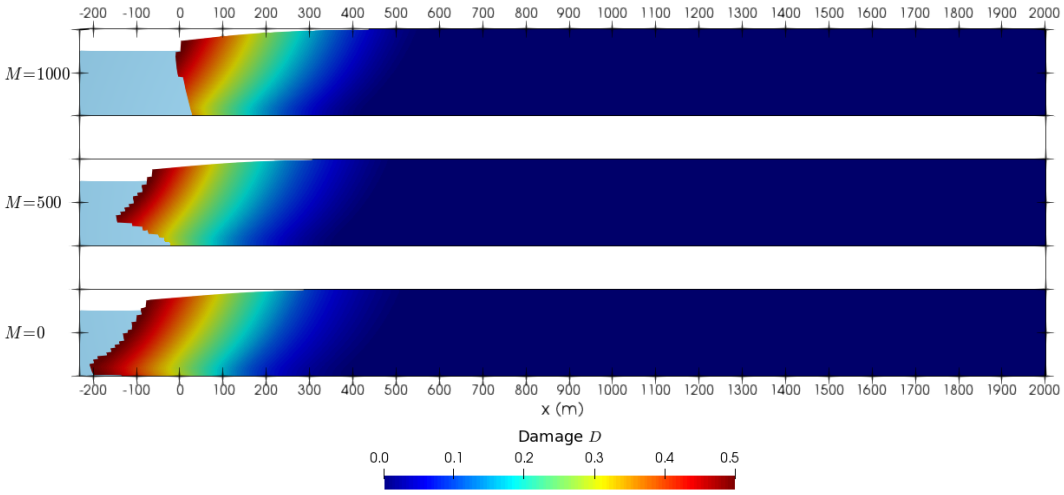

Figure 3.7: Model geometry and damage distribution after one year for different melt rates M ($\mathrm{m\,a}^{-1}$). The dark lines show the bed and maximum thickness for each geometry. Light blue indicates ocean.

The melt rate sensitivity analysis shows that submarine melt strongly affects the shape of the calving front (Fig. 3.7 and Movie S5). For the experiment with $M = 1000\,\mathrm{m\,a}^{-1}$ the front progressively develops a calving front that is over-steepened below the water line. During the first year of simulation, increasing the melt rate leads to a faster retreat of the calving front. However, once the calving front shape has adjusted itself after one year, mass loss occurs faster when submarine frontal melt is neglected (Fig. 3.A.8).

3.4 Discussion

The coupled ice flow-calving model presented in this study is capable of producing different geometries typically encountered in tidewater glaciers (Figs. 3.3 to 3.7) and different calving styles by only varying a set of parameters and forcings. The dependence of model performance and glacier evolution on these parameters, and avenues for validating the model with measurements, are elaborated in the following sections.

3.4.1 Retreat and advance

The calving front evolution is essentially controlled by four processes acting on different time scales: ice deformation, damage evolution, frontal melt and basal sliding. Understanding these time scales is crucial as they determine the rate of advance and retreat of the glacier front. Basal sliding and ice deformation determine the mass flux and thus affect the rate of advance of the glacier, while damage evolution and submarine melt control the calving rate and hence retreat.

While melt and inflow from upstream are external forcings, damage evolves at its own time scale, driven by mechanical stress and thus the glacier geometry. Damage evolution leads to two processes with different time scales: sub-aerial break-off and break-off below water. The latter process is an order of magnitude slower due to the effective gravity (buoyant force) under water of magnitude $(\rho_w - \rho_i)/\rho_i\, g \simeq 0.12\, g$ and accordingly reduced deviatoric stresses.

The model results show that the shapes of the calving front obtained by varying the damage parameters remain very similar (Fig. 3.5). Thus, these parameters determine the time scales at which break-off occurs at the calving front in the coupled model rather than the shape of the calving front. The ice thickness variations exhibit a similar effect on the time scale of glacier geometry evolution (Fig. 3.6).

In order to reproduce observed rates of mass loss at the calving front the calibration of the critical damage and damage rate parameter are required, and the submarine melt rate would have to be prescribed.

3.4.2 Stress measures and calving front geometries

The choice of stress measure has a strong influence on the modeled calving front geometry. All our modeling experiments reproduce a vertical ice cliff above the water line (Fig. 3.3), a feature that is commonly observed at calving glaciers (Benn et al., 2007b). In contrast, below the water line the modeled geometries show large differences for the different stress measures.

A noteworthy feature that is common to all model runs with von Mises stress measure is the presence of an ice foot below the water line. The development of subaqueous ice feet, which have been observed for a series of calving glaciers (Warren et al., 1995, Motyka, 1997, Hunter and Powell, 1998, O'Neel et al., 2007), can be caused by calving losses above the water line exceeding those below (Benn et al., 2007b). Buoyant forces then induce a rotation of the terminus either by ice creep or fracture propagation and calving (Warren et al., 2001, Benn et al., 2007b). This process can clearly be observed in our model experiments involving the von Mises stress. However, this process is expected to be much slower than aerial calving since the buoyancy forces are ~ 9 times smaller than gravitational forces, leading to an order-of-magnitude lower effective upward gravity and accordingly reduced stresses. Indeed, in our model subaqueous calving events are less frequent but of larger magnitude than above

water (Movie S1), in agreement with observations (Warren et al., 1995, Motyka, 1997, Hunter and Powell, 1998, O'Neel et al., 2007).

The underwater geometry has been investigated only for a few marine-terminating glaciers. Recent studies using multi-beam bathymetry in West Greenland revealed undercut ice faces below the water line as well as ice foot formations (Fried et al., 2015, Rignot et al., 2015). The observed glacier undercuts were larger at the sites of subglacial water discharge from the glacier. Buoyant plumes of subglacial water transport the warm oceanic water to the ice face, and consequently enhance the local melt rate (Rignot et al., 2015, Slater et al., 2016). In the presented model runs, the persistent presence of an ice foot at the calving front could therefore be explained by the lack of undercutting by melt and the absence of pre-existing cracks near the bed of the partly grounded glacier. As shown in Section 3.3.5, undercutting by submarine melt has a significant impact on the underwater calving front geometry as the ice foot is melted away while it forms. Further, the pre-existence of cracks at the bed, due to irregularities in the bed for example, would be expected to increase damaging and reduce the formation of an ice foot.

Model runs with the Hayhurst and maximum principal stress show damage concentration at the top surface rather than at the bed of the glacier. Therefore, cracks do not penetrate through the whole ice thickness and elements are deleted only at the top surface. In reality such ice might not be removed from the glacier as it is in our model implementation (Sect. 3.3.1). The lack of depth penetration is likely due to the importance of the overburden ice pressure at depth which exceeds the tensile and shearing stress components. The no-slip basal boundary condition could further explain the lack of depth penetration, as free slip boundary conditions led to full-thickness calving using the maximum principal stress (Ma et al., 2017).

Based on the above considerations, the von Mises and von Mises tensile stresses produce the most realistic calving front geometry evolutions for tidewater glaciers using a continuum damage mechanics model. This observation agrees with results from Choi et al. (2018) who found that the von Mises tensile stress provides more satisfactory results than the three other calving laws in their comparison effort.

Combining the maximum principal stress with the effect of water pressure in the submerged parts of the glacier, i.e using the $\sigma_{1,w}$ stress measure, led to the formation of a floating ice tongue but cracks at the surface and the bed were still not able to penetrate through the whole thickness of the glacier (Fig. 3.3 and Movie S1). However, the presence of surface water would likely facilitate crevasse propagation through the whole thickness of the glacier (Benn et al., 2007b). Including the effect of such a process into the model with these stress measures would likely be effective in reproducing ice shelf disintegration.

3.4.3 Submarine melt

The submarine melt parametrization used in this study is simple, with a continous and depth-independent melt. However, any arbitrary melt parametrization as a function of position and time can be prescribed in the presented model.

Implementing submarine melt at the calving front in a Lagrangian reference frame without a rediscretization scheme presents some challenges. While the implementation of oceanic melt used in this study is straightforward, it neglects certain effects caused by submarine melting. For instance, small geometrical changes of the calving front due to melt are neglected until the elements at the water boundary are removed. Conversely, a more accurate description of melt would first lead to a reduction of the size of the elements in contact with water before they are removed. Therefore, the length of the sides in contact with water are likely underestimated during the melt accumulation process, leading to an underestimation of melt with respect to the imposed melt rate. Further, the effect of these progressive geometrical changes on the stress state, during the melt accumulation process, at the calving front is also partially neglected. These shortcomings are mesh-size dependent and negligible for small elements.

During model development, a potential improvement to the method described above was implemented, but ultimately discarded. By moving the nodes in contact with the water according to the imposed melt at each time step, the size reduction of the elements in contact with water was tracked. This approach presents, however, some implementation issues. First, the solution of the damage distribution has to be remapped to the updated nodal positions of the shrinking elements. Second, the element shape often became very distorted when nodes were moved due to melt. These element distortions can cause convergence issues due to the presence of negative eigenvalues of the element Jacobian matrix. To remedy this issue, the distorted elements can be removed as soon as the element quality is too low. With such an approach, elements would be removed that are not fully melted which would lead to a non-negligible overestimation of melt. Therefore, we decided to use the simple melt accumulation implementation presented before.

Undercutting by melt below and at the water line is generally suggested to lead to an increase in calving activity, resulting from the formation of an overhang in the submerged parts of the calving front (Motyka et al., 2013, O'Leary and Christoffersen, 2013, Petlicki et al., 2015, Benn et al., 2017, How et al., 2019). Indeed, such an overhang under the water line forms for the model experiment with a melt rate of $1000\,\mathrm{m\,a^{-1}}$ (Fig.3.7). However, the long-term calving activity appears to be larger for the experiment without submarine melt. Therefore, the effect of melt-undercutting on the rate of calving is not yet clear from our experiments. A detailed investigation will be necessary to understand the effect of modeled submarine melt on the calving rate.

3.4.4 Model improvements

The coupled ice flow-calving model was applied only to an idealized glacier geometry. For arbitrary tidewater glacier geometries and comparison with data, several adaptations are needed. Basal motion, now implemented as simple forward movement of mesh nodes, would be implemented as a frictional boundary with potential dependence on effective water pressure (e.g., Ryser et al., 2014a). Ice flux into the model domain at the upstream boundary could be adapted in a straight-forward manner to include variable vertical extent. Moreover, the evolution of the glacier over arbitrary bedrock geometries could induce local damage effects that might influence the calving front patterns.

The presented model was implemented in plane-strain formulation in a vertical section along the flow line. Consequently, important effects such as lateral stress bridging are neglected (Todd et al., 2018, Choi et al., 2018). The current model implementation is generic and can be used in three dimensions by only changing the finite element types to three-dimensional hexahedral or tetrahedral elements. Computational costs would be much higher, which is alleviated by the fully parallel implementation of the libMesh finite element library and the employed PETSc solvers.

3.5 Conclusions

We developed a transient model of coupled damage evolution and ice flow to simulate ice break-off at the calving front of a tidewater glacier. A coupled Euler-Lagrange formulation was used for the model evolution, combined with the heuristic removal of elements at the calving front representing calving and oceanic melt, and addition of elements at the upstream influx boundary. The model therefore incorporates the main processes affecting tidewater glacier evolution and can be used to investigate the relative importance of individual processes, their time scales and their intricate coupling.

The discussed model runs all started from an idealized geometry, and evolved to a wide range of geometries and calving dynamics which resemble those observed on tidewater glaciers. The emergent modeled calving front geometries and calving rates depend delicately on the choice of the stress measure and further model parameters, and oceanic melt. For a chosen stress measure the calving rate and hence the rate of advance and retreat of the glacier depends on the damage rate and basal sliding. Our analysis suggests that the von Mises stress measures produce the most realistic calving front geometry evolutions.

Undercutting by melt has a significant impact on the calving front geometry. However, more detailed investigations are needed to understand the effect of submarine melt on the calving rate. Calibration of the model parameters with observations will be necessary to reproduce calving rates and frontal positions from real tidewater glaciers.

Acknowledgments

The libMesh library is a C++ framework for the numerical simulation of partial differential equations on serial and parallel platforms available at `http://libmesh.github.io/` (Kirk et al., 2006). Data from this study can be obtained from `https://doi.org/10.5281/zenodo.1492244`

This work was funded by the Swiss National Science Foundation Grant 200021-156098.

The authors declare that they have no conflict of interest.

3.A Appendix

3.A.1 Mesh size dependence of the model

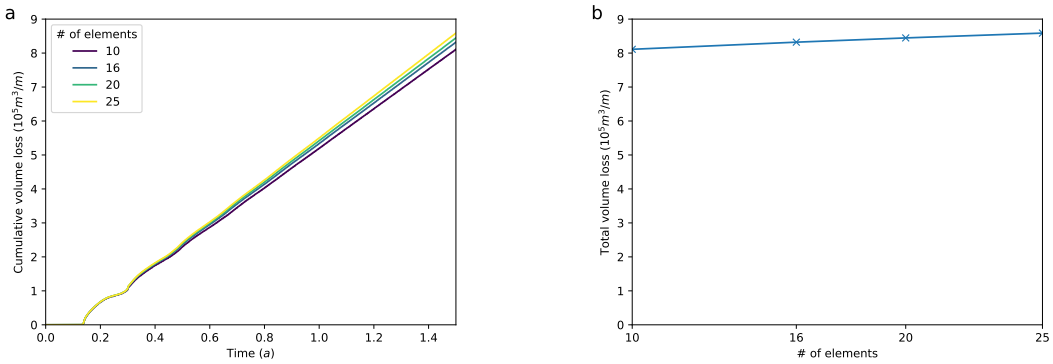

Figure 3.A.1: (a) Volume losses over time and (b) total volume losses for meshes with different numbers of elements in the vertical dimension after 1.5 years of simulation.

3.A.2 Model geometries for different mesh sizes

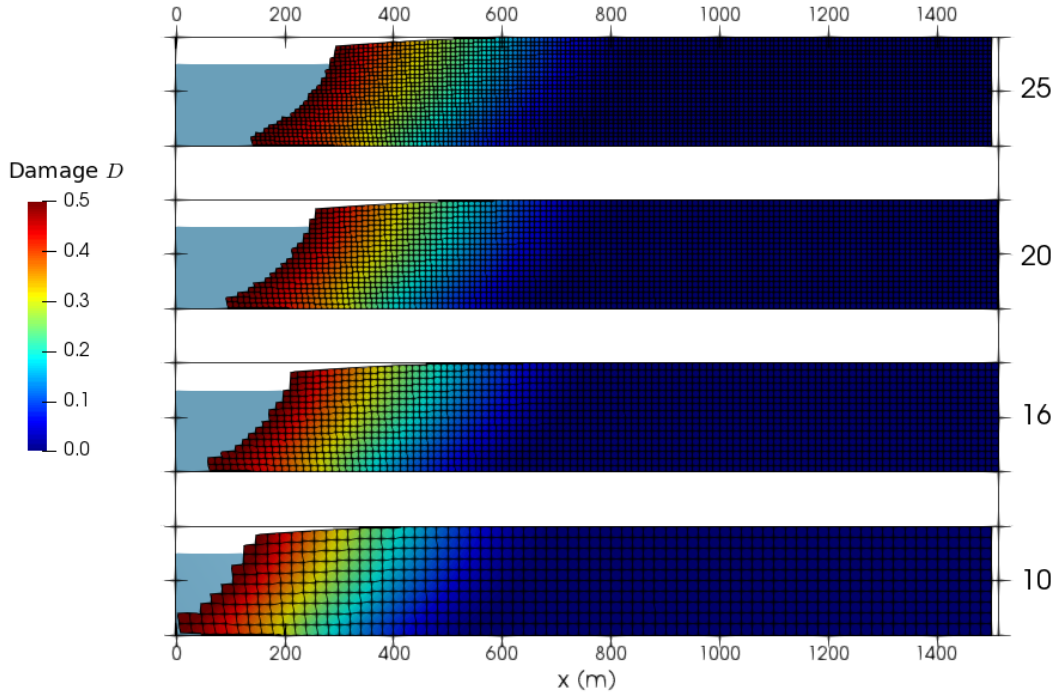

Figure 3.A.2: Snapshot of the modeled geometries after one year of simulation for different mesh sizes (labeled on the right). The dark lines show the bed and maximum thickness for each geometry. Light blue indicates ocean.

3.A.3 Time step dependence of the model

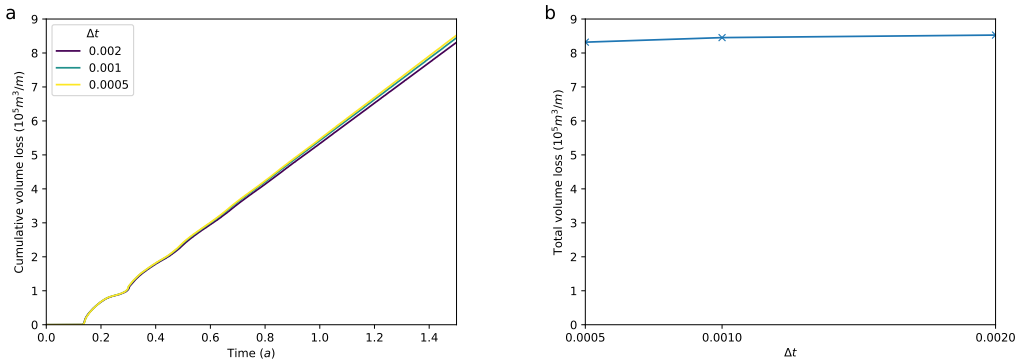

Figure 3.A.3: (a) Volume losses over time and (b) total volume losses for different time steps Δt (a) after 1.5 years of simulation.

3.A.4 Volume loss over time for different critical damages

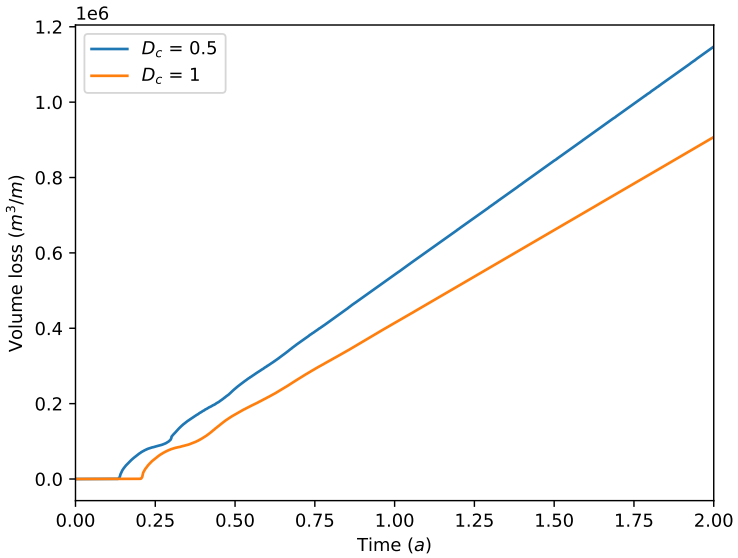

Figure 3.A.4: Volume loss over time for different critical damage D_{c}.

3.A.5 Volume loss over time for different damage rates

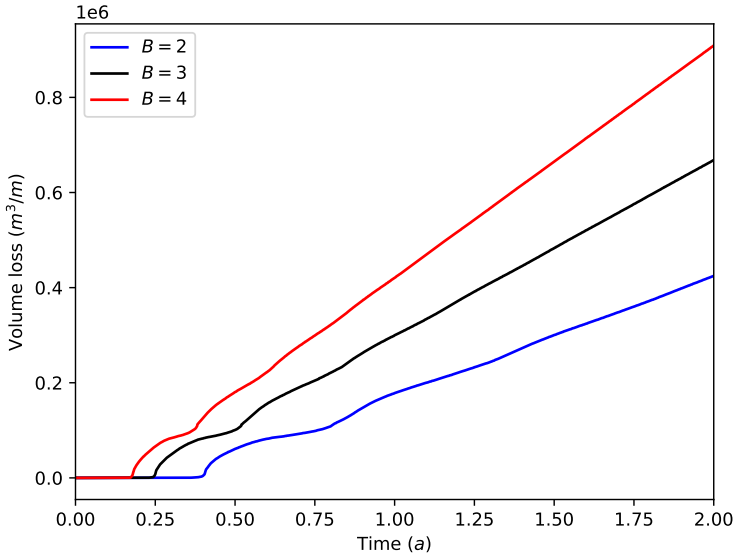

Figure 3.A.5: Volume loss over time for different damage rates B (MPa^{-r}a^{-1}).

3.A.6 Volume loss over time for different ice thicknesses

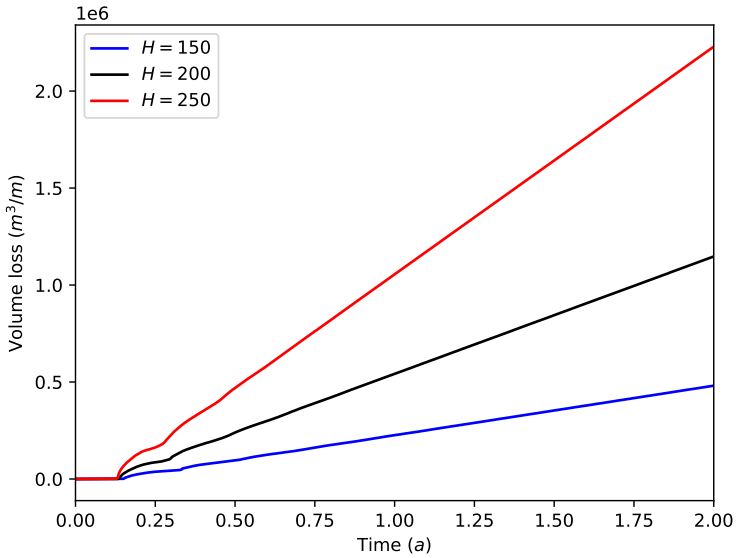

Figure 3.A.6: Volume loss over time for different ice thicknesses H (m).

3.A.7 Model geometry after one year for different relative water depths

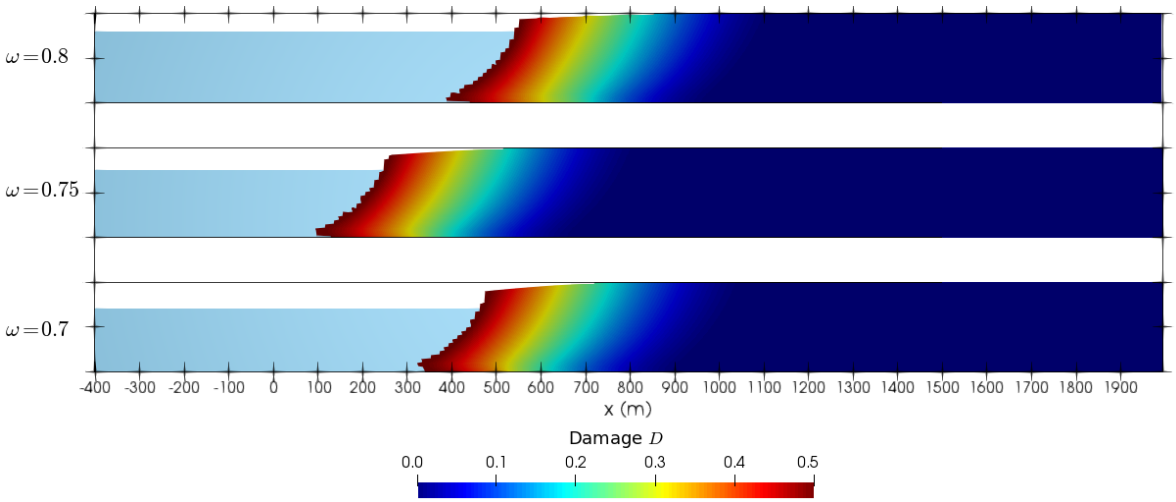

Figure 3.A.7: Model geometry and damage distribution after one year for different relative water depths ω, labeled on the left. The dark lines show the bed and maximum thickness for each geometry. Light blue indicates ocean. Note that the influx velocity u_{in} is 2000 m a^{-1} for $\omega = 0.8$ and 2500 m a^{-1} for the lower ω.

3.A.8 Volume loss over time for different melt rates

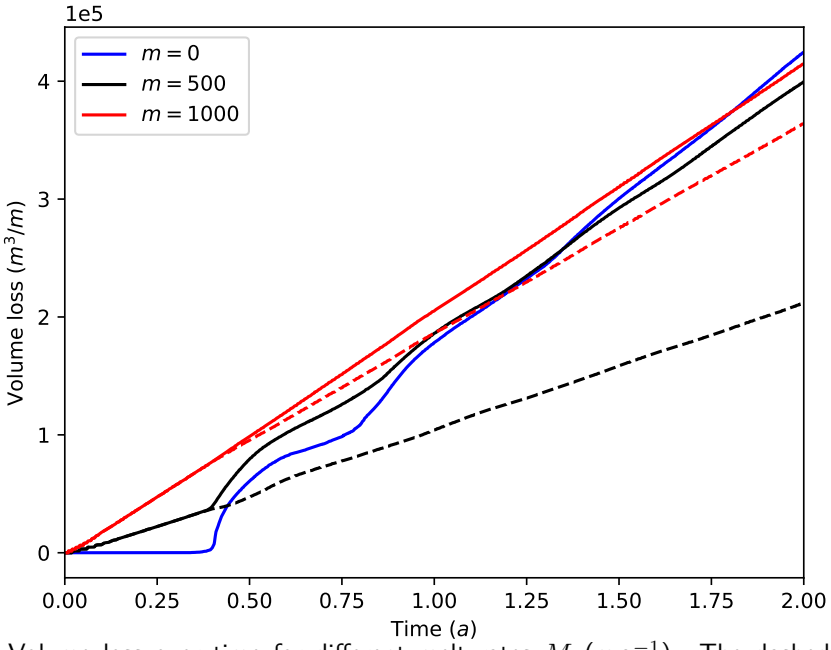

Figure 3.A.8: Volume loss over time for different melt rates M (m a^{-1}). The dashed lines show the volume loss occurring through melting alone and the solid lines show the total volume loss.

4 How oceanic melt controls tidewater glacier retreat

Citation Mercenier, R., Lüthi, M. P., and Vieli, A.: How oceanic melt controls tidewater glacier evolution, Geoph. Res. Lett., in review, 2019b.

Short summary The current rapid retreat of ocean-terminating glaciers of the Greenland ice sheet has been attributed to increased advection of warm ocean currents into the glacial fjords. Submarine melt is generally assumed to result in the formation of an over-steepening calving front and therefore increased stresses and calving activity. However, the relationship between oceanic melt and iceberg calving may not be as straightforward as previously thought, with a potential suppressing effect on iceberg calving with oceanic melt. A transient calving model that couples ice break-off and oceanic melt is employed to investigate the relationship between these two processes, and its consequential effect on tidewater glacier evolution.

Main findings The Mercenier et al. (2019b) study major findings are:

- While high melt rates lead to large volume losses, intermediate melt rates induce volume losses that are lower than those attained without oceanic melt.
- The complex relationship between the ice fracturing and oceanic melt processes, and their effect on the calving front geometry evolution highlights the necessity to consider the two processes as tightly coupled.
- Simple additive parametrizations of calving and oceanic melt are not able to capture the essential complexity of tidewater glacier evolution.

Contributions of the author The author performed the model sensitivity analysis to increasing melt rates with the different implementations. The author wrote the manuscript with the help of the co-authors, designed all graphics and was in charge of the paper publication.

Data availability Data from this study can be obtained from `https://doi.org/10.5281/zenodo.2677937`.

Journal *Geophysical Research Letters (GRL)*
Impact Factor: **4.34**

Abstract

The recent rapid retreat of many Greenland outlet glaciers has been attributed to increased oceanic melt, but the relationship between oceanic melt and iceberg calving remains poorly understood. Here, we employ a transient finite-element model that simulates oceanic melt and ice break-off at the terminus. The response of an idealized tidewater glacier to various submarine melt rates and seasonal variations is investigated. Our modeling shows that for zero to low oceanic melt, the rate of volume loss at the front is similar or higher than for intermediate oceanic melt rates. Only very high melt rates lead to increasing volume losses. These results highlight the complex interplay between oceanic melt and calving and question the general assumption that increased submarine melt leads to higher calving fluxes and enhanced retreat. Models for tidewater glacier evolution should therefore consider calving and oceanic melt as tightly coupled processes rather than as simple, additive parametrizations.

4.1 Introduction

The current rapid retreat of ocean-terminating glaciers of the Greenland ice sheet has been attributed to increased advection of warm ocean currents into the glacial fjords (e.g., Holland et al., 2008, Straneo and Heimbach, 2013, Luckman et al., 2015, Slater et al., 2018). Subaqueous melt erosion at the glacier terminus by warm water is generally assumed to result in the formation of an over-steepened calving front and therefore increased stresses and calving flux (Motyka et al., 2013, O'Leary and Christoffersen, 2013, Benn et al., 2017). This implies that increased oceanic melt drives enhanced volume loss through calving, which is also exploited in simple parametrizations of frontal ablation in models for tidewater glacier evolution (Bondzio et al., 2016, Morlighem et al., 2016, Amundson and Carroll, 2018). In a recent sophisticated modeling study, Todd et al. (2018) also demonstrated a direct influence of submarine melting on the evolution of Store Glacier. However, their approach only allowed for a fully vertical calving front after ice break-off, and any buoyant submerged ice was removed as soon as it formed, which is not fully consistent with observations (Warren et al., 1995, Motyka, 1997, Hunter and Powell, 1998, O'Neel et al., 2007, Sugiyama et al., 2019). Other studies have demonstrated that melt-undercutting has a limited effect on calving rates (Cook et al., 2014, Krug et al., 2015). Ma and Bassis (2019) found both an enhancing and a suppressing effect of melt on calving, depending on magnitude and vertical distribution of melt, but their simulation was limited to the onset phase of one calving event. Our own preliminary experiments with a transient Lagrangian ice-flow and damage-based calving model showed similar effects and also indicated that the relationship between submarine melt and iceberg calving may not be as straightforward as generally assumed (Mercenier et al., 2019a). That study lacked a systematic investigation of the influence of oceanic melt rates on calving flux and frontal volume loss.

In this paper, we aim at a better understanding of the link between oceanic melt, iceberg calving and volume loss for a tidewater glacier geometry that evolves over several years. We use a transient Lagrangian finite-element ice flow model that simulates ice break-off using a damage evolution law combined with the application of oceanic melt at the calving front. We investigate the response of an idealized glacier to variations of oceanic melt rate. The effects of seasonality and variations of oceanic melt rate with depth on the volume loss are evaluated.

4.2 Methods

We employ the transient Lagrangian multi-physics calving model developed in Mercenier et al. (2019a) in two and three dimensions. This model is implemented using the libMesh finite-element library (Kirk et al., 2006). Ice flow is calculated solving the Stokes equations for incompressible fluid flow with power-law rheology (Glen's flow law). Material damage D is implemented as an evolving state variable (Pralong and Funk, 2005)

$$\frac{\partial D}{\partial t} = \max\left(B\left(\frac{\chi}{1-D} - \sigma_{\mathrm{th}}\right)^{r}, 0\right) - h\,. \tag{4.1}$$

that varies according to the damage rate B, a stress measure χ chosen for damage evolution, a stress threshold σ_{th}, the power r and a healing term h (for parameter settings, see Tab. S1). Damage in the ice affects its viscosity η

$$\eta = \frac{1}{2}\,(1-D)\,A^{-\frac{1}{n}}(\dot{\varepsilon_e} + \kappa_\varepsilon)^{\frac{1-n}{n}}\,. \tag{4.2}$$

with A the fluidity parameter, $\dot{\varepsilon_e}$ the effective strain rate, $n = 3$ the Glen's flow law exponent and κ_ε a regularization parameter. Therefore, damaged ice is softened while undamaged ice remains unaffected ($D = 0$) and a feedback between damage and the stress and velocity field is created. The model is fully Lagrangian with the state variables stored on the mesh nodes, which allows us to avoid numerical diffusion issues as no advection problem needs to be solved. Details are given in Mercenier et al. (2019a).

The model geometry is evolved over time in equal time steps calculating the velocity field and stresses. The state variable "damage" is updated according to Equation (4.1), and elements in contact with the ocean accumulate melt according to their interface area and oceanic melt rate. Ice removal by break-off (calving) and ocean melt is simulated with element extinction once accumulated damage exceeds a critical value or melt accumulation exceeds the element volume. The mesh nodes are subsequently moved according to nodal velocities yielding a deformed geometry. The whole domain is then horizontally moved at a constant speed u_{in}, which is chosen for each experiment to compensate average ice loss and to obtain a stationary calving front position. This horizontal movement does not influence the shape or volume loss of the modeled glaciers. The gap created at the upstream boundary by the

horizontal movement is filled with new undeformed elements with their state variables set to zero. Details are given in Mercenier et al. (2019a).

The damage evolution law (Eq. 1) was tested with different types of stress measure (Mercenier et al., 2019a, Eq. 8). Damage evolves when the stress measure exceeds a threshold σ_{th}, leading to ice weakening and ultimately failure. From all tested stress measures, only the "von Mises" and "von Mises tensile" stress measures produced realistic calving front geometries and significant calving activity (Mercenier et al., 2019a). The von Mises stress is thus used throughout this study.

Starting from a rectangular block geometry, all model runs evolved for 5 years with 5000 time steps of 0.001 year. The initial domain consisted of a simple geometry of 2000 m length and 200 m thickness, discretized with quadratic isoparametric Q2Q1 elements at a spatial resolution of $10\,\mathrm{m}$. The water depth for all runs was set to $H_w = 150\,\mathrm{m}$ and the other model parameters are given in Table S1. The ice volume losses occurring through oceanic melt and calving were tracked separately to facilitate the analysis.

Different types of oceanic-melt experiments were performed by varying the oceanic melt rate magnitude, its seasonality, and its vertical pattern. Combinations of melt forcing parameters and their corresponding designations are listed in Table S2 and labeled with corresponding abbreviations. Oceanic melt rate was either continuously applied at a prescribed value (denoted as C) or seasonally switched on and off (denoted as S). The maximum melt rate M was varied between 0 and 1500 $\mathrm{m\,a^{-1}}$ in intervals of 250 $\mathrm{m\,a^{-1}}$ (denoted as Mx with x being the applied melt rate) which covers the main range of observed values from Greenland glaciers (Rignot et al., 2010, Carroll et al., 2016). The vertical pattern of oceanic melt was either set as constant with depth (C) or as linearly increasing from zero at the waterline to the prescribed melt rate at the bottom of the fjord (denoted as L). In the following, the term "melt" in general refers to submarine melt at the calving face.

To set the results of the two-dimensional modeling experiments into the context of the high oceanic melt rates observed in localized meltwater plumes, additional preliminary simulations with a three-dimensional version of the model were undertaken. The specific details of the three-dimensional model setup are described in the supplementary material.

4.3 Results

All model runs start with the along flow rectangular geometry that evolves by ice deformation, calving and melt for 5 years. During the first 1.5 years, the terminus geometries self-adjust from the initial condition, and to the imposed melt rates. Therefore, the evolution of volume loss (with units $\mathrm{m^3/m}$) for all experiments is only shown from 1.5 years onward to the end of the simulation (Fig. 4.1).

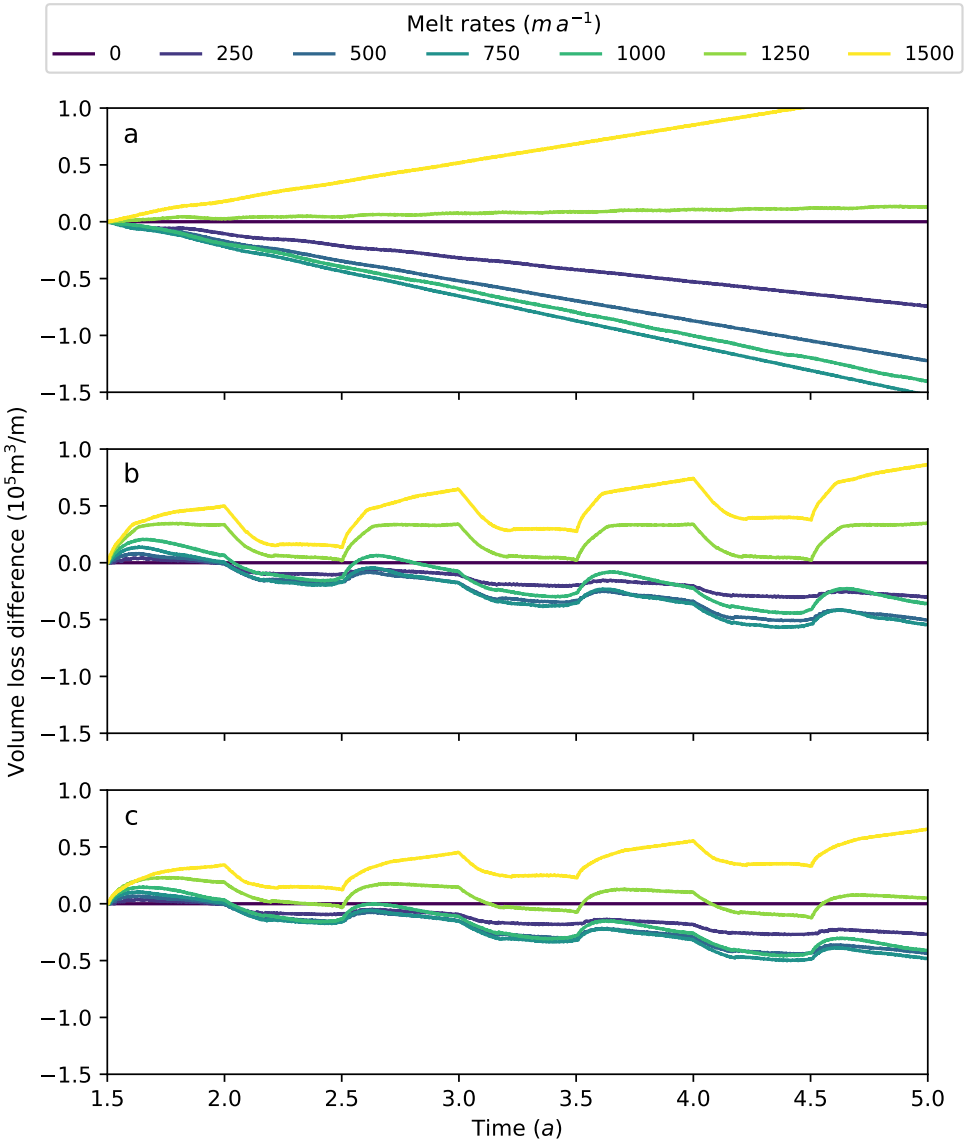

Figure 4.1: Cumulative volume loss difference ($10^5 \mathrm{m}^3/\mathrm{m}$) over time in comparison to the "no melt" scenario $\mathrm{M0}$ for different melt scenarios. (a) CMC: Melt is continuous and constant with depth. (b) SMC: Melt is seasonal and constant with depth. (c) SML: Melt is seasonal and linearly increases with depth (maximum melt rate M at depth and $M = 0$ at the waterline).

In the first set of model experiments, labeled CMC (Tab. S2), a continuous oceanic melt that is constant with depth was applied. The results of this set are shown in Movie S1 and Figures 4.2 and 4.1a.

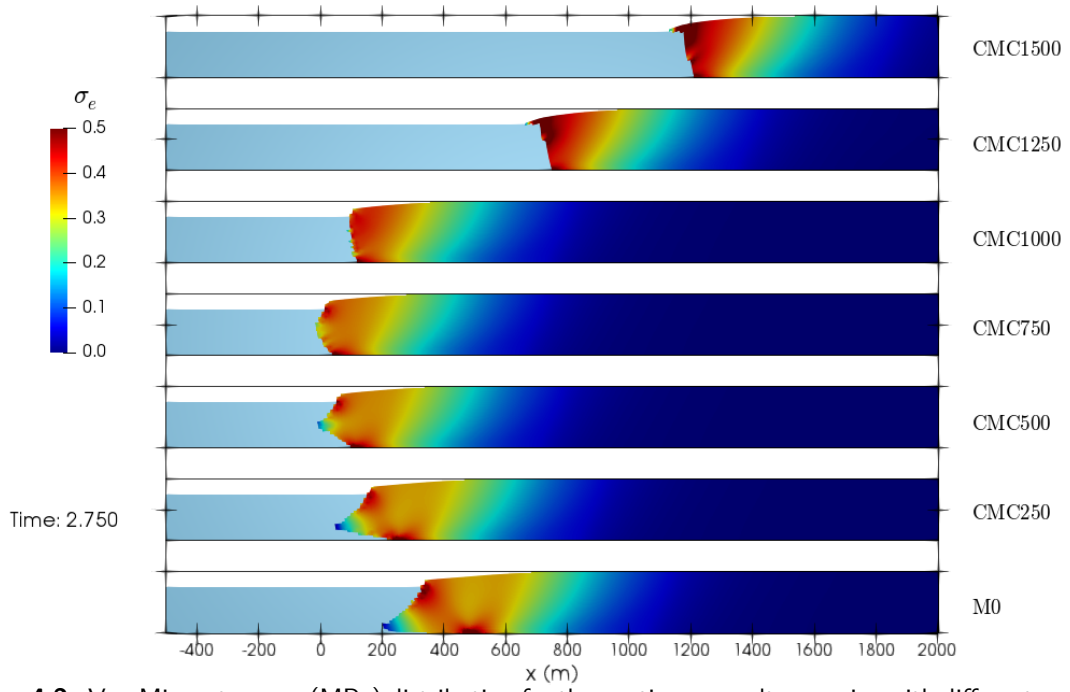

Figure 4.2: Von Mises stress σ_e (MPa) distribution for the continuous melt scenarios with different oceanic melt rates as labeled on the right (numbers after CMC in $\mathrm{m\,a^{-1}}$), after 2.75 years of simulation. Light blue indicates ocean water and dark lines show the bed and maximum thickness for each geometry. Note that the CMC1500 experiment is displayed with $u_{in} = 1000\,\mathrm{m}\,a^{-1}$ like all other experiments (but was run with $u_{in} = 1250\,\mathrm{m}\,a^{-1}$ in order to constrain the domain length).

Different shapes of the calving front (Fig. 4.2) and volume loss rates (relative to the "no melt" scenario M0; Fig. 4.1) are obtained for the imposed melt rates. The scenarios of high oceanic melt ($\mathrm{M} > 750\ \mathrm{m\,a^{-1}}$) show the development of an over-steepened calving face below the water line (Movie S1 and Fig. 4.2) and experience increasing volume losses with enhanced melt rates (Fig. 4.1a). In contrast, lower melt rate scenarios ($\mathrm{M} \leq 750\ \mathrm{m\,a^{-1}}$) result in decreasing volume losses with increasing oceanic melt rates (Fig. 4.1a), and an ice foot below the waterline develops near the base of the fjord that is more prominent for lower melt rates (Movie S1 and Fig. 4.2).

Movie S2 shows the evolution of the glacier geometry that experiences seasonal variations in depth-averaged melt (labeled SMC). For the same melt rates as before, smaller absolute and relative volume loss differences are obtained than for the CMC scenarios (Fig. 4.1 and Fig. 4.3). During the melt season, the volume losses and geometries evolve similarly to the CMC scenarios, with the development of over-steepened calving faces (Fig. S1, between 2.6 and 3 years) and increased volume losses for the SMC1000 high melt scenario (Fig. 4.1b). In this scenario, the damage accumulated in the ice below the waterline remains mostly below the threshold for break-off (Fig. S1 between 2.6 and 3 years), and thus oceanic melt almost directly translates into additional volume loss. After switching off oceanic melt, the volume loss briefly decreases (Fig. S1 between 3 and 3.2 years, Movie S2), and the calving front adjusts to a shape and evolution similar to the "no melt" scenario M0, which exhibits a permanent large ice foot below the waterline. For lower melt rates, the seasonal evolution of

the front is very similar, although the undercutting during the melt phase is less pronounced and volume losses are slightly reduced.

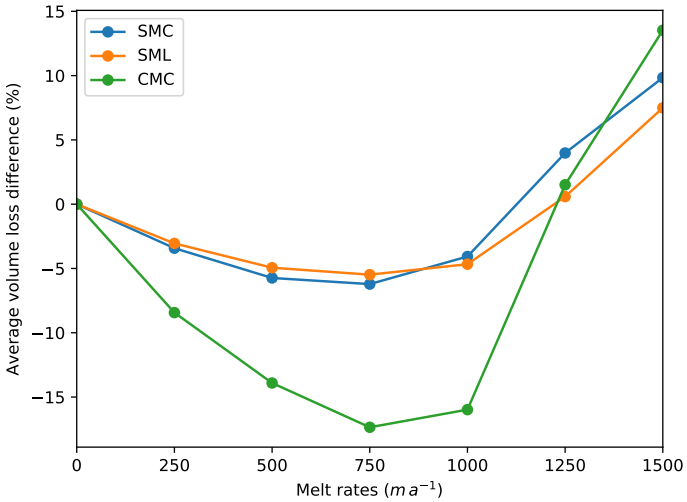

Figure 4.3: Average volume loss difference (%) in comparison to the "no melt" scenario M0 for the different melt scenarios.

Figure 4.3 summarizes the key characteristic of our sensitivity experiments, namely that moderate oceanic melt reduces volume loss rates. Volume losses are higher for the "no melt" scenario M0 than for most scenarios with melt. For our choice of model parameters the minimum average volume loss is obtained for scenario CMC750, which is $\sim$ 17% less than without melt. Only the scenarios with melt rates exceeding 1000 m a^{-1} show a higher volume loss than scenario M0.

Figure 4.1c displays the volume losses over time with seasonal oceanic melt that linearly increases with depth (denoted SML, Tab. S2). Similar geometries (Fig. S2 and Movie S3) and the same relationship between volume loss and oceanic melt are found as for the SMC scenarios. Compared to SMC, the relative differences in volume loss are slightly subdued and a melt rate exceeding 1250 m a^{-1} is necessary for a volume loss that is higher than the "no melt" scenario M0.

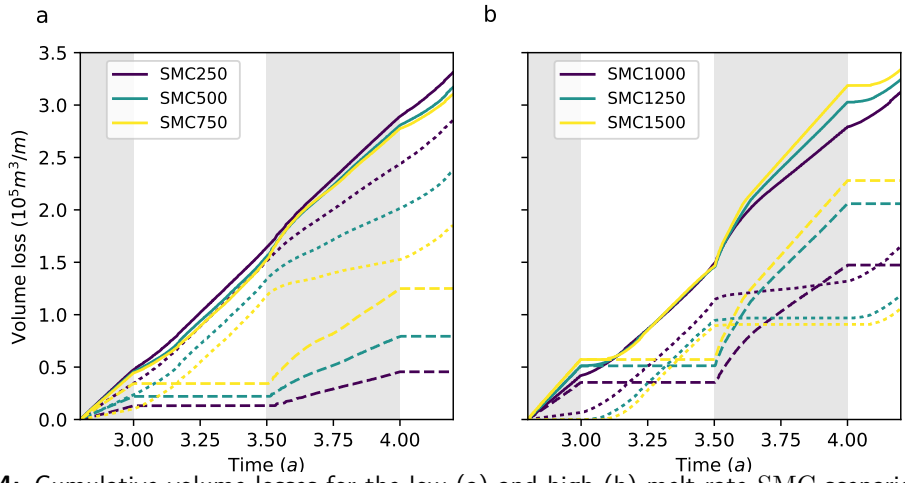

Figure 4.4: Cumulative volume losses for the low (a) and high (b) melt rate SMC scenarios between 2.8 and 4.2 years of simulation time. Different scenarios are represented by different colors. In addition to total volume loss (solid lines), the components of volume losses by calving (dotted lines) and oceanic melt (dashed lines) are displayed. The gray areas show the periods during which melt was applied.

The relative contribution of calving and oceanic melt to volume loss is displayed in Figure 4.4 for the SMC scenarios. For high seasonal melt rates (> 750 m a^{-1}) the volume loss during the melt season is dominated by oceanic melt, with strongly reduced volume losses through damage-induced calving. During the period without melt, damage evolution quickly recovers and calving thereby rapidly reaches a constant rate again. For lower seasonal melt rates, the effect of reduced calving due to melting is also clearly apparent.

4.4 Discussion

4.4.1 The effect of melt on tidewater glacier evolution

Melt-undercutting is generally assumed to lead to higher calving activity due to the formation of an over-steepened calving face below the waterline (Hanson and Hooke, 2000, O'Leary and Christoffersen, 2013, Benn et al., 2017). Our model results show that the effect of oceanic melt on the calving front geometry could lead to a complex behavior of tidewater glacier termini. This complexity seems to stem from the different calving front geometries below the waterline that result from the competing processes of damage evolution and oceanic melt.

For our choice of geometrical and model parameters the lowest volume loss was found for a melt rate of 750 m a^{-1} (Fig. 4.3). At higher melt rates, the volume losses are increasingly dominated by melt, and therefore calving through damage is effectively shut down, as the ice is melted away before critical damage is reached (Fig. 4.4b). At lower melt rates, calving dominates the volume loss (Fig. 4.4a) and the calving front geometry is characterized by a subaqueous ice foot which is most pronounced for the "no melt" scenario M0. Such subaqueous feet are generated when calving loss above the waterline exceeds the volume loss

below (Benn et al., 2007b), and have been observed at several calving glaciers (Warren et al., 1995, Motyka, 1997, Hunter and Powell, 1998, O'Neel et al., 2007, Sugiyama et al., 2019). The presence of an ice foot induces buoyancy forces (Warren et al., 2001, Benn et al., 2007b) and enhances stresses at the calving face and around the grounding line (clearly visible in panels M0 to CMC500 of Fig. 4.2). These stresses in turn lead to increased damages and hence higher volume losses through calving (Fig. 4.4). In contrast, increasing oceanic melt reduces the length of the ice foot faster than it can break off through damage accumulation, thus reducing volume loss rates. These model results demonstrate that moderate melt rates reduce volume loss from the glacier terminus and imply that for low melt rates an increase in fjord temperatures would not necessarily induce enhanced volume loss and terminus retreat.

Large ice feet are not often observed at ocean-terminating tidewater glaciers. While the example of a 100 m long ice terrace in a Patagonian lake demonstrates the stability of large protruding ice feet (Sugiyama et al., 2019), such features, if they are formed, are likely rapidly melted away in tidewater fjords. The sparse observational record from Greenland is restricted to summer conditions, where several ice feet of up to 50 m length have been observed (Rignot et al., 2015, Fried et al., 2015, Slater et al., 2018). The shapes and extents of these documented terminus geometries agree with our model results. For oceanic melt rates typically estimated in Greenland fjords in summer, the modeled ice feet are reduced to 50 m or less (Fig. 4.2 and Movie S2), and the modeled front shapes are consistent with observations (e.g., Kangerlussuup Sermia, Fried et al., 2015). For such moderate melt rates, our model results imply a stabilizing effect on the calving front evolution.

In the case of high melt rates (> 750 m a^{-1}), as expected around meltwater plumes (Sciascia et al., 2013, Fried et al., 2015, Slater et al., 2015, 2018), oceanic melt dominates volume loss (Fig. 4.4b). Melt-undercutting leads to the formation of over-steepened calving faces with large stresses (Fig. 4.2), but calving through damage only occurs above the waterline and hence the loss through calving remains limited. Importantly, the contrasting relationships robustly map onto the two cases of (i) low and distributed oceanic melt rates and (ii) high melt rates from meltwater plumes (Sciascia et al., 2013, Fried et al., 2015, Slater et al., 2015, 2018).

Ultimately, it is the competition between damage evolution and ice removal through oceanic melt that determines the total volume loss, and hence advance or retreat of the terminus. Additional experiments were performed with a doubled damage rate parameter, which showed the same contrasting relationship of oceanic melt with glacier evolution, with a shift of the minimum of average volume loss towards higher values of melt rate (Fig. S3). Under constant melt conditions, an increase in damage rate leads to a larger volume loss through ice break-off and consequently a reduced effect of oceanic melt. The transition from a volume loss reduction to an enhancement due to oceanic melt therefore also depends on the timescale of damage evolution (damage rate parameter).

4.4.2 Localized high melt in three dimensions

Large submarine melt rates are often associated with narrow discharge outlets at the base of the terminus (Fried et al., 2015, Slater et al., 2018). While the runoff input drives the formation of localized plumes that only cover a portion of the terminus extent, fjord-wide circulations likely transport the warm water over most of the calving front (Slater et al., 2018). Our two-dimensional model results do not capture this spatial variability. To qualitatively assess three-dimensional effects of such localized high melt on the evolution of the calving front, we ran a preliminary simulation on an idealized three-dimensional glacier.

We applied a melt rate of $250\,\mathrm{m\,a^{-1}}$ in all submerged parts of a 1500 m wide and 200 m high calving front, representing background oceanic melt rates from entrainment and upwelling of warm fjord water. Substantially higher localized melt rates were assigned over two 50 m wide sections of the terminus (Fig. 4.5), with a constant melt rate of $M = 500\,\mathrm{m\,a^{-1}}$ between 450 and 500 m at the calving front and a second plume between 950 and 1000 m with a $M = 1000\,\mathrm{m\,a^{-1}}$ melt rate. All other parameters remained the same as in the two-dimensional modeling above (see supplementary material for additional details).

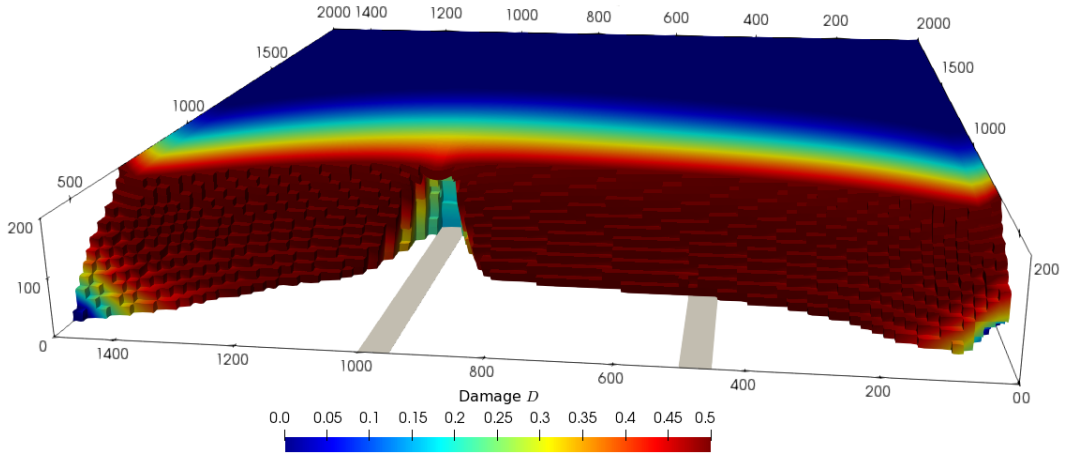

Figure 4.5: Damage D distribution in the three-dimensional model after one year. Grey bands show the locations of high localized oceanic melt rates: $M = 1000\,\mathrm{m\,a^{-1}}$ between 950 and 1000 m and $M = 500\,\mathrm{m\,a^{-1}}$ between 450 and 500 m on the transverse to flow axis, $M = 250\,\mathrm{m\,a^{-1}}$ elsewhere.

Figures 4.5 and S4 show the evolved geometry, damage and von Mises stress distributions after one year of simulation. At the location of the highest plume melt rate ($1000\,\mathrm{m\,a^{-1}}$) a narrow overhang has been eroded with a high stress concentration and strongly negative vertical velocities (Fig. S5). Below this overhang, low damage values are found as the ice was melted away faster than damage can evolve to a critical value. In contrast, the second plume with lower melt rates of $500\ \mathrm{m\,a^{-1}}$ did not produce any overhang and the vertical shape of the front is almost indistinguishable from areas where solely background melt was applied.

The results of the three-dimensional experiment are in agreement with the interpretation from the two-dimensional models, but show the importance of localized high melt rates

in plumes, which cut the front back and thereby enhance retreat. A comparison to an experiment with background melt only shows that the high localized melt seems to slightly enhance front retreat along the entire front (Fig. S6) and its impact is therefore not only local, as observed for tidewater glaciers with shallow ($< 400\mathrm{m}$) grounding lines (Fried et al., 2018).

The modeled ice foot of 70 m and the ∼400 m cutback of the meltwater channel (Fig. 4.5) give an indication of the type of geometry that can be obtained with the assumptions of our model. These emergent geometries are similar to the few observations from Greenland (Fried et al., 2015, Rignot et al., 2015, Slater et al., 2018), although the exact dimensions are different. By simple variations of the melt rate in the plume and along the front, various extents and geometries of the terminus can be produced, and their evolution investigated.

The computational costs of three-dimensional simulations are demanding for the application to real glaciers. However, they allow us to elucidate mechanisms of tidewater glacier evolution that are not captured by flowline models. For example, our three-dimensional modeling implies that increased melt in plumes may not only locally enhance volume loss, but trigger enhanced calving and retreat over the entire front, even if background melt rates remain relatively low. This three-dimensional effect is particularly important as plume melt rates increase with subglacial discharge, which in turn is directly linked to surface melt, and has the intriguing consequence that atmospheric warming increases the frontal volume loss (Straneo and Heimbach, 2013). This sensitivity to surface temperature is independent of any warming of ocean water.

4.4.3 Model simplifications

In this study we aimed at distinguishing the effect of oceanic melt on volume loss alone, without the well-known strong control of bed geometry on tidewater glacier behavior. To use a more realistic geometry than our idealized block, and to validate the results with direct observations, several adaptations would be needed. Sliding of the glacier over the bedrock was implemented as a simple forward movement of the mesh nodes. Alternative implementations of basal motion use a frictional relationship that depends on the water pressure (e.g., Ryser et al., 2014b). However, the sensitivity study of Mercenier et al. (2018) indicated that the effect of basal sliding on the stress regime at the calving front, and therefore the damage evolution, is limited, and the results presented here are robust in this regard.

The submarine melt profiles applied on the calving front were idealized to study a range of forcings. They therefore do not represent the exact melt rate distribution of any particular glacier (Ma and Bassis, 2019). The simple melt parametrizations are however sufficient to examine the effect of oceanic melt on tidewater glacier evolution.

4.5 Conclusions

We showed with detailed model experiments that oceanic melt has a more complex influence on tidewater glacier evolution than is commonly assumed. At high oceanic melt rates,

increased melt rates lead to increased volume losses. In contrast, at low to intermediate melt rates volume losses are almost constant or even decrease with increasing oceanic melt.

The complex interplay between ice fracturing processes and oceanic melt and its effect on the evolution of the calving front geometry is illustrated by our transient modeling results. In the scenarios with low or zero melt, the terminus geometry consists of a submerged ice foot that eventually breaks off due to buoyancy forces. Low to intermediate oceanic melt reduces the size of the ice foot, and consequently buoyancy forces, and thus stabilizes the glacier geometry. Only at very high melt rates the glacier evolution is dominated by the removal of submerged ice with a negative feedback on ice break-off, even with the presence of over-steepened calving faces.

Our model results highlight the necessity to consider iceberg calving and oceanic melt as tightly coupled processes that both influence the terminus geometry, which in turn affects the calving process. Simple parametrizations of calving with oceanic melt or temperatures do not capture the complexity of tidewater glacier evolution and neglect the inverted relationship at low oceanic melt rates. The susceptibility of the terminus to changes in local external forcings from meltwater plumes highlights the need for further investigation of three-dimensional effects. Calibration of model parameters with detailed observations will also be necessary to reproduce the evolution of real tidewater glaciers. This will, together with additional processes, such as the buttressing effect from ice mélange, help to better understand the calving mechanism and its link to the climate system.

Acknowledgments

The authors wish to thank the editor Mathieu Morlighem and two anonymous reviewers for their comments that helped to considerably improve this paper.

The libMesh library is a C++ framework for the numerical simulation of partial differential equations on serial and parallel platforms available at `http://libmesh.github.io/` (Kirk et al., 2006). Data from this study can be obtained from `https://doi.org/10.5281/zenodo.2677937`.

This work was funded by the Swiss National Science Foundation Grant 200021-156098.

The authors declare that they have no conflict of interest.

4.A Appendix

4.A.1 Three-dimensional model implementation

We ran the three-dimensional model on a 2000 m long, 1500 m wide and 200 m thick glacier geometry, and with a relative water level $\omega = 0.75$. A melt rate of $M = 500\,\mathrm{m\,a^{-1}}$ is applied between the widths of 450 and 500 m and between 950 and 1000 m, a $M = 1000\,\mathrm{m\,a^{-1}}$ melt rate is imposed.

The upper surface of the glacier is described as a traction free boundary while the side and upstream boundaries were treated as zero velocity Dirichlet boundaries. At the ice/ocean interface, a normal stress boundary condition was imposed below the waterline, while the surface above water is kept traction-free, similar to (Mercenier et al., 2019; Eq. 6). On the bottom surface boundary of the domain the type of boundary condition depends on the normal stress. For parts of the boundary where the normal stress exceeds the water pressure, a zero velocity Dirichlet boundary condition is imposed. On the remaining parts of the bottom boundary, the ice/ocean normal stress boundary condition is imposed.

In order to reduce the computing time, the influx velocity is set to $0\,\mathrm{m\,a^{-1}}$ and the temporal and spatial resolution are reduced to 0.005 years and 16.67m, respectively.

4.A.2 Model parameters, notations, values and units

Table 4.A.1: Model parameters, notations, values and units.

Parameter	Notation	Value	Units
Fluidity parameter	A	75	$\mathrm{MPa^{-3}\,a^{-1}}$
Damage rate	B	2	$\mathrm{MPa^{-r}a^{-1}}$
Damage threshold	D_{th}	0.5	
Gravitational acceleration	$\boldsymbol{g}$	9.81	$\mathrm{m\,s^{-2}}$
Melt rate	M		$\mathrm{m\,a^{-1}}$
Glen exponent	n	3	
Damage law exponent	r	0.43	
Ice density	ρ_i	917	$\mathrm{kg\,m^{-3}}$
Sea water density	ρ_w	1028	$\mathrm{kg\,m^{-3}}$
Damage threshold stress	σ_{th}	0.11	MPa
Relative water level	ω	0.75	

4.A.3 Summary of the model experiments and their notations

Table 4.A.2: Summary of the model experiments and their notations.

Seasonality	Depth-relation	Melt rate ($\mathrm{m\,a^{-1}}$)	Notation
Continuous	Constant	0	M0
Continuous	Constant	250	CMC250
Continuous	Constant	500	CMC500
Continuous	Constant	750	CMC750
Continuous	Constant	1000	CMC1000
Continuous	Constant	1250	CMC1250
Continuous	Constant	1500	CMC1500
Seasonal	Constant	250	SMC250
Seasonal	Constant	500	SMC500
Seasonal	Constant	750	SMC750
Seasonal	Constant	1000	SMC1000
Seasonal	Constant	1250	SMC1250
Seasonal	Constant	1500	SMC1500
Seasonal	Linear	250	SML250
Seasonal	Linear	500	SML500
Seasonal	Linear	750	SML750
Seasonal	Linear	1000	SML1000
Seasonal	Linear	1250	SML1250
Seasonal	Linear	1500	SML1500

4.A.4 Snapshots of the SMC1000 scenario at different times

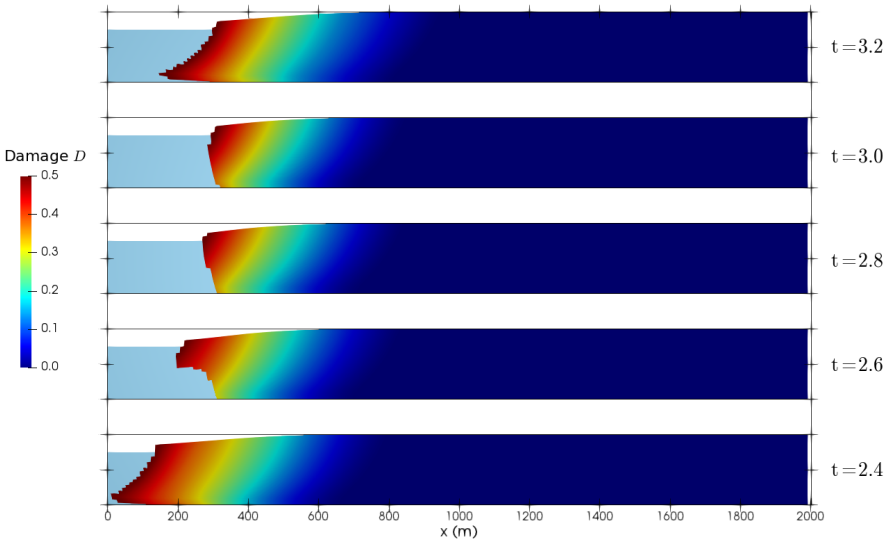

Figure 4.A.1: Snapshots of the SMC1000 scenario at different times, labeled on the right. The melt season occurs between 2.5 and 3 a. Light blue indicates the ocean water and dark lines show the bed and maximum thickness for each geometry.

4.A.5 Average volume loss difference to the M0 scenario for different damage rates

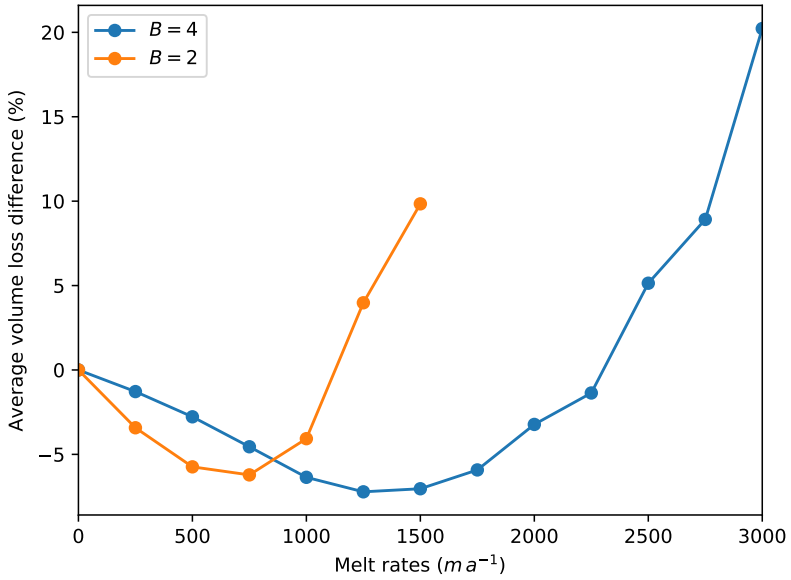

Figure 4.A.2: Average volume loss difference (%) to the M0 scenario at different melt rates for different damage rates ($\mathrm{MPa}^{-r}\mathrm{a}^{-1}$), labeled on the top left. $B = 2$ is the damage rate used for the main experiments of this study.

4.A.6 von Mises stress distribution in the three-dimensional model

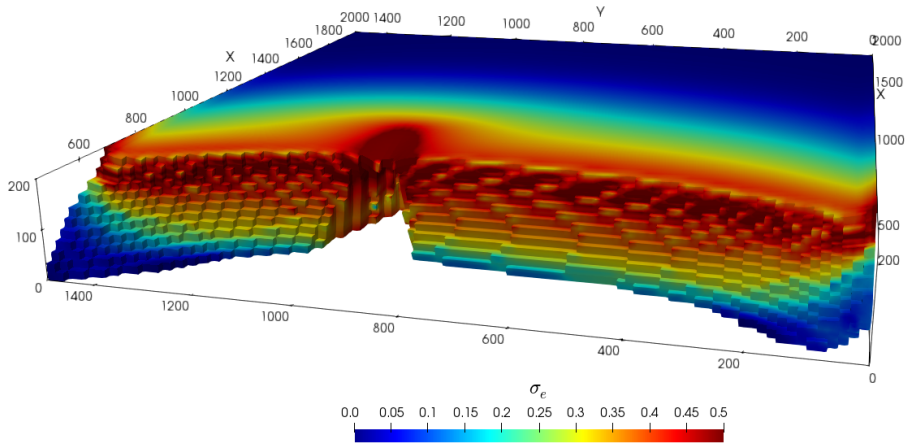

Figure 4.A.3: von Mises stress σ_e (MPa) distribution in the three-dimensional model after one year. $M =$ 1000 m a^{-1} between 950 and 1000 m and $M =$ 500 m a^{-1} between 450 and 500 m on the y-axis, $M =$ 250 m a^{-1} elsewhere.

4.A.7 Vertical velocity in the three-dimensional model experiment

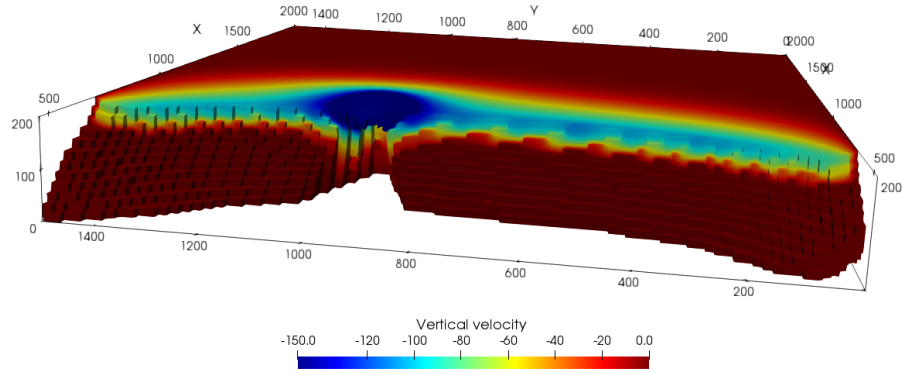

Figure 4.A.4: Vertical velocity component (m a^{-1}) distribution in the three-dimensional model after a year. $M =$ 1000 m a^{-1} between 950 and 1000 m and $M =$ 500 m a^{-1} between 450 and 500 m on the y-axis, $M =$ 250 m a^{-1} elsewhere.

4.A.8 Overlap of three-dimensional with plumes and background melt

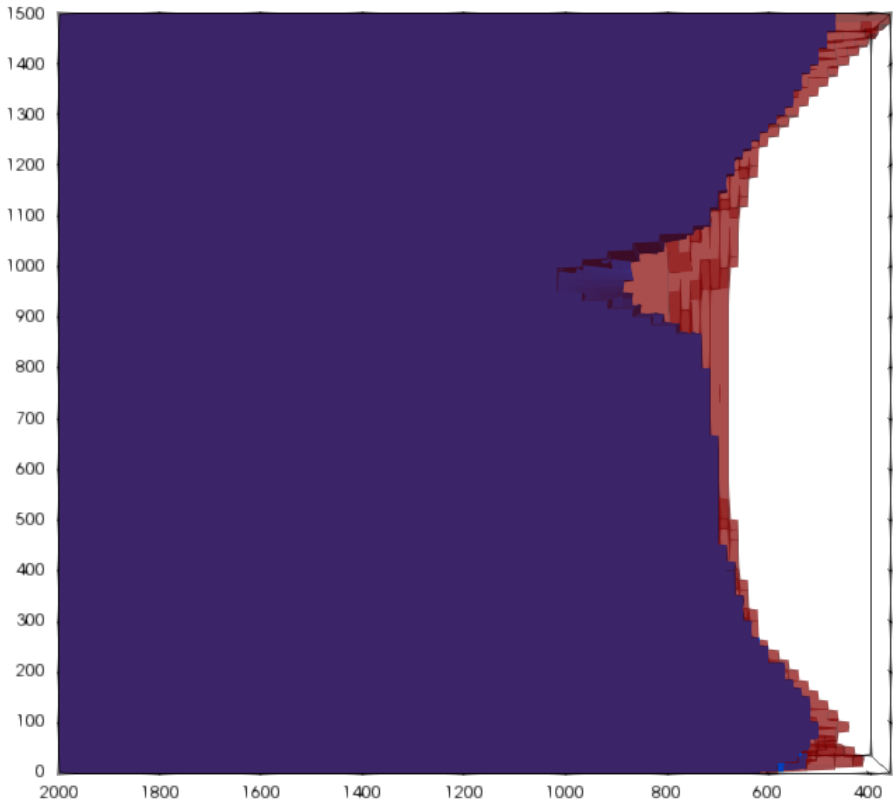

Figure 4.A.5: Overlap, viewed from below, between the three-dimensional model with two melt water plumes (blue) and the three-dimensional model with only background melt (red) after one year of simulation.

5 Additional model experiments

This chapter presents additional investigations performed with the transient calving model developed in the second publication. These experiments are not part of the publications.

5.1 Water density

Calving rates of glaciers terminating in freshwater are consistently found to be one order of magnitude lower than the calving rates for ocean-terminating glaciers in comparable settings (Benn et al., 2007b). This systematic difference in calving rates has been attributed to differences in water density, subaqueous melt rates, frontal over-steepening and longitudinal strain rate (Benn et al., 2007b).

In this experiment, we employ the transient calving model developed in the second publication to compare the volume loss for a glacier that terminates in a freshwater lake, with a water density $\rho = 1000\,\mathrm{kg\,m^{-3}}$, and one that terminates in ocean water, with a water density $\rho = 1028\,\mathrm{kg\,m^{-3}}$. The idealized glacier used for this experiment is 200 m thick with a relative water depth ω = 0.75 and no subaqueous melt is applied (see Table 4.A.1 for other model parameters).

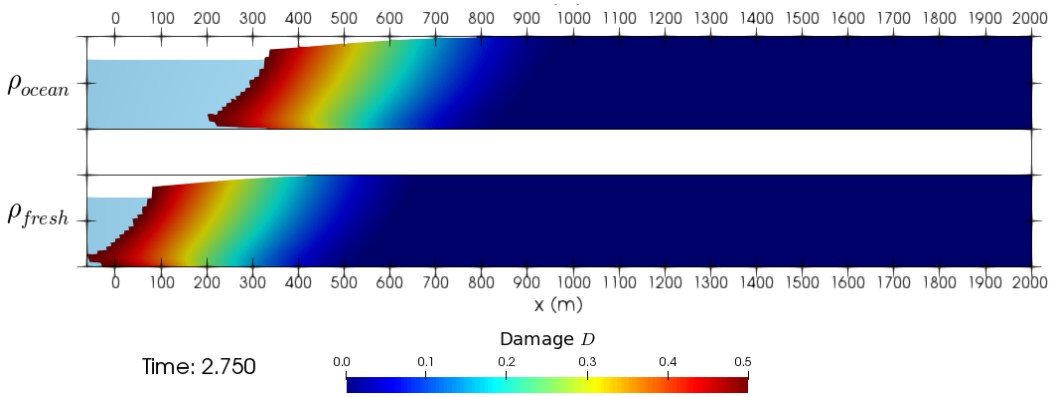

Figure 5.1: Modeled damage distribution for a glacier terminating in freshwater (lower panel) and in tidewater (upper panel), after 2.75 years of simulation. Light blue indicates ocean water and dark lines show the bed and maximum thickness for each geometry.

Figures 5.1 and 5.2 show the terminus geometries and the cumulative volume losses for the glacier with two different water densities, respectively. Figure 5.2 shows the cumulative volume loss from 1.5 years to 5 years of simulation, due to the self-adjustment period of the model to the initial geometry. The density of the water at the frontal boundary of the glacier does not appear to show a substantial impact on the calving front geometry, but higher volume losses are found for the marine-terminating glacier. The difference in total volume loss between tidewater and freshwater is ~ 10 %. The water density difference alone cannot explain the order of magnitude difference in calving rate between freshwater and tidewater glaciers.

The two modeled geometries (Fig. 5.1) are characterized by a large ice foot below the waterline. Buoyant forces, due to the presence of the ice foot, induce an upward rotation of the terminus, which leads to increased stresses and calving activity. A higher water density leads to stronger buoyancy forces, which consequently could explain the difference in volume losses between the two water densities.

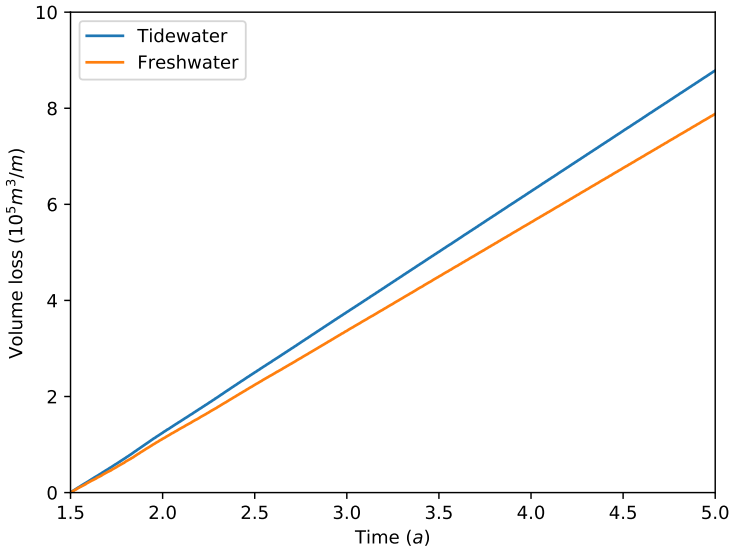

Figure 5.2: Modeled cumulative volume losses ($10^5 \mathrm{m}^3/\mathrm{m}$) for a glacier terminating in freshwater and in tidewater.

5.2 Tides

A process that was not considered in the publications employing the transient calving model is the potential fatigue of the glacier ice due to repeated variations in water depth through tidal fluctuations. For example, a synchronicity between ice flow velocities and tidal activity, which would potentially impact the calving activity, has been observed at Store Gletscher (Walter et al., 2012). In order to investigate the sensitivity of the volume loss of a tidewater

glacier to tidal forcing, the water depth H_w at the calving front was defined as a function of time t

$$H_w = H_{wi} + H_T \sin(2\pi f t) \tag{5.1}$$

with $H_{wi} = 150\,\mathrm{m}$ the initial water depth, $H_T = 1.5\,\mathrm{m}$ the amplitude of the tides and $f = 2 \cdot 365\,\mathrm{a}^{-1}$ the tide frequency, representing 2 tidal cycles per day of simulation. We perform an experiment with the same model parameters as in the previous section for an idealized tidewater glacier.

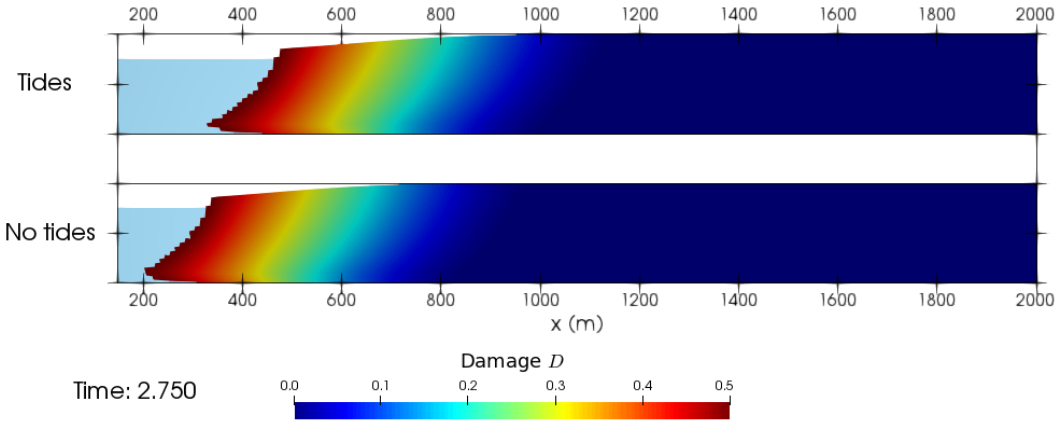

Figure 5.3: Modeled damage distribution with (upper panel) and without (lower panel) the effect of tides, after 2.75 years of simulation. Light blue indicates ocean water and dark lines show the bed and maximum thickness for each geometry.

Similarly to the water density experiment, tidal fluctuations have a limited effect on the calving front geometry (Fig. 5.3) and the volume loss of the tidewater glacier, which is ~ 5 % larger when tidal fluctuations are included in the simulations. Tidal fluctuations further affect the periodicity of the volume loss, with a shift towards higher frequencies (Fig. 5.4). The periodicity of the tides cannot be observed in the volume loss signal due to the time step size and number in the simulation.

A larger amplitude of the tidal variation would likely have a greater impact on the volume loss. However, the 1.5 m tide amplitude used for this experiment is already larger than the observed ~ 1 m amplitude at Store Gletscher (Walter et al., 2012).

5.3 Conclusions

Varying the water density and including variations of water depth led to a limited effect on the calving front geometry evolution and volume loss. Therefore, combining the effects of water density and tidal fluctuations using the current version of the transient calving model would not be sufficient to explain the one order of magnitude difference between tidewater and freshwater glaciers.

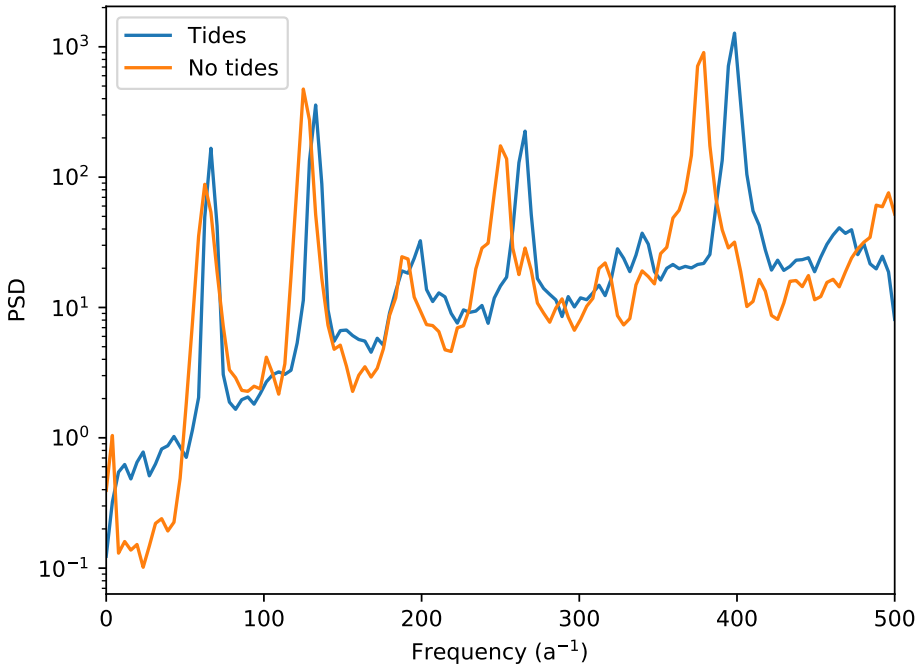

Figure 5.4: Power spectrum density (PSD) distribution of the volume losses for an idealized tidewater glacier with and without tidal fluctuations.

The water density might still explain the one order of magnitude difference between freshwater and tidewater calving rates, due to the dependency of the effective basal pressure (i.e., the difference between ice overburden and hydrostatic pressure) on water density (Van der Veen, 2002). The effective basal pressure determines the sliding velocity of the glacier, which is increased for tidewater glaciers as sea water is denser than fresh water. Larger velocities lead to increased along-flow stretching and facilitate upward propagation of bottom crevasses, and consequently enhance the calving activity (Van der Veen, 2002). This relation could potentially explain the one order of magnitude difference in calving rate between freshwater and tidewater glaciers. While spatially-uniform variations in bed slipperiness were shown to have a limited effect on the stress regime at the calving front in the first publication, the effective pressure typically decreases towards the calving front and may cause additional sliding and potentially impact the calving activity. Therefore, the effect of water density on the effective basal pressure cannot be investigated in the current implementation of the model, due to the simple basal sliding law used. Implementing basal sliding as a frictional relationship that depends on the effective basal pressure might allow the model to reproduce the difference in calving rates from freshwater and tidewater glaciers. Further, the smaller buoyancy difference between

6 Synthesis

The previous Chapters addressed the research questions formulated in Chapter 1 (p. 8). In the following Chapter, the main findings regarding these three research questions are discussed.

6.1 How do geometrical properties of the calving front influence the stress and flow regimes of tidewater glaciers?

In order to provide an answer to this research question, the sensitivity of an idealized glacier to variations in calving front slope, relative water depth and basal sliding was investigated. The magnitude of stresses and velocities near the grounded vertical calving fronts shows a dominant dependence on the relative water depth. As the relative water depth increases, flow velocities and stresses decrease. Therefore, the presence of water at the terminus of a tidewater glacier is shown to have a strong stabilizing effect (as emphasized by Bassis and Walker, 2012), which seems in contrast with commonly-used relations that predict increasing calving rates with water depth (Brown et al., 1982, Meier and Post, 1987, Hanson and Hooke, 2000). However, in nature, glaciers terminating in deeper waters are also generally thicker and therefore calve at higher rates as they experience higher stresses. Glaciers with grounded termini that are characterized by reclining calving faces have the potential to be more stable than those with vertical fronts. Such glaciers can sustain larger heights than the estimated 110 m maximum height for a dry calving front of a grounded glacier (Bassis and Walker, 2012), as observed in the case of Eqip Sermia with a 150-200 m high calving face with an inclination of 45 °(Lüthi et al., 2016). Spatially uniform variations in basal sliding have a limited effect on the stability of the calving front, as the magnitude and location of the stress maximum shows a small sensitivity to variations in bed slipperiness.

The similarity in stress distribution at the surface of the grounded idealized glaciers for varying relative water depths allows for an explicit parametrization of the stresses. With some simple assumptions on a damage evolution law, a calving rate relation can be derived that only requires two geometrical properties: relative water depth and frontal ice thickness. The semi-empirical relation is similar to calving front position models (Vieli et al., 2001, Benn et al., 2007a, Nick et al., 2010, Todd and Christoffersen, 2014, Benn et al., 2017, Todd et al., 2018), as it is based on the stress distribution near the calving front. The calving rate parametrization is calibrated using data on calving rate, ice thickness and relative

water depth for a wide variety of tidewater glaciers in the Arctic. This parametrization is straightforward and could therefore easily be applied in large-scale ice-sheet models. This parametrization could further be used to assess the stability of tidewater glaciers with different fjord geometries for paleo-reconstructions of ice sheet behavior (Vieli et al., 2019).

In the model results of the last research publication, the geometrical properties induced by oceanic melt at the calving front further show a strong influence on the stress and flow regime and a more complex than previously assumed relationship between oceanic melt and volume loss is found (O'Leary and Christoffersen, 2013, Motyka et al., 2013). An interesting feature that appears when oceanic melt rates are low in the transient calving model is the development of a subaqueous ice foot. A large ice foot below the waterline increases the stresses and causes a higher rate of volume loss. On the other hand, the calving front face is over-steepened when high melt rates are imposed, leading to high stresses. This effect is particularly visible in the three-dimensional experiment (Fig. 4.A.3), in which a large stress concentration is found in the direct vicinity of the over-steepened part of the calving front.

6.2 How realistically can a model that couples ice flow and damage mechanics reproduce calving front geometry and tidewater glacier evolution?

The evolution of the calving front is essentially controlled by four processes that depend on each other, but act at different time scales: ice deformation, damage evolution, oceanic melt and basal sliding. These processes are incorporated in the model, and have been used to investigate their importance, their time scales and their intricate coupling. While oceanic melt and basal sliding, in this thesis, are external forcings on the glacier, damage evolves at its own time scale, driven by the stress regime, which depends on the calving front geometry. The model results of this thesis show that the calving front shapes obtained by varying damage parameters are similar but the rates of advance and retreat differ. These parameters therefore determine the time scales at which break-off occurs rather than the shape of the calving front. Damage evolution parameters are not well constrained and need calibration with real world observations. Calving rate measurements for different glaciers with various geometries could be used to better estimate the damage rate parameter.

The most important parameter for the glacier evolution is the choice of stress measure for damage evolution. While modeling experiments with all stress measures reproduce a vertical cliff above the waterline, as commonly observed for calving glaciers (Benn et al., 2007b), larger differences are found for the modeled geometries below the waterline.

The von Mises stress measures exhibit, besides a vertical front above the waterline, a remarkable feature in all model runs: the presence of an ice foot below the waterline. The development of subaqueous ice feet has been observed at several tidewater and freshwater glaciers (Warren et al., 1995, Motyka, 1997, Hunter and Powell, 1998, O'Neel et al., 2007, Sugiyama et al., 2019), and can occur when the losses above the waterline exceed those below

(Benn et al., 2007b). Multibeam bathymetry measurements of marine-terminating glaciers in West Greenland revealed undercut ice faces below the waterline as well as ice foot formations (Fried et al., 2015, Rignot et al., 2015). The glacier undercuts were found to be larger at the sites of subglacial water discharge. Buoyant plumes of subglacial water transport the warm oceanic water to the ice face, and consequently enhance the melt rate (Rignot et al., 2015). The persistent presence of an ice foot at the calving front can be explained by calving through damage evolution together with a potential lack of undercutting by melt, as explained in the following research question discussion.

For the Hayhurst and the maximum principal stress measures, damage is concentrated at the top surface rather than at the bed of the glacier. Thus, cracks do not penetrate through the whole ice thickness of the grounded glacier. The lack of depth penetration is likely due to the importance of the overburden ice pressure at the bed which compensates the tensile and shearing stress components. The no-slip basal boundary condition could further explain the lack of depth penetration, as free slip boundary conditions led to full-thickness crevassing using the maximum principal stress (Ma et al., 2017). Additionally accounting for the effect of water pressure in the submerged parts of the glacier, i.e., using the effective principal stress as stress measure, led to the formation of a floating ice tongue but cracks at the surface and the bed were still not able to penetrate through the whole thickness of the glacier. The presence of surface water would be likely to facilitate crevasse propagation through the whole thickness of the glacier (Benn et al., 2007b). Including the effect of such a process into the model with these stress measures might be effective in reproducing ice shelf disintegration.

Based on these considerations, the von Mises stress measures produce the most realistic calving front geometry evolutions for tidewater glaciers using a damage mechanics approach. Interestingly, Choi et al. (2018) found that the von Mises tensile stress provides more satisfactory results than other stress measures in their effort to compare different calving laws. The experiments with the von Mises stress measures were, however, not able to produce floating ice tongues. The lack of such features might be due to the glacier thickness imposed (up to 250 m), since thicker glaciers (> 500 m) would be more likely to form floating ice tongues than the thinner glaciers simulated in this thesis.

With respect to current calving models, the transient model developed by Todd et al. (2018) is the most similar model to the transient calving model developed for this thesis. The former model simulates a three-dimensional glacier over several years but is restricted by the use of a rediscretization scheme and the automatic removal of ice feet, which is not consistent with observations (Warren et al., 1995, Motyka, 1997, Hunter and Powell, 1998, O'Neel et al., 2007, Sugiyama et al., 2019). On the other hand, the coupled ice flow/damage model is characterized by a freely evolving calving front geometry of a tidewater glacier. The presence of ice feet was further shown to have a particularly important effect on the calving activity in the oceanic melt sensitivity analysis. Moreover, the coupled two-dimensional ice flow/damage model was also extended to three-dimensions.

In conclusion, the transient calving model developed in this thesis, that couples an ice flow model to a damage mechanics model, is capable of producing the different frontal geometries and calving styles typically encountered in tidewater glaciers.

6.3 How does oceanic melt control the evolution of tidewater glaciers?

Oceanic melt is generally assumed to lead to increased calving activity, thus glacier retreat, through the formation of an over-steepened calving face below the waterline (Hanson and Hooke, 2000, Benn et al., 2017). In a recent sophisticated modeling study, Todd et al. (2018) demonstrated a direct influence of submarine melt on the evolution of Store Glacier, but disregarded the potential effect of buoyant submerged ice (as explained in the previous section). A limited effect of submarine melt has been found in other studies (Cook et al., 2014, Krug et al., 2015). Ma and Bassis (2019) further investigated the controversial effect of submarine melt on the onset of a calving event, starting from an idealized glacier geometry. They found that oceanic melt can have both a suppressing and enhancing effect on iceberg calving. This last study however presents a major limitation since it does not simulate the tidewater glacier evolution after the onset of the first calving event.

The transient calving model developed in Chapter 3 was employed to determine the effect of oceanic melt on iceberg calving and tidewater glacier evolution during several years. The detailed model experiments show that oceanic melt has a more complex relationship with tidewater glacier evolution than previously expected. Similar to the recent modeling effort of Ma and Bassis (2019), submarine melt may have an enhancing or a suppressing effect on calving, depending on the magnitude and vertical profile of melt. Complex relationships between melt and ice dynamics have been modeled in other studies. For example, increasing rates of melting below ice shelves do not necessarily lead to loss of inland ice, but may lead to inland ice thickening and grounding line advance due to the feedback between melting and buttressing forces (Gagliardini et al., 2010). In the results of our modeling experiments, intermediate melt rates ($< 1000\,\mathrm{m\,a^{-1}}$) lead to a lower volume loss than without oceanic melt, while the volume loss increases and the glacier retreats rapidly for very high melt rates. These results are in contrast to the calving parametrizations used in glacier models (Morlighem et al., 2016, Amundson and Carroll, 2018) that only add the contributions of calving and oceanic melt for the evolution of tidewater glaciers.

There is a complex interplay between oceanic melt and iceberg calving that impacts the evolution of the calving front geometry. In the absence of melt, the terminus of the glacier is characterized by a substantial ice foot below the waterline, that continuously breaks off due to buoyant forces. The size of the ice foot is reduced by oceanic melt, causing a reduction of buoyant forces and consequently leads to lower rates of volume loss at the terminus. For high melt rates, oceanic melt dominates the volume loss and evolution of the terminus geometry, with a negative feedback on ice break-off, even with the presence of over-steepened calving faces.

The transition from a volume loss reduction to an enhancement due to oceanic melt ultimately depends on the timescale of damage evolution, as the minimum of average volume loss is shifted towards higher values of oceanic melt with a higher rate of damage evolution. This further highlights the need for a calibration of the damage rate parameter to better understand the effect of oceanic melt on tidewater glacier evolution.

The modeling shows that for low background melt rates, an increase of fjord temperatures would not necessarily lead to a significant increase in volume loss and terminus retreat. Buoyant plumes at the terminus of tidewater glaciers, where high oceanic melt rates have been estimated, would be strengthened by an increase in atmospheric temperatures, as the release of fresh water from surface melting at the base of the glacier would be amplified (Straneo and Heimbach, 2013). Increases in melt rates in buoyant plumes would consequently induce a substantially stronger volume loss and increased glacier retreat. As buoyant plumes only cover a portion of the terminus extent, the two-dimensional model results do not capture the transport of warm water over most of the calving front due to fjord circulation (Slater et al., 2018). A three-dimensional experiment was performed to assess the effect of localized plumes on the evolution of the calving front.

The three-dimensional experiment results are in agrement with the conclusions drawn from the two-dimensional sensitivity analyses, but highlight the importance of localized high melt rates in plumes. High melt rates in plumes cut back the terminus and enhance retreat compared to an overall background melt rate scenario. The three dimensional terminus geometry that emerges from the model corresponds well to the few observed tidewater glacier geometries, where the front is over-steepened at the location of high localized melt, and the remaining parts of the front are characterized by the presence of ice feet (Fried et al., 2015, Rignot et al., 2015, Slater et al., 2018). This experiment further indicates that increased melt rates in plumes lead to slightly enhanced calving and retreat over the entire front, even with relatively low background melt rates. This outcome is similar to the "keystone effect" modeled by Todd et al. (2018), through which highly localized melt amplifies the rate of mass loss across wide parts of the terminus. This particular three-dimensional effect is particularly important as oceanic melt is expected to increase as a result of atmospheric warming (Straneo and Heimbach, 2013), independently of any ocean water warming. Therefore, atmospheric warming may be the main driver of future tidewater glacier retreat, with a larger impact than oceanic warming.

The submarine melt rate profiles applied on the calving front were idealized to study the effect of increasing forcings. They therefore do not correspond to the exact melt rate distribution of any particular glacier (Ma and Bassis, 2019). Applying various vertical melt profiles did not result in substantial differences in tidewater glacier evolution. The simple melt profiles are therefore sufficient to examine the effect of oceanic melt. A more accurate description of the interaction between oceanic melt and tidewater glacier evolution could be achieved by combining the calving model with an ocean model that simulates the fjord circulation and plume dynamics (e.g., Slater et al., 2018).

It is therefore necessary to consider iceberg calving and oceanic melt as coupled processes that both alter the calving front geometry, which affects the stress regime and generally the calving process. The complexity of the tidewater glacier evolution cannot be captured by simple additive parametrizations of calving and oceanic melt, and three dimensional effects need to be considered for the simulation of tidewater glacier evolution.

7 Conclusions and Outlook

In this Chapter, the conclusions of this thesis are presented and directions for future research on the iceberg calving mechanism are proposed.

7.1 General conclusions

This thesis presented here the development of numerical models that combine ice flow and damage mechanics. The sensitivity of these tidewater glacier models to various geometrical and physical parameters was examined in detail in order to better understand the iceberg calving mechanism.

The relative water depth, together with the frontal ice thickness, was shown to be one of the main determining properties that control the stability of the grounded tidewater glaciers. Based on this consideration, a calving rate parametrization was derived that only depends on frontal ice thickness and relative water depth, and was calibrated with observations from a set of Arctic tidewater glaciers. The application of the calving rate parametrization in large-scale ice sheet models would be straightforward. Further sensitivity analyses interestingly showed a limited effect of basal motion on the stress regime, which allowed for the use of simplified sliding laws in the subsequent model experiments.

A transient model that couples ice flow to damage evolution was developed and was capable of producing the frontal geometries and calving styles typically encountered in tidewater glaciers. Calving front geometries were emergent results of the developed model with a freely evolving terminus boundary, a feature that is important but not common among existing calving models. The sensitivity analyzes suggest that the von Mises stress measures produce the most realistic tidewater glacier front geometry evolutions.

The necessity of incorporating the physical processes (e.g., ice deformation, iceberg calving, oceanic melt, basal sliding) affecting tidewater glacier evolution in numerical modeling efforts was further illustrated by the investigation of the relationship between oceanic melt and iceberg calving. The presence of subaqueous ice feet, that induce an upward rotation of the terminus and therefore increased stresses and volume losses, was persistent in the scenario without oceanic melt. Incorporating oceanic melt into the model led to a reduction of the ice feet extent and consequently lower volume losses at low melt rates. High melt rates

triggered the formation of over-steepened calving faces below water, but ice break-off was effectively shut down as oceanic melt dominated volume loss and removed ice faster than damage had time to evolve to critical damage. Warmer atmospheric temperatures would impact the melt rates in buoyant plumes at the terminus through increased subglacial discharge, which in turn would strongly affect the volume loss and hence retreat of the tidewater glacier. On the other hand, increased oceanic temperatures in the fjord may have a limited effect on the volume loss of tidewater glaciers.

In conclusion, this thesis provides new tools to better understand the iceberg calving mechanism and the related physical processes. The results of this thesis further highlight the importance of the calving front geometrical properties on the evolution of tidewater glaciers.

7.2 Outlook

A number of challenges and questions for future research arose from the undertakings of this thesis. Improvements to the newly developed calving model remain and potential future research directions are proposed in the following sections.

7.2.1 Model improvements

The models used in this thesis could be further improved by overcoming some limitations such as the use of idealized bedrock geometries and simplistic basal sliding laws.

For example, in order to validate the results presented with observations from tidewater glaciers, the evolution of the glacier would have to be simulated over arbitrary bedrock geometries. Several adaptations to the model would have to be implemented such as sliding over an irregular bed geometry.

In the first publication, basal sliding was implemented using a spatially uniform bed slipperiness distribution. In the transient calving model, basal motion was implemented as a simple forward movement of the nodes of the mesh. However, the effective pressure, i.e., the difference between the ice normal stress at the bed and water pressure, typically decreases towards the calving front for real glaciers with sloping surfaces. This may cause additional sliding towards the front, an effect that was not considered in the modeling efforts of this thesis. In further developments of the model, basal sliding should therefore be implemented using a frictional relationship that depends on the effective pressure (e.g., Ryser et al., 2014a). This was further emphasized by the recent study of Stearns and van der Veen (2018) which showed that there is a strong relationship between sliding velocity and effective basal pressure, but not with the frictional stress at the glacier bed.

Implementing oceanic melt at the calving front in a Lagrangian reference frame without a rediscretization scheme presented further challenges. The melting formulation used in this thesis was simple and its implementation straightforward. However, this method neglects

certain effects caused by submarine melting. For instance, small geometrical changes of the calving front due to continuous melt are neglected until the elements at the water boundary are removed. Conversely, a more accurate description of melt would first lead to a reduction of the size of the elements in contact with water before they are removed. This leads to a potential underestimation of melt with respect to the imposed melt rate. Further, the effect of progressive geometrical changes on the stress state, during the melt accumulation process, at the calving front is also partially neglected. During model development, a potential improvement to the simple method used in the second research publication was implemented, but ultimately discarded. By moving the nodes in contact with the water according to the imposed melt at each time step, the size reduction of the elements in contact with water was accurately tracked. However, this approach presented some implementation issues, discussed in Section 3.3.5.

Further potential improvements in the implementation of the model are possible to reduce its large computational time. Minimizing computational time is particularly necessary for three dimensional model experiments, which may take several weeks to compute. Adaptive mesh refinement is a method that subdivides elements to locally refine the mesh (Kirk et al., 2006). This would potentially strongly reduce the computational time as the high spatial resolution of the mesh is only necessary in the vicinity of the calving front. While the ice flow model can easily be computed on an adaptively refined mesh, combining adaptive mesh refinement with the removal of elements proves to be a challenge. Adaptations to the mesh refinement code would be necessary to use the full capacities of the libMesh library.

7.2.2 Future research directions

This thesis explored the effect of geometrical properties on the stress regime and tidewater glacier evolution. The sensitivity of the tidewater glacier evolution to variations in ice thickness was analyzed, but with frontal ice thicknesses always below 250 m. However, ice thicknesses of ocean-terminating glaciers such as Jakobshavn Isbrae or Helheim glacier are estimated to be more than 700 m (Nick et al., 2009, Lüthi et al., 2009, Morlighem et al., 2017). While the coupled ice flow/damage model was not able to produce floating ice tongues for the von Mises stress measures, such features would be more likely to occur for the thicker glaciers (> 500 m) terminating in deeper waters. Investigating the influence of such ice thicknesses with variable water depths on the calving front geometry evolution would provide more insight into the behavior of the larger tidewater glaciers, and would potentially allow the transient calving model to produce features such as floating ice tongues and ice shelves.

This thesis, in the last research publication, focused on the effect of one physical process on the iceberg calving mechanism: oceanic melt. The effects of water density and tidal fluctuations were further examined, but demonstrated a limited influence on the volume loss and calving front geometries. Other physical processes linked to the calving mechanism should be investigated such as the presence of "ice mélange" in the fjord (Krug et al., 2015, Cassotto et al., 2015, Todd et al., 2018) and water-filled crevasses at the surface of the glacier (Weertman, 1973, Duddu et al., 2013). The calving parametrization proposed in the

first research publication could be further improved by incorporating these physical processes, once their link to the calving mechanism are further understood. The validity of the parametrization could be tested by applying it for a different set of tidewater glaciers. Further, the parametrization could be used to assess the stability of tidewater glaciers for reconstructions of the long-term behavior of ice sheets (Vieli et al., 2019).

The oceanic melt profiles used in this thesis were idealized to study a range of forcings. They therefore do not correspond to the exact melt rate profile of any particular glacier. A better representation of subaqueous melting could be achieved by coupling the calving model to an ocean model that simulates the fjord circulation and plume dynamics (e.g., Slater et al., 2018). This coupling would provide a more accurate description of the interaction between submarine melt and iceberg calving.

The damage evolution parameters, which determine the rate of volume loss of the simulated tidewater glaciers, are not yet constrained in the presented results. Damage evolution rates have been determined with data from laboratory tests of creep to failure at constant load under uniaxial tension (Mahrenholtz and Wu, 1992, Pralong and Funk, 2005), but not from glacier ice in natural conditions. Calibration of the transient calving model parameters with detailed observations of the external forcings and calving activity will be necessary in order to reproduce the past and future evolution of real tidewater glaciers. In particular, a strong knowledge of the calving rates and of the three-dimensional glacier geometry would be ideal for parameter calibration. The unique century-long record of Eqip Sermia glacier in West Greenland, which includes time series of atmospheric and oceanic forcing and detailed observations of its terminus geometry (Lüthi et al., 2016), provides the opportunity for calibration of the model parameters that could be followed by a long-term assessment of the performance of the calving model.

References

Åström, J. A., Riikilä, T. I., Tallinen, T., Zwinger, T., Benn, D., Moore, J. C., and Timonen, J.: A particle based simulation model for glacier dynamics, The Cryosphere, 7, 1591–1602, doi: 10.5194/tc-7-1591-2013, 2013.

Albrecht, T. and Levermann, A.: Fracture-induced softening for large-scale ice dynamics, The Cryosphere, 8, 587–605, doi: 10.5194/tc-8-587-2014, 2014.

Amundson, J., Fahnestock, M., Truffer, M., Brown, J., Lüthi, M., and Motyka, R.: Ice mélange dynamics and implications for terminus stability, Jakobshavn Isbræ, Greenland, J. Geophys. Res, 115, F01 005, doi: 10.1029/2009JF001405, 2010.

Amundson, J. M. and Carroll, D.: Effect of Topography on Subglacial Discharge and Submarine Melting During Tidewater Glacier Retreat, Journal of Geophysical Research: Earth Surface, doi: 10.1002/2017JF004376, 2018.

Balay, S., Buschelman, K., Eijkhout, V., Gropp, W. D., Kaushik, D., Knepley, M. G., McInnes, L. C., Smith, B. F., and Zhang, H.: PETSc Users Manual, Tech. Rep. ANL-95/11 - Revision 3.0.0, Argonne National Laboratory, URL `http://www.mcs.anl.gov/petsc`, 2017.

Bassis, J. N. and Jacobs, S.: Diverse calving patterns linked to glacier geometry, Nature Geoscience, 8, 833–836, doi: 10.1038/NGEO1887, 2013.

Bassis, J. N. and Walker, C. C.: Upper and lower limits on the stability of calving glaciers from the yield strength envelope of ice, Proceedings of the Royal Society of London A: Mathematical, Physical and Engineering Sciences, 468, 913–931, doi: 10.1098/rspa.2011.0422, 2012.

Benn, D. I. and Åström, J.: Calving glaciers and ice shelves, Advances in Physics: X, 3, doi: 10.1080/23746149.2018.1513819, 2018.

Benn, D. I., Hulton, N. R., and Mottram, R. H.: 'Calving laws', 'sliding laws' and the stability of tidewater glaciers, Annals of Glaciology, 46, 123–130, doi: 10.3189/172756407782871161, 2007a.

Benn, D. I., Warren, C. R., and Mottram, R. H.: Calving processes and the dynamics of calving glaciers, Earth-Science Reviews, 82, 143–179, doi: 10.1016/j.earscirev.2007.02.002, 2007b.

Benn, D. I., Åström, J., Todd, J., Nick, F. M., Hulton, N. R., and Luckman, A.: Melt-undercutting and buoyancy-driven calving from tidewater glaciers: new insights from

discrete element and continuum model simulations, Journal of Glaciology, 63, 691–702, doi: 10.1017/jog.2017.41, 2017.

Bondzio, J., Seroussi, H., Morlighem, M., Kleiner, T., Rückamp, M., Humbert, A., and Larour, E.: Modelling calving front dynamics using a level-set method: application to Jakobshavn Isbrae, West Greenland, The Cryosphere, 10, 497–510, doi: 10.5194/tc_10_497_2016, 2016.

Borstad, C. P., Khazendar, A., Larour, E., Morlighem, M., Rignot, E., Schodlok, M. P., and Seroussi, H.: A damage mechanics assessment of the Larsen B ice shelf prior to collapse: Toward a physically-based calving law, Geophysical Research Letters, 39, L18 502, doi: 10.1029/2012GL053317, 2012.

Brown, C. S., Meier, M. F., and Post, A.: Calving speed of Alaska tidewater glaciers, with application to Columbia glacier, Tech. rep., US Geological survey professional paper 1258-C, 1982.

Carbonnell, M. and Bauer, A.: Exploitation des couvertures photographiques aériennes répétées du front des glaciers vêlants dans Disko Bugt et Umanak Fjord, Juin-Juillet 1964, Tech. Rep. 3, Expédition glaciologique internationale au Groenland (EGIG), tirage à part des Meddelelser om Grønland, Bd. 173, Nr. 5, 1968.

Carr, J., Stokes, C., and Vieli, A.: Climatic, oceanic and topographic controls on marine-terminating outlet glacier behaviour in north-west Greenland at seasonal to interannual timescales, J. of Geophys. Res.: Earth Surface, 118, 1–7, doi: 10.1002/jgrf.20088, 2013a.

Carr, J., Stokes, C., and Vieli, A.: Recent progress in understanding marine-terminating Arctic outlet glacier response to climatic and oceanic forcing: Twenty years of rapid change, Progress in Physical Geography, 37, 436–467, doi: 10.1177/0309133313483163, 2013b.

Carr, J., Vieli, A., Stokes, C., Jamieson, S., Palmer, S., Christoffersen, P., Dowdeswell, J., Nick, F., Blankenship, D., and Young, D.: Basal topographic controls on rapid retreat of Humboldt Glacier, nothern Greenland, Journal of Glaciology, 61, 137–150, doi: 10.3189/2015JoG14J128, 2015.

Carroll, D., Sutherland, D. A., Hudson, B., Moon, T., Catania, G. A., Shroyer, E. L., Nash, J. D., Bartholomaus, T. C., Felikson, D., Stearns, L. A., Noël, B. P. Y., and van den Broeke, M. R.: The impact of glacier geometry on meltwater plume structure and submarine melt in Greeland fjords, Geophysical Research Letters, 43, doi: 10.1002/2016GL070170, 2016.

Cassotto, R., Fahnestock, M., Amundson, J. M., Truffer, M., and Joughin, I.: Seasonal and interannual variations in ice melange and its impact on terminus stability, Jakobshavn Isbræ, Greenland, Journal of Glaciology, 61, 76–88, doi: 10.3189/2015JoG13J235, 2015.

Choi, Y., Morlighem, M., Wood, M., and Bondzio, J. H.: Comparison of four calving laws to model Greenland outlet glaciers, The Cryosphere, 12, 3735–3746, doi: 10.5194/tc-12-3735-2018, 2018.

Colgan, W., Rajaram, H., Abdalati, W., McCutchan, C., Mottram, R., Moussavi, M. S., and Grigsby, S.: Glacier crevasses: Observations, models, and mass balance implications, Reviews of Geophysics, 54, 119–161, doi: 10.1002/2015RG000504, 2016.

Cook, S., Rutt, I., Murray, T., Luckman, A., Goldsack, A., and Zwinger, T.: Modelling environmental influences on calving at Helheim Glacier, East Greenland, The Cryosphere, 7, 4407–4442, doi: 10.5194/tc-8-827-2014, 2014.

Cowton, T., Sole, A., Nienow, P., Slater, D., Wilton, D., and Hanna, E.: Controls on the transport of oceanic heat to Kangerdlugssuaq Glacier, East Greenland, Journal of Glaciology, 62, 1167–118, doi: 10.1017/jog.2016.117, 2016.

Cuffey, K. and Paterson, W.: The Physics of Glaciers, Elsevier, Burlington, MA, USA, iSBN 978-0-12-369461-4, 2010.

Duddu, R. and Waisman, H.: A temperature dependent creep damage model for polycrystalline ice, Mechanics of Materials, 46, 23–41, doi: 10.1016/j.mechmat.2011.11.007, 2012.

Duddu, R. and Waisman, H.: A non local continuum damage mechanics approach to simulation of creep fracture in ice sheets, Comput Mech, 51, 961–974, doi: 10.1007/s00466-012-0778-7, 2013.

Duddu, R., Bassis, J. N., and Waisman, H.: A numerical investigation of surface crevasse propagation in glaciers using nonlocal continuum damage mechanics, Geophysical Research Letters, 40, 3064–3068, doi: 10.1002/grl.50602, 2013.

Durand, G., Gagliardini, O., de Fleurian, B., Zwinger, T., and Meur, E. L.: Marine ice sheet dynamics: Hysteresis and neutral equilibrium, Journal of Geophysical Research, 114, doi: 10.1029/2008JF001170, 2009.

Faillettaz, J., Sornette, D., and Funk, M.: Numerical modeling of a gravity-driven instability of a cold hanging glacier: reanalysis of the 1895 break-off of Altelsgletscher, Switzerland, Journal of Glaciology, 57, 817–831, 2011.

Faillettaz, J., Funk, M., and Vincent, C.: Avalanching glacier instabilities: Review on processes and early warning perspectives, Reviews of Geophysics, 53, 203–224, 2015.

Fried, M., Catania, G., Bartholomaus, T., Duncan, D., Davis, M., Stearns, L., Nash, J., Shroyer, E., and Sutherland, D.: Distributed subglacial discharge drives significant submarine melt at a Greenland tidewater glacier, Geophysical Research Letters, 42, doi: 10.1002/2015GL065806, 2015.

Fried, M., Catania, G., Stearns, L., Sutherland, D. A., Bartholomaus, T., Shroyer, E., and Nash, J.: Reconciling drivers of seasonal terminus advance and retreat at 13 central west Greenland tidewater glaciers, Geophysical Research Letters, 123, 1590–1617, doi: 10.1029/2018JF004628, 2018.

Gagliardini, O., Durand, G., Zwinger, T., Hindmarsh, R. C. A., and Meur, E. L.: Coupling of ice-shelf melting and buttressing is a key process in ice-sheet dynamics, Geophysical Research Letters, 37, doi: 10.1029/2010GL043334, 2010.

Greve, R. and Blatter, H.: Dynamics of Ice Sheets and Glaciers, Springer-Verlag Heidelberg, iSBN 978-3-642-03414-5, 2009.

Gudmundsson, G. H. and Raymond, M. J.: On the limit to resolution and information on basal properties obtainable from surface data on ice streams, The Cryosphere Discuss., 2,

413–445, 2008.

Hanson, B. and Hooke, R. L.: Glacier calving: a numerical model of forces in the calving-speed/water-depth relation, Journal of Glaciology, 46, 188–196, doi: 10.3189/172756500781832792, 2000.

Hayhurst, D. R.: Creep rupture under multi-axial states of stress, Journal of the Mechanics and Physics of Solids, 20, 381–390, doi: 10.1016/0022-5096(72)90015-4, 1972.

Holland, D. M., Thomas, R. H., de Young, B., Ribergaard, M. H., and Lyberth, B.: Acceleration of Jakobshavn Isbræ triggered by warm subsurface ocean waters, Nature Geoscience, 1, 659 – 664, doi: 10.1038/ngeo316, 2008.

How, P., Schild, K. M., Benn, D. I., Noormets, R., Kirchner, N., Luckman, A., Vallot, D., Hulton, N. R. J., and Borstad, C.: Calving controlled by melt-under-cutting: detailed calving styles revealed through time-lapse observations, Annals of Glaciology, doi: 10.1017/aog.2018.28, 2019.

Howat, I. M., Box, J. E., Ahn, Y., Herrington, A., and McFadden, E. M.: Seasonal variability in the dynamics of marine terminating outlet glaciers in Greenland, Journal of Glaciology, 56, 601–613, doi: 10.3189/002214310793146232, 2010.

Hunter, L. E. and Powell, R. D.: Ice foot developement at temperate tidewater margins in Alaska, Journal of Geophysical Research, 25, 1923–1926, doi: 10.1029/98GL01403, 1998.

IPCC: Climate Change 2013: The Physical Science Basis. Contribution of Working Group I to the Fifth Assessment Report of the Intergovernmental Panel on Climate Change, Tech. rep., WMO/UNEP, authors: T.F. Stocker, D. Qin, G.-K. Plattner, M. Tignor, S.K. Allen, J. Boschung, A. Nauels, Y. Xia, V. Bex and P.M. Midgley, 2013.

Jenkins, A.: Convection-driven melting near grounding lines of ice shelves and tidewater glaciers, Journal of Physical Oceanography, 41, 2279–2293, doi: 10.1175/JPO-D-11-03.1, 2011.

Jiménez, S. and Duddu, R.: On the evaluation of the stress intensity factor in calving models using linear elastic fracture mechanics, Journal of Glaciology, 64, 759–770, doi: 10.1017/jog.2018.64, 2018.

Jiménez, S., Duddu, R., and Bassis, J.: An updated-Lagrangian damage mechanics formulation for modeling the creeping flow and fracture of ice sheets, Computer methods in applied mechanics and engineering, 313, 406–432, doi: 10.1016/j.cma.2016.09.034, 2017.

Joughin, I., Das, S. B., King, M. A., Smith, B. E., Howat, I. M., and Moon, T.: Seasonal Speedup Along the Western Flank of the Greenland Ice Sheet, Science, 320, 781–783, doi: 10.1126/science.1153288, 2008.

Jouvet, G., Picasso, M., Rappaz, J., Huss, M., and Funk, M.: Modelling and numerical simulation of the dynamics of glaciers including local damage effects, Math. Model. Nat. Phenom., 6, 263–280, doi: 10.1051/mmnp/20116510, 2011.

Kirk, B., Peterson, J. W., Stogner, R. H., and Carey, G. F.: `libMesh`: A C++ Library for Parallel Adaptive Mesh Refinement/Coarsening Simulations, Engineering with Computers, 22,

237–254, doi: 10.1007/s00366-006-0049-3, 2006.

Krug, J., Weiss, J., Gagliardini, O., and Durand, G.: Combining damage and fracture mechanics to model calving, The Cryosphere, 8, 2101–2117, doi: 10.5194/tc-8-2101-2014, 2014.

Krug, J., Durand, G., Gagliardini, O., and Weiss, J.: Modelling the impact of submarine frontal melting and ice mélange on glacier dynamics, The Cryosphere, 9, 989–1003, doi: 10.5194/tc-9-989-2015, 2015.

Lea, J. M., Mair, D. W. F., Nick, F. M., Rea, B. R., van As, D., Morlighem, M., Nienow, P. W., and Weidick, A.: Fluctuations of a Greenlandic tidewater glacier driven by changes in atmospheric forcing: observations and modelling of Kangiata Nunaata Sermia, 1859-present, The Cryosphere, 8, 2031–2045, doi: 10.5194/tc-8-2031-2014, 2014.

Lemaitre, J.: A course on damage mechanics, Springer, Berlin, Germany, second edn., 228 p., 1992.

Leysinger–Vieli, G. J.-M. C. and Gudmundsson, G. H.: On estimating length fluctuations of glaciers caused by changes in climatic forcing, Journal of Geophysical Research, 109, doi: 10.1029/2003JF000027, 2004.

Lliboutry, L.: Velocities, strain rates, stresses, crevassing and faulting on Glacier de Saint-Sorlin, French Alps, 1957-1976, Journal of Glaciology, 48, 125–141, 2002.

Luckman, A., Benn, D. I., Cottier, F., Bevan, S., Nilsen, F., and Inall, M.: Calving rates at tidewater glaciers vary strongly with ocean temperature, Nat. Commun., 6:8566, doi: 10.1038/ncomms9566, 2015.

Lüthi, M. P. and Vieli, A.: Multi-method observation and analysis of a tsunami caused by glacier calving, The Cyrosphere, 10, 995–1002, doi: 10.5194/tc-10-995-2016, 2016.

Lüthi, M. P., Fahnestock, M., and Truffer, M.: Calving icebergs indicate a thick layer of temperate ice at the base of Jakobshavn Isbræ, Greenland, Journal of Glaciology, 55, 563–566, doi: 10.3189/002214309788816650, 2009.

Lüthi, M. P., Vieli, A., Moreau, L., Joughin, I., Reisser, M., Small, D., and Stober, M.: A century of geometry and velocity evolution at Eqip Sermia, West Greenland, Journal of Glaciology, pp. 1–15, doi: 10.1017/jog.2016.38, 2016.

Ma, Y. and Bassis, J. N.: The effect of submarine melting on calving from marine terminating glaciers, J. Geophys. Res. Earth Surf., doi: 10.1029/2018JF004820, 2019.

Ma, Y., Tripathy, C. S., and Bassis, J. N.: Bounds on the calving cliff height of marine terminating glaciers, Geophysical Research Letters, 44, 1369–1375, doi: 10.1002/2016GL071560, 2017.

MacAyeal, D. R.: Large-scale ice flow over a viscous basal sediment: Theory and Application to Ice Stream B, Antarctica, Journal of Geophysical Research, 94, 4071–4078, 1989.

Mahrenholtz, O. and Wu, Z.: Determination of Creep Damage Parameters for Polycrystalline Ice, Advances in Ice Technology (3rd Int. Conf. Ice Tech./Cambridge USA), pp. 181–192, 1992.

Meier, M. F. and Post, A.: Fast Tidewater Glaciers, Journal of Geophysical Research, 92, 9051–9058, 1987.

Mercenier, R., Lüthi, M. P., and Vieli, A.: Calving relation for tidewater glaciers based on detailed stress field analysis, The Cryosphere, 12, 721–739, doi: 10.5194/tc-12-721-2018, 2018.

Mercenier, R., Lüthi, M. P., and Vieli, A.: A transient coupled ice flow-damage model to simulate iceberg calving from tidewater outlet glaciers, Journal of Advances in Modeling Earth Systems, in press, 2019a.

Mercenier, R., Lüthi, M. P., and Vieli, A.: How oceanic melt controls tidewater glacier evolution, Geoph. Res. Lett., in review, 2019b.

Mobasher, M., Duddu, R., Bassis, J. N., and Waisman, H.: Modeling hydraulic fracture of glaciers using continuum damage mechanics, Journal of Glaciology, 62, 794–804, doi: 10.1017/jog.2016.68, 2016.

Morlighem, M., Bondzio, J., Seroussi, H., Rignot, E., Larour, E., Humbert, A., and Rebuffi, S.: Modeling of Store Gletscher's calving dynam- ics, West Greenland, in response to ocean thermal forcing, Geophysical Research Letters, 43, 2659–2666, doi: 10.1002/2016GL067695, 2016.

Morlighem, M., Williams, C. N., Rignot, E., An, L., Arndt, J. E., Bamber, J. L., Catania, G., Chauché, N., Dowdeswell, J. A., Dorschel, B., Fenty, I., Hogan, K., Howat, I., Hubbard, A., Jakobsson, M., Jordan, T. M., Kjeldsen, K. K., Millan, R., Mayer, L., Mouginot, J., Noël, B. P. Y., O'Cofaigh, C., Palmer, S., Rysgaard, S., Seroussi, H., Siegert, M. J., Slabon, P., Straneo, F., van den Broeke, M. R., Weinrebe, W., Wood, M., and Zinglersen, K. B.: BedMachine v3: Complete Bed Topography and Ocean Bathymetry Mapping of Greenland From Multibeam Echo Sounding Combined With Mass Conservation, Geophysical Research Letters, 44, 11 051–11 061, doi: 10.1002/2017GL074954, 2017.

Morlighem, M., Wood, M., Seroussi, H., Choi, Y., and Rignot, E.: Modeling the response of northwest Greenland to enhanced ocean thermal forcing and subglacial discharge, The Cryosphere, 13, 723–734, doi: 10.5194/tc-13-723-2019, 2019.

Motyka, R. J.: Deep-water calving at Le Conte, Southeast Alaska, in: Calving Glaciers: Report of a Workshop, edited by Van der Veen, C. J., BPRC Report No. 15, pp. 115–118, Byrd Polar Research Center, Ohio State University, Columbus, Ohio, 1997.

Motyka, R. J., Dryer, W. P., Amundson, J., Truffer, M., and Fahnestock, M.: Rapid submarine melting driven by subglacial discharge, LeConte Glacier, Alaska, Geophysical Research Letters, 40, 1–6, doi: 10.1002/grl.51011, 2013.

Murray, T., Selmes, N., James, T., Edwards, S., Martin, I., O'Farwell, T., Aspey, R., Rutt, I., Nettles, M., and Baugé, T.: Dynamics of glacier calving at the ungrounded margin of Helheim Glacier, southeast Greenland, Journal of Geophysical Research, 120, 964–982, doi: 10.1002/2015JF003531, 2015.

Nick, F., Van der Veen, C., Vieli, A., and Benn, D. I.: A physically based calving model applied to marine outlet glaciers and implications for the glacier dynamics, Journal of

Glaciology, 56, 781–794, doi: 10.3189/002214310794457344, 2010.

Nick, F., Vieli, A., Andersen, M. L., Joughin, I., Payne, A., Edwards, T. L., Pattyn, F., and van de Wal, R. S.: Future sea-level rise from Greenland's main outlet glaciers in a warming climate, Nature, 479, 235–238, doi: 10.1038/nature12068, 2013.

Nick, F. M., Vieli, A., Howat, I. M., and Joughin, I.: Large-scale changes in Greenland outlet glacier dynamics triggered at the terminus, Nature Geoscience, 2, 110–114, doi: 10.1038/ngeo394, 2009.

Nye, J. F.: The distribution of stress and velocity in glaciers and ice-sheets, Proceedings of the Royal Society of London, Ser. A, 239, 113–133, 1957.

O'Leary, M. and Christoffersen, P.: Calving of tidewater glaciers amplified by submarine frontal melting, The Cryosphere, 7, 119–128, doi: 10.5194/tc-7-119-2013, 2013.

O'Neel, S., Marshall, H., McNamara, D., and Pfeffer, W.: Seismic detection and analysis of earthquakes at Columbia Glacier, Alaska, Journal of Geophysical Research, 112, doi: 10.1029/2006JF000595, 2007.

Otero, J., Navarro, F., Martin, C., Cuadrado, M., and Corcuera, M.: A three-dimentional calving model: numerical experiments on Johnsons Glacier, Livingston Island, Antarctica, Journal of Glaciology, 56, 200–214, doi: 10.3189/002214310791968539, 2010.

Otero, J., Navarro, F., Lapazaran, J. J., Welty, E., Puczko, D., and Finkelnbrug, R.: Modeling the controls on the front position of a tidewater glacier in Svalbard, Frontiers in Earth Science, 5, 200–214, doi: 10.3389/feart.2017.00029, 2017.

Petlicki, M., Cieply, M., Jania, J. A., Prominska, A., and Kinnard, C.: Calving of a tidewater glacier driven by melting at the waterline, Journal of Glaciology, 61, 851–863, doi: 10.3189/2015JoG15J062, 2015.

Pfeffer, T.: A simple mechanism for irreversible tidewater glacier retreat, Journal of Geophysical Research, 112, doi: 10.1029/2006JF000590, 2007.

Post, A., , O'Neel, S., Motyka, R., and Streveler, G.: A Complex Relationship Between Calving Glaciers and Climate, EOS, 92, 305–306, doi: 10.1029/2011EO370001, 2011.

Pralong, A.: Ductile Crevassing, in: Glacier Science and Environmental Change, edited by Knight, P. G., Blackwell Publishing, Oxford, p. 62, 2006.

Pralong, A. and Funk, M.: Dynamic Damage Model of Crevasse Opening and Application to Glacier Calving, Journal of Geophysical Research, 110, doi: 10.1029/2004JB003104, 2005.

Pralong, A., Funk, M., and Lüthi, M. P.: A description of crevasse formation using continuum damage mechanics, Annals of Glaciology, 37, 77–82, doi: 10.3189/172756403781816077, 2003.

Rignot, E., Box, J. E., Burgess, E., and Hanna, E.: Mass balance of the Greenland ice sheet from 1958 to 2007, Geophysical Research Letters, 35, doi: 10.1029/2008GL035417, 2008.

Rignot, E., Koppes, M., and Velicogna, I.: Rapid submarine melting of the calving faces of West Greenland glaciers, Nature Geoscience, 3, 187–191, doi: 10.1038/NGEO765, 2010.

Rignot, E., Fenty, I., Xu, Y., Cai, C., and Kemp, C.: Undercutting of marine-terminating glaciers in West Greenland, Geophysical Research Letters, 42, 5909–5917, doi: 10.1002/2015GL064236, 2015.

Rist, M. A., Sammonds, P. R., Murrell, S. A. F., Meredith, P. G., Doake, C. S. M., Oerter, H., and Matsuki, K.: Experimental and theoretical fracture mechanics applied to Antarctic ice fracture and surface crevassing, Journal of Geophysical Research - Solid Earth, 104, 2973–2987, 1999.

Ryan, J., Hubbard, A., Box, J., Todd, J., Christoffersen, P., Carr, J., Holt, T., and Snooke, N.: UAV photogrammetry and structure from motion to assess calving dynamics at Store Glacier, a large outlet draining the Greenland ice sheet, The Cryosphere, 9, 1–11, 2015.

Ryser, C., Lüthi, M., Andrews, L., Catania, G., Funk, M., Hawley, R., Hoffman, M., and Neumann, T.: Caterpillar-like ice motion in the ablation zone of the Greenland Ice Sheet, J. Geophys. Res. Earth Surf., 119, 2258–2271, doi: 10.1002/2013JF003067, 2014a.

Ryser, C., Lüthi, M., Andrews, L., Hoffman, M., Catania, G., Hawley, R., Neumann, T., and Kristensen, S. S.: Sustained high basal motion of the Greenland Ice Sheet revealed by borehole deformation, Journal of Glaciology, 60, 647–660, doi: 10.3189/2014JoG13J196, 2014b.

Sciascia, R., Straneo, F., Cenedese, C., and Heimbach, P.: Seasonal variability of submarine melt rate and circulation in an East Greenland fjord, Journal of Geophysical Research, 118, 2492–2502, 2013.

Shepherd, A., Ivins, E. R., A, G., Barletta, V. R., Bentley, M. J., Bettadpur, S., Briggs, K. H., Bromwich, D. H., Forsberg, R., Galin, N., Horwath, M., Jacobs, S., Joughin, I., King, M. A., Lenaerts, J. T. M., Li, J., Ligtenberg, S. R. M., Luckman, A., Luthcke, S. B., McMillan, M., Meister, R., Milne, G., Mouginot, J., Muir, A., Nicolas, J. P., Paden, J., Payne, A. J., Pritchard, H., Rignot, E., Rott, H., Sørensen, L. S., Scambos, T. A., Scheuchl, B., Schrama, E. J. O., Smith, B., Sundal, A. V., van Angelen, J. H., van de Berg, W. J., van den Broeke, M. R., Vaughan, D. G., Velicogna, I., Wahr, J., Whitehouse, P. L., Wingham, D. J., Yi, D., Young, D., and Zwally, H. J.: A Reconciled Estimate of Ice-Sheet Mass Balance, Science, 338, 1183–1189, doi: 10.1126/science.1228102, 2012.

Slater, D. A., Nienow, P. W., Cowton, T. R., Goldberg, D. N., and Sole, A. J.: Effect of near-terminus subglacial hydrology on tidewater glacier submarine melt rates, Geophysical Research Letters, 42, 2861–2868, doi: 10.1002/2014GL062494, 2015.

Slater, D. A., Goldberg, D. N., Nienow, P. W., and Cowton, T. R.: Scalings for Submarine Melting at Tidewater Glaciers from Buoyant Plume Theory, Journal of Physical Oceanography, 46, 1836–1855, doi: 10.10175/JPO-D-15-0132.1, 2016.

Slater, D. A., Straneo, F., Das, S. B., Richards, C. G., Wagner, T. J. W., and Nienow, P. W.: Localized Plumes Drive Front-Wide Ocean Melting of A Greenlandic Tidewater Glacier, Geophysical Research Letters, 45, 12 350–12 358, doi: 10.1029/2018GL080763, 2018.

Smith, R.: The application of fracture mechanics to the problem of crevasse penetration, Journal of Glaciology, 17, 223–228, doi: /10.3189/S0022143000013563, 1976.

Stearns, L. A. and van der Veen, C. J.: Friction at the bed does not control fast glacier flow, Science, 361, 273–277, doi: 10.1126/science.aat2217, 2018.

Straneo, F. and Heimbach, P.: North Atlantic warming and the retreat of Greenland's outlet glaciers, Nature, 504, 36–43, doi: 10.1038/nature12854, 2013.

Straneo, F., Curry, R. G., Sutherland, D. A., Hamilton, G. S., Cenedese, C., Vage, K., and Stearns, L. A.: Impact of fjord dynamics and glacial runoff on the circulation near Helheim Glacier, Nature Geoscience, 4, 322–327, 2011.

Straneo, F., Heimbach, P., Sergienko, O., Hamilton, G., Catania, G., Griffies, S., Hallberg, R., Jenkins, A., Joughin, I., Motyka, R., Pfeffer, W. T., Price, S. F., Rignot, E., Scambos, T., Truffer, M., and Vieli, A.: Challenges to Understand the Dynamic Response of Greenland's Marine Terminating Glaciers to Oceanic and Atmospheric Forcing, Bulletin of the American Meteorological Society, 94, 1131–1144, doi: 10.1175/BAMS-D-12-00100.1, 2013.

Sugiyama, S., Sakakibara, D., Tsutaki, S., Maruyama, M., and Sawagaki, T.: Glacier dynamics near the calving front of Bowdoin Glacier, northwestern Greenland, Journal of Glaciology, 61, 223–23, doi: 10.3189/2015JoG14J127, 2015.

Sugiyama, S., Minowa, M., and Schaefer, M.: Underwater Ice Terrace Observed at the Front of Glaciar Grey, a Freshwater Calving Glacier in Patagonia, Geophysical Research Letters, 46, doi: 10.1029/2018GL081441, 2019.

Todd, J. and Christoffersen, P.: Are seasonal calving dynamics forced by buttressing from ice mélange or undercutting by melting? Outcomes from full-Stokes simulations of Store Glacier, West Greenland, The Cryosphere, 8, 2353–2365, doi: 10.5194/tc-8-2353-2014, 2014.

Todd, J., Christoffersen, P., Zwinger, T., Raback, P., Chauché, N., Benn, D., Luckman, A., Ryan, J., Toberg, N., Slater, D., and Hubbard, A.: A Full-Stokes 3-D Calving Model Applied to a Large Greenlandic Glacier, Journal of Geophysical Research: Earth Surface, 123, 410–432, doi: 10.1002/2017JF004349, 2018.

Trüssel, B., Truffer, M., Hock, R., Motyka, R., Huss, M., and Zhang, J.: Runaway thinning of the low-elevation Yakutat Glacier, Alaska, and its sensitivity to climate change, Journal of Glaciology, 61, 65–75, doi: 10.3189/2015JoG14J125, 2015.

van den Broeke, M., Bamber, J., Ettema, J., Rignot, E., Schrama, E., van de Berg, W. J., van Meijgaard, E., Velicogna, I., and Wouters, B.: Partitioning recent Greenland mass loss, Science, 326, 984–986, doi: 10.1126/science.1178176, 2009.

van den Broeke, M., Enderlin, E. M., Howat, I., Kuipers Munneke, P., Noël, B. Y. P., van de Berg, W. J., van Meijgaard, E., and Wouters, B.: On the recent contribution of the Greenland ice sheet to sea level change, The Cryosphere, 10, 1933–1946, doi: 10.5194/tc-10-1933-2016, 2016.

Van der Veen, C.: Calving glaciers, Progress in Physical Geography, 26, 96–122, 2002.

Van der Veen, C. J.: Tidewater calving, Journal of Glaciology, 42, 375–385, 1996.

Van der Veen, C. J.: Fracture mechanics approach to penetration of surface crevasses on glaciers, Cold Regions Science and Technology, 27, 31–47, 1998a.

Van der Veen, C. J.: Fracture mechanics approach to penetration of bottom crevasses on glaciers, Cold Regions Science and Technology, 27, 213–223, 1998b.

Van der Veen, C. J.: Fundamentals of Glacier Dynamics, A. A. Balkema, Rotterdam/Brookfield, 1999.

Vaughan, D. G.: Relating the occurrence of crevasses to surface strain rates, Journal of Glaciology, 39, 255–266, doi: 10.3189/S0022143000015926, 1993.

Vaughan, D. G. and Arthern, R.: Why is it hard to predict the future of ice sheets, Science, 315, 1503–1504, doi: 10.1126/science.1141111, 2007.

Vieli, A. and Nick, F.: Understanding and modelling rapid dynamic changes of tidewater outlet glaciers: issues and implications, Surveys in Geophysics, 32, 437–458, doi: 10.1007/s10712-011-9132-4, 2011.

Vieli, A., Funk, M., and Blatter, H.: Flow dynamics of tidewater glaciers: a numerical modelling approach, Journal of Glaciology, 47, 595–606, 2001.

Vieli, A., Boxleitner, M., and Lüthi, M. P.: Understanding variations in early Holocene retreat pattern along the fjord- and land-terminating ice sheet margin in West-Greenland, Geophysical Research Abstracts, 21, EGU2019-16709, 2019.

Voytenko, D., Dixon, T. H., Howat, I. M., Gourmelen, N., Lembke, C., Werner, C. L., de la Peñ, S., and Oddsson, B.: Multi-year observations of Breidamerkurjökull, a marine-terminating glacier in southeastern Iceland, using terrestrial radar interferometry, Journal of Glaciology, 61, 42–54, doi: 10.3189/2015JoG14J099, 2015.

Waddington, E.: Life, death and afterlife of the extrusion flow theory, Journal of Glaciology, 200, 973–996, 2010.

Walter, F., Amundson, J., O'Neel, S., Truffer, M., Fahnestock, M., and Fricker, H.: Analysis of low-frequency seismic signals generated during a multiple-iceberg calving event at Jakobshavn Isbræ, Greenland, Journal of Geophysical Research, 117, doi: 10.1029/2011JF002132, 2012.

Warren, C. R., Glasser, N. F., Harrison, S., Winchester, V., Kerr, A. R., and Rivera, A.: Characteristics of tide–water calving Glaciar San Rafael, Journal of Glaciology, 41, 273–288, doi: 10.3189/S0022143000016178, 1995.

Warren, C. R., Benn, D., Winchester, V., and Harrison, S.: Buoyancy-driven lacustrine calving, Glaciar Nef, Chilean Patagonia, Journal of Glaciology, 47, 135–146, doi: 10.3189/172756501781832403, 2001.

Weertman, J.: Can a water-filled crevasse reach the bottom surface of a glacier?, IASH Publ., 95, 1973.